Akademia Górniczo-Hutnicza im. Stanisława Staszica

Wydział Inżynierii Metali i Informatyki Przemysłowej

Rozprawa doktorska

Mechanical Properties and Microstructure of Dense Ceramic Membranes for Oxygen Separation in Zero-Emission Power Plants

Bogdan Rutkowski

Promotor:

Univ.-Prof. Dr.-Ing. Tilmann Beck
Prof. dr hab. inż. Aleksandra Czyrska-Filemonowicz

Aachen / Kraków 2012

Kurzfassung

In der vorliegenden Arbeit wurden mechanische Eigenschaften sowie Mikrostruktur von Perowskitstrukturierten dichten keramischen $Ba_{0.5}Sr_{0.5}Co_{0.8}Fe_{0.2}O_{3-d}$ (BSCF) Membranen für die Anwendung als Sauerstofftrennmembran untersucht. Die Herstellung des Materials erfolgt beim Fraunhofer Institut für Keramische Technologien und Systeme (IKTS), Hermsdorf, Deutschland.

Einachsige Hochtemperaturbelastungstests, erlaubten eine genaue Ermittlung von Materialkriechfestigkeit bei unterschiedlichen Belastungen und Sauerstoffpartialdrücken im Anwendungsrelevanten Temperaturbereich für die röhrenförmigen Proben. Darüber hinaus ermöglichten die Tests eine Bewertung des Einflusses der Korngröße auf das Kriechverhalten. Das Kriechverhalten des BSCF Materials wurde mathematisch durch eine Standardkriechgleichung in Abhängigkeit von Temperatur, Spannung, Sauerstoffdruck, und Korngröße, erfasst. Die Ergebnisse der im Vakuum durchgeführten Kriechversuchen bestätigten die Existenz von zwei Kriechregimen, die durch verschiedene Aktivierungsenergie gekennzeichnet sind. Die Übergang der Kriechmechanismen tritt bei etwa 800 °C auf. Das Kriechverhalten in Luft ist jedoch noch viel komplizierter: für die Kriechuntersuchen, die während Aufheizsequenz durchgeführt wurden, zeigten sich wieder wie unter reduzierten Sauerstoffpartialdrücken zwei Kriechregime mit unterschiedlichen Aktivierungsenergien. Jedoch ist die Übergangstemperatur zu 850 °C verschoben. Dieser Unterschied kann mit einer Materialinstabilität und der Bildung einer hexagonal Phase in Verbindung gebracht werden. Darüber hinaus wurde eine Hysterese - Kriechraten um die 850 ° C beobachtet die während der Abkühlung zu deutlich höheren Kriechrate führte. Um die Kriechergebnisse für Luft zu überprüfen, wurden zusätzlich BSCF Proben in zylindrischer Geometrie getestet. Zusätzliche wurden Kriechversuche an einem neu entwickelten $BaCo_{0.4}Fe_{0.4}Zr_{0.2}O_{3-\delta}$ (BCFZ) Material durchgeführt.

Ergänzend zu Kriecharakterisierung erfolgten auch Biegeversuch an O-Ring Proben die eine Bestimmung der Temperaturabhängigkeit von Elastizitätsmodul und Festigkeit erlaubten. Nachfolgende fraktographische Analysen bestätigten längliche Poren und

Agglomerate als Bruchursprung. Zusätzlich ergaben die mikromechanischen Messungen Mikrohärte und Elastizitätsmodul bei Raumtemperatur.

Um die Informationen über Materialstabilität zu gewinnen wurden Langzeitauslagerungen (2 Wochen) in Luft im anwendungsrelevanten Temperaturbereich (750-950 °C) durchgeführt. Diese Studien wurden durch eine qualitative mikrostrukturelle Untersuchung mittels Lichtmikroskopie ergänzt und weist auf signifikante Materialsinstabilitäten hin. Ausscheidungen von hexagonaler Phase wurden nach Auslagerung in Luft, bei 850 °C gefunden und der Volumenanteil dieser Phase scheint temperaturabhängig zu sein (mit einem Maximum bei 750 °C).

Die Analyse der Mikrostruktur von der Rohren, die in einem Demonstrator unter Anwendungen kraftwerkstypischer Bedingungen betrieben wurden, ermöglichte eine Untersuchung der mikrostrukturellen Veränderungen des Materials und eine Ermittlung des axialen Temperaturprofil der Rohre im Demonstratortest.

Schließlich wurden alle Ergebnisse zusammengefasst und Schlussfolgerungen gezogen.

Abstract

In the present work, the mechanical properties as well as microstructure of perovskite-structured $Ba_{0.5}Sr_{0.5}Co_{0.8}Fe_{0.2}O_{3-d}$ (BSCF) dense ceramic membranes for oxygen separation were investigated. The main supplier of the material was the Fraunhofer-Institut für Keramische Technologien und Systeme (IKTS), Hermsdorf, Germany. High temperature uniaxial compressive tests on tubular specimens allow the precise determination of material's creep resistance under varied load in the wide range of application relevant temperatures and various oxygen partial pressures. Additionally, it allows to establish the influence of grain size on creep. The results of the creep test were described by the steady state creep equation, which allows to predict the creep resistance of the material under varied conditions (like: stress, oxygen pressure, grain size, temperature). Creep tests performed in vacuum, revealed the existence of two creep regimes, characterised by different activation energy. Change of creep mechanism occurs at around 800 °C. In air, creep behavior is much more complicated: during heating sequence, also two regimes are visible, however transition temperature is shifted to 850 °C. This difference is related to materials instability and hexagonal phase formation. Moreover, hysteresis was found- creep rates obtained at 850 °C during cooling sequence are significantly higher than one obtained during heating. In order to verify creep results obtained for air, additional specimens with cylindrical geometry were tested. Furthermore, additional creep tests were conducted on a newly developed $BaCo_{0.4}Fe_{0.4}Zr_{0.2}O_{3-\delta}$ (BCFZ) material. Complementary to creep characterization, also bending test on O-ring specimens, machined from tubes, were carried out. Temperature dependence of Young's modulus and strength were established. Subsequent fractographic analyses revealed elongated pores and agglomerates as fracture origins. Additionally, micromechanical measurements provided information concerning the micro-hardness and Young's modulus at the room temperature.

In order to gain information about material stability, a long-term (2 weeks) annealing of BSCF in the air in the range of application-relevant temperatures (750 - 950 °C) was performed. The study was complemented by qualitative microstructural investigation performed by means of light microscopy and revealed significant material instability. Precipitates of hexagonal phase are present after annealing in air below 850 °C, and their volume fraction is temperature-dependent (maximum occurs at 750 °C).

Post operation analysis of tubes operated in a demonstration unit under conditions expected in a real power-plant operation allows to investigate microstructural changes in the material and find the axial temperature profile in the membrane tube.
Finally, all collected results were summarized and conclusions were drawn.

Contents

Introduction

The worldwide energy demand is expected to reach 35.2 trillion kilowatt-hours in the next three decades, which is a factor two higher than the demand in 2008 [1]. One of the most widely used energy sources for large scale electricity production are still fossil fuels [1]. However, these are also considered to be one of the largest emission sources of greenhouse gases [1] (CO_2, NO_X, SO_X). Therefore, according to the Kyoto-Protocol issued in 1997, 84 countries are committed to the progressive reduction of greenhouse gas emissions [2], mainly CO_2 that appears to have the greatest share in causing the global warming effect.

One of the methods currently under development for CO_2 emission reduction is carbon dioxide capture. The CO_2 should eventually be stored in liquid form in natural cavities (carbon capture and storage, CCS) [3, 4]. One of the most promising techniques of CCS appears to be CO_2 separation using inorganic membranes [5]. Three main technical implementations can be distinguished: post-combustion, pre-combustion and the OXYFUEL process [6, 7].

In the post-combustion technology, carbon dioxide is separated from flue gases (containing mainly N_2) for example using micro-sieving membranes after the combustion process. One main disadvantage of this process is the rather low CO_2 and high N_2 concentration in flue gas (N_2 to CO_2 ratio is around 9:1).

The pre-combustion process targets the disadvantages of the N_2 presence. Here, oxygen is extracted from air by mixed ionic-electronic conducting (MIEC) dense ceramic membranes at the beginning of the process. Fuel is partially oxidized in pure oxygen, to obtain CO as an intermediate product. Afterwards, partially oxidized fuel goes into reaction with water vapor (CO-shift reaction), resulting in a mixture of H_2 and CO_2. These gases are separated either with proton conducting H_2 - selective dense ceramic membranes or polymeric H_2 or CO_2 selective membranes, and finally hydrogen is used as a fuel for power plant while CO_2 is captured and stored.

For oxygen separation in the OXYFUEL process, similar MIEC membranes as for the pre-combustion process might be used. Here, the aim is the combustion of fossil fuels in pure oxygen and hence, to eliminate nitrogen and its products from the flue gases. Accordingly, only CO_2 and H_2O are combustion products. In this case, CO_2 separation is rather simple – H_2O is removed via vapor condensation.

Compared to the other separation methods, the main advantage of the OXYFUEL process is its rather small efficiency loss (around 5 % points) of the power plant [8], which makes this process economically more interesting than the other alternatives mentioned above. Combustion of fuel in pure oxygen increases both, the flame temperature as well as energy density, which requires combustor re-design. Therefore a recirculation of CO_2, is introduced in order to substitute the temperature stabilizing effect of nitrogen, removed earlier by air separation units (ASU). This modification allows to keep the flame temperature on a level according to the current state of the art, and therefore permitting the use of standard combustors [9, 10].

Due to its high oxygen permeation coefficients [11, 12], the perovskite $Ba_{0.5}Sr_{0.5}Co_{0.8}Fe_{0.2}O_{3-\delta}$ (BSCF 5582) appears to be one of the most promising materials for application as dense ceramic MIEC membrane. Its high specific flux permits to use relatively small membrane areas to obtain the necessary oxygen flux required for the combustion process [13]. Membrane materials applied in particular in the OXYFUEL process are exposed to high temperatures (ultimately 800 °C) as well as to high oxygen pressure differences. Therefore, beside high oxygen fluxes, also adequate resistance with respect to these environmental conditions, in particular mechanical integrity (at elevated temperatures and also during thermal cycling) is required. Hence, assessment of the mechanical properties, especially strength and creep resistance plays an essential role in material development.

The current work mainly focuses on the correlation of microstructure and mechanical properties with special emphasis on the creep behavior of the perovskite-type BSCF membrane material considering the requirements of the OXYFUEL process. Moreover, supporting investigation was carried out to determine other basic mechanical properties, such as: strength, fracture stress, Young's modulus and hardness. In addition to an understanding of the mechanical behavior, the performed assessment of the origins of failure, degradation and microstructural as well as mechanical property changes under operation relevant conditions is a prerequisite for the improvement of materials. Furthermore, in addition to these experiments under simulated atmospheres the investigation was supplemented by analysis of membrane tubes after demonstrator operation.

1. **Literature review**

Mixed ionic-electronic conductors are promising materials for applications such as reactors for syngas production [14-16], electrodes for solid oxide fuel cells [17-22] and oxygen separating membranes [11, 12, 23, 24].

BSCF 5582 appears to be one of the most promising materials especially to fulfill the requirements of the OXYFUEL process. The $Ba_XSr_{1-X}Cr_YFe_{1-Y}O_{3-\delta}$ material has a cubic ABO_3 perovskite structure (see Figure 1). Its high permeation allows an operation at a temperature of about 800 °C to provide satisfactory oxygen flux [13, 25]. Furthermore, contrary to other membrane materials BSCF 5582 has no cubic to rhomboidal phase transformation at intermediate temperatures that could diminish the oxygen flux.

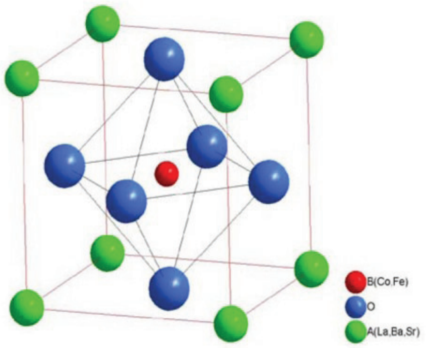

Figure 1. Sketch of the BSCF unit cell [26].

1.1. **Membrane application**

A ceramic oxygen transport membrane is an oxide material with the ability to transport oxygen ions through its lattice, while simultaneously representing a barrier for other elements (e.g. nitrogen, neon, argon). ABO_3 perovskite structured materials which contain a large amount of oxygen atoms in the lattice are mainly considered for this application. The necessary operation temperature for such ceramic membranes is usually higher than 500 °C, where the oxygen vacancy concentration increases by the continuous release of oxygen [16, 27] from the lattice which leads to a sufficient amount of pathways for oxygen transport.

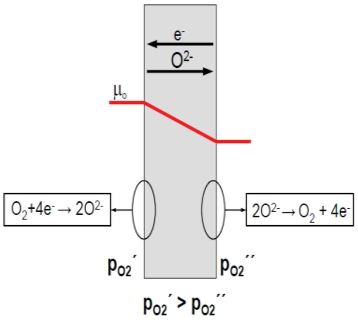

Figure 2. Schematic drawing of the function of an oxygen permeable membrane. Difference in oxygen partial pressures is the driving force for oxygen transport [26].

In the membrane application (Figure 2), the material will be exposed to oxygen partial pressure differences; one side of the membrane might be exposed to air (oxygen partial pressure pO_2') whereas the other surface will be exposed to an oxygen depleted environment (e.g. vacuum, pO_2”). Hence, a driving force (gradient in chemical potentials) for oxygen transport exists. Oxygen will be adsorbed on the membrane surface subjected to higher oxygen partial pressure and diffuse via oxygen vacancies to the other side of membrane.

The oxygen permeation coefficient of the membranes should be as high as possible, to reduce the required membrane area.

Due to specifications of OXYFUEL process chain, oxygen separation units have to be placed directly behind the air intake of the power plant line (Figure 3).

According to Higginbotham et al. [28], around 10.000 tons of O_2 per day have to be separated in a 500 MW power plant. Calculations by Engels et al. [25] for a 4-end membrane model, operating at a temperature about 800 °C, yield an necessary membrane area of around 0.28 m^2/kW_{th}. Hence, for a 500 MW power plant the membrane area will be 140000 m^2.

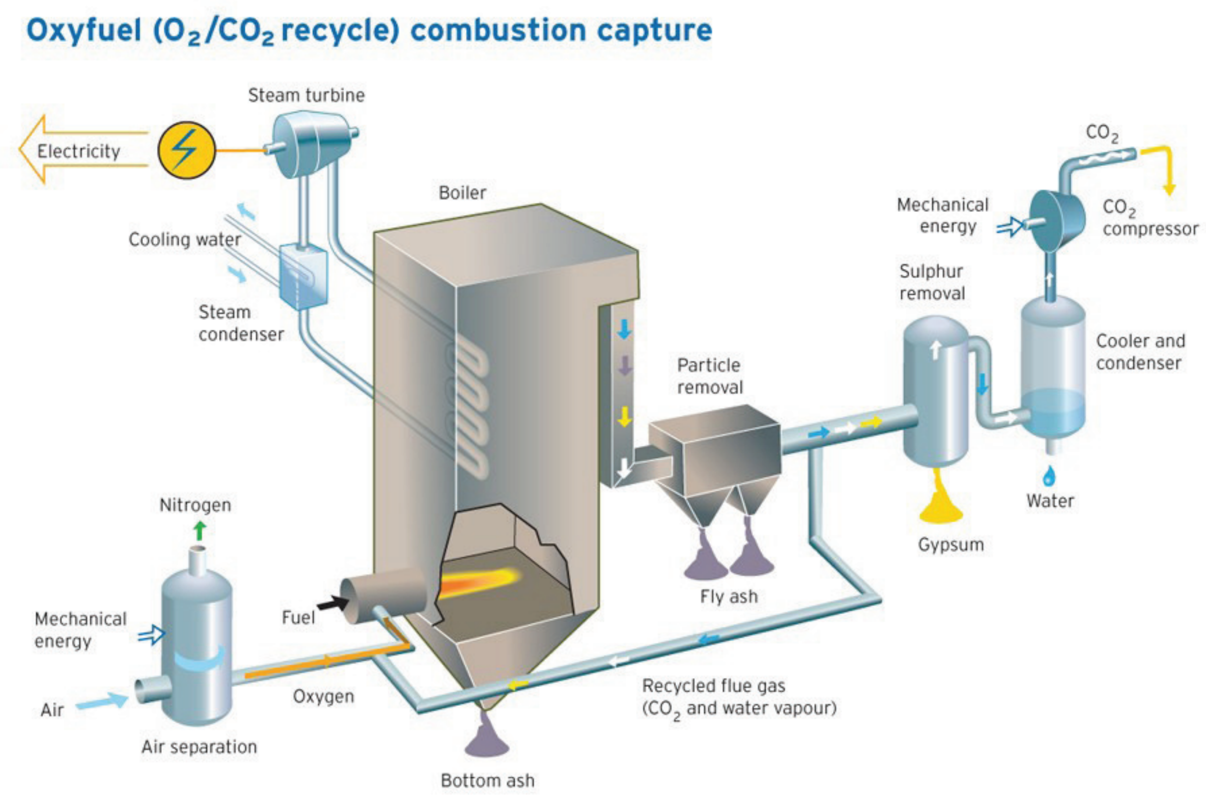

Figure 3. Schematic chart of a fossil fuel fired power plant configured for the OXYFUEL process (Vattenfall) [29].

Combustion of coal in oxygen has a lot of advantages. One of them is the elimination of nitrogen (78 % in air), resulting in CO_2 and H_2O as main products in flue gases which can be simply separated from each other by condensation (Figure 3). Subsequently, CO_2 can be directly compressed and stored in natural cavities. In contrast to this, during combustion of coal in air, the flue gas contains mainly nitrogen and only 10 % of CO_2. In this case separation of those components can be carried out with micro-sieving membranes, which results, however, in higher efficiency losses than in the OXYFUEL process [8].

1.2. BSCF development

BSCF5582 is a perovskite material with the general chemical formula ABO_3 and a cubic lattice structure. As illustrated in Figure 1, the A side is occupied with Ba and Sr atoms in the ratio 1:1 and the B side with Fe and Co in the ratio 4:1. Valence state of B side dopants can vary from 4+ to 2+ in case of cobalt. For iron, only 4+ and 3+ states are possible in the oxygen concentration range 1 to 10^{-6} atm [30].

BSCF material was developed on the basis of the knowledge on the compound $SrCoO_{3-\delta}$. [13, 30, 31], which exhibits a high oxygen permeation coefficient at elevated temperatures ($3.4 \cdot 10^{-7}$ $mol \cdot cm^{-2} \cdot s^{-1}$ at 1000 °C) [31], however, its perovskite structure has reported to be rather unstable [31]. The material can therefore only be used at temperatures above 1000 °C. Below this temperature a perovskite – brownmillerite transformation leads to a strong decrease of the oxygen permeation (Figure 4).

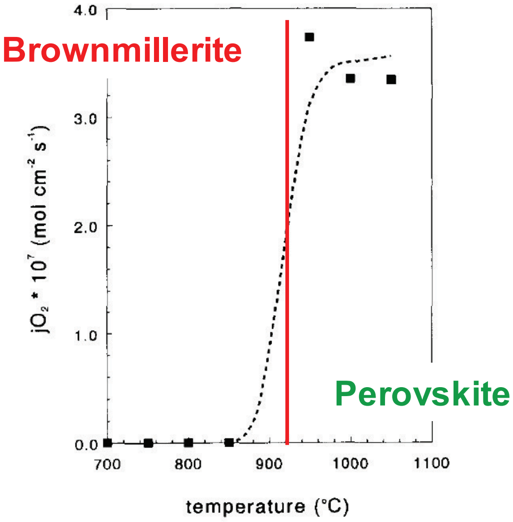

Figure 4. Oxygen permeation of $SrCoO_{3-\delta}$ perovskite type membrane. Below 1000°C the formation of a brownmillerite structure decreases the permeation [31].

Below 850°C, where a low temperature ordered vacancy structure becomes stable, oxygen permeation decreases to almost zero. Furthermore, Kruidhof et al. [31] reported that the crystal lattice of $SrCoO_{3-\delta}$ at RT in the as-received state is strongly dependent on the preparation conditions leading to either a cubic, orthorhombic or tetragonal structure.

Efforts directed toward improving the perovskite stability by a partial substitution of Co with Fe, led to the compound $SrCo_{0.8}Fe_{0.2}O_{3-\delta}$ (SCF). Here an oxygen permeation coefficient of about $2\cdot10^{-7}$ $mol\cdot cm^{-2}\cdot s^{-1}$ was obtained at 900 °C. Basically, the iron addition of 20 % on the B-side extended the perovskite phase stability range by 110 K down to a temperature of 790 °C (Figure 5) [13].

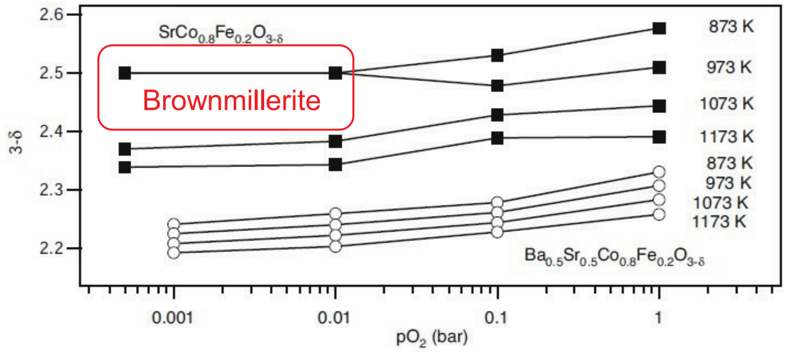

Figure 5. Oxygen stoichiometry of SCF and BSCF as a function of oxygen partial pressure. The oxygen stoichiometry of 2.5 is typical for a Brownmillerite structure [13].

The limit of the temperature window for brownmillerite structure in SCF can also be seen in the results of differential thermal analysis (TGA-DTA) (Figure 6) [13], which indicates that the typical oxygen stoichiometry of 2.5 is limited to a temperature below 780 °C.

These unsatisfactory results led to additional experiments with other A – side dopants. It was found that a 60 % substitution of Sr with La changed the transition temperature to around 860 - 910 °C, but also decreased the permeation rate of the resulting $La_{0.6}Sr_{0.4}Co_{0.8}Fe_{0.2}O_{3-\delta}$ (LSCF) material from $2\cdot10^{-7}$ (reported for SCF) down to $3\cdot10^{-8}$ $mol\cdot cm^{-2}\cdot s^{-1}$ [31] at 925 °C.

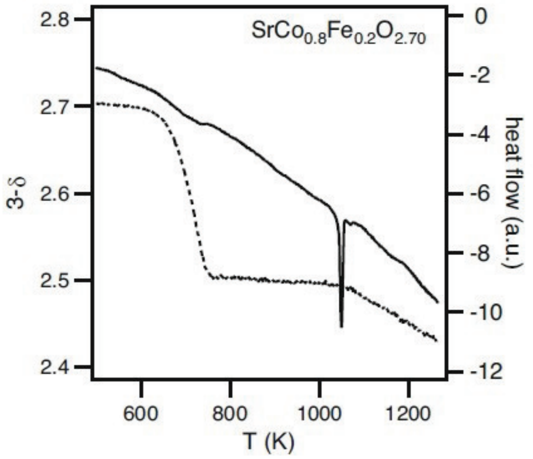

Figure 6. Change of oxygen stoichiometry of SCF as a function of temperature in nitrogen atmosphere. An oxygen stoichiometry of 2.5 corresponds to the stability range of brownmillerite - like structure [13].

According to Vente et al. [13], modification of SCF by a partial substitution of Sr with barium on the A side, ($Ba_XSr_{1-X}Co_YFe_{1-X}O_{3-\delta}$ - BSCF) should not lead to such disadvantages and the resulting material should maintain a stable cubic structure in a wide temperature and oxygen partial pressure range (600 - 900 °C and 1 - 1000 mbar) (Figure 5).

Stability measurements of BSCF 5582 obtained by Vente et al. [13] via neutron diffraction, that were also confirmed by TGA measurements, didn't reveal any signs of BSCF instability in the intermediate temperature range, which was in good agreement with short time-scale (70 min at each temperature) stability measurements performed with XRD method by Wang et al. [32]. Note that a stabilization effect was already visible when the A side was doped with only 10 % of barium [13].

The BSCF, as well as $Ba_{0.5}Sr_{0.5}FeO_{3-\delta}$ (BSF), was found to be stable down to an oxygen partial pressure of 10^{-5} atm up to 1000 °C, whereas $Ba_{0.5}Sr_{0.5}CoO_{3-\delta}$ (BSC) shows a rhombohedral lattice structure at oxygen partial pressures less than 10^{-5} atm below 850 °C [33].

Note that partial substitution of Sr with Ba atoms, that have a larger atomic radius, led to an increase of the lattice parameter from *a* = 3.8630 Å for SCF to 3.9795 Å in the case of BSCF [34]. Furthermore, the oxygen desorption at temperatures 300 - 600 °C due to Co^{4+}/Fe^{4+} to Co^{3+}/Fe^{3+} valence state reduction which appears to follow the reaction:

$$2Me^{3+} + O_2^{2-} \rightarrow 2Me^{2+} + ½\, O_2\, (g)$$

is less likely in case of BSCF [34] (Figure 7), which implies a better stability resulting in reduction of the chemical expansion of BSCF compared to SCF membranes.

Note that a second oxygen desorption peak for BSCF at about 850 – 900 °C could be related to cobalt reduction from Co^{3+} to Co^{2+} [30, 34, 35] following the reaction:

$$2Co^{3+} + O_2^{2-} \rightarrow 2Co^{2+} + ½\, O_2\, (g),$$

which might be another factor influencing the mechanical properties of BSCF.

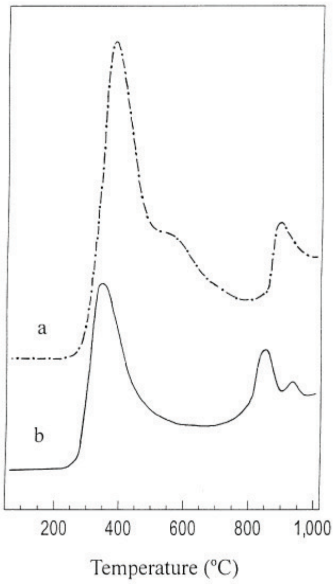

Figure 7. O_2-TDP results showing oxygen desorption in : a) SCF, b)BSCF [34].

These results from literature suggest that BSCF based compounds are promising candidates for oxygen separation membranes in the OXYFUEL process, and further development of dense oxygen transport membranes should be based on this class of materials.

1.3. Permeation efficiency of various perovskite materials

As already discussed in chapter 1.2, a major advantage of BSCF in comparison to SCF and other perovskite compounds is the relatively high oxygen permeation at intermediate temperatures (850 – 900 °C) [11].

A compilation of permeation rates of different materials by Vente et al. [13] for temperatures 1000 °C and 700 °C is shown in Figure 8 and Figure 9, respectively. The oxygen permeability at 1000 °C is similar for SCF and BSCF. Smaller values were observed for LSCF. However, this situation changes, when the operating temperature is decreased to 700 °C. At this temperature, the permeation rate for BSCF is higher than for SCF, and the oxygen fluxes of BSCF and SCF differ by a factor of two when oxygen partial pressure at the feed side reaches 1 bar. Such a large difference is a result of the structural instability of SCF below 790 °C and reflects the coexistence of cubic and brownmillerite – like structure (Figure 5); the latter cannot permeate oxygen.

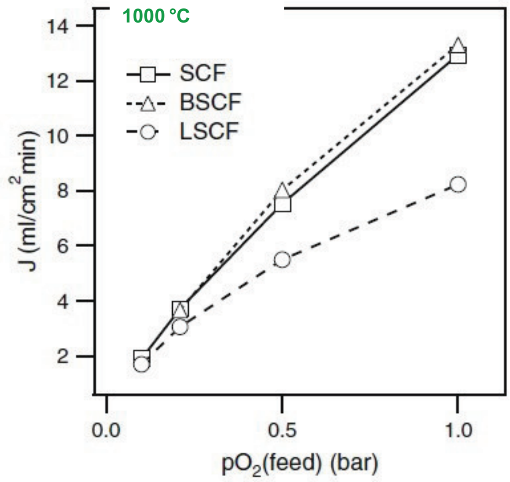

Figure 8. Comparison of permeation rates of SCF based components at 1000 °C [13]. The pO_2 at sweep side was dependent from oxygen flux and varied between 0.02 to 0.28 bar.

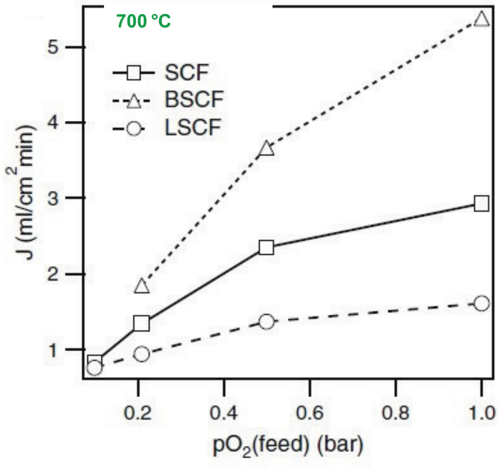

Figure 9. Comparison of oxygen permeation of SCF based components at 700 °C [13]. The pO$_2$ at sweep side was dependent from oxygen flux and varied between 0.02 to 0.28 bar.

Note that permeation of LSCF is also affected by a phase transformation (from rhomboedrical to cubic) [36], whereas no phase transition was detected for BSCF [32].

A comprehensive compilation of available permeation data for MIEC materials has been reported by Sunarso et al. [11]. Here only selected examples will be discussed. All data presented in Table 1 correspond to results obtained on disc-shaped specimens. It should be taken into consideration that the tests were not always carried out under identical conditions (e.g. driving forces due to different oxygen partial pressure gradients across the wall thickness) which might have affected the permeation rate.

For example Shao et al. [30] carried out investigation on the effect of Ba doping in SCF. Optimized Ba to Sr ratios were found to be 1:1 or 0.3:0.7, where the highest increase of oxygen permeation (comparing to SCF) was obtained (Figure 10). Further increase of barium content beyond 70 % results in a suppression of oxygen release at around 500 °C (oxygen peak in the TDP plot disappears) [30]. Moreover, measureable permeation starts at around 750 – 800 °C, which corresponds to the appearance of large oxygen desorption peak in this temperature range [30]. This behavior might indicate the existence of a non-perovskite structure which reduces the permeation below 800 °C. In fact, this was confirmed in [37], where for as-synthesized BSCF samples with Ba content higher than 60 %, an additional set of peaks in the XRD results was found, indicating the presence of phases different from the cubic polymorph. Note that oxygen permeation behavior for BSCF with Ba content higher than 70 % is similar to the behavior of the $SrCoO_{3-\delta}$ component, which confirms that a phase transition takes place.

Table 1. Oxygen permeation trough different disc shaped perovskite-type membranes.

Material	T [°C]	JO_2 [$mol\cdot s^{-1}\cdot cm^{-2}$]	thickness [mm]	Reference
$BaBi_{0.5}Co_{0.2}Fe_{0.3}O_{3-\delta}$	925	$5.6\cdot10^{-7}$	1.5	[38]
$BaCe_{0.4}Fe_{0.6}O_{3-\delta}$	950	$1.7\cdot10^{-7}$	1.5	[39]
$BaCo_{0.4}Fe_{0.5}Zr_{0.1}O_{3-\delta}$	950	$6.8\cdot10^{-7}$	1	[40]
$Ba_{0.5}Sr_{0.5}Co_{0.8}Fe_{0.2}O_{3-\delta}$	900	$1.6\cdot10^{-7}$	1.8	[34]
$Ba_{0.5}Sr_{0.5}Zn_{0.2}Fe_{0.8}O_{3-\delta}$	975	$2.6\cdot10^{-6}$	1.45	[41]
$BaTi_{0.2}Co_{0.4}Fe_{0.4}O_{3-\delta}$	950	$6.7\cdot10^{-6}$	2	[42]
$CaTi_{0.8}Fe_{0.2}O_{3-\delta}$	1100	$3.3\cdot10^{-8}$	2.5	[43]
$La_{0.4}Ba_{0.6}Co_{0.2}Fe_{0.8}O_{3-\delta}$	900	$5.4\cdot10^{-7}$	0.55	[44]
$La_{0.6}Na_{0.4}Co_{0.8}Fe_{0.2}O_{3-\delta}$	860	$2.0\cdot10^{-7}$	1.5	[45]
$La_{0.6}Sr_{0.4}CoO_{3-\delta}$	870	$3.8\cdot10^{-7}$	1	[46]
$La_{0.6}Sr_{0.4}Co_{0.8}Fe_{0.2}O_{3-\delta}$	860	$4.6\cdot10^{-7}$	1.5	[45]
$La_{0.6}Sr_{0.4}Co_{0.8}Ni_{0.2}O_{3-\delta}$	860	$1.1\cdot10^{-6}$	1.5	[45]
$La_{0.6}Sr_{0.4}FeO_{3-\delta}$	1000	$2.6\cdot10^{-7}$	1	[47]
$SrCoO_{3-\delta}$	1000	$3.4\cdot10^{-7}$	1	[31]
$SrCo_{0.8}Fe_{0.2}O_{3-\delta}$	850	$1.7\cdot10^{-7}$	1	[31]
$SrCo_{0.4}Fe_{0.6}O_{3-\delta}$	1100	$1.5\cdot10^{-6}$	1	[46]
$Sr_{0.65}La_{0.35}CoO_{3-\delta}$	880	$2.5\cdot10^{-7}$	1.4	[48]
$Y_{0.1}Ba_{0.9}CoO_{3-\delta}$	900	$2.7\cdot10^{-7}$	2	[49]

According to Lim et al. [50] and Chen et al. [51], an increase of the Fe content in BSCF decreases the thermal expansion coefficient as well as oxygen permeation. In this case, due to the lower oxygen diffusivity caused by the smaller amounts of oxygen vacancies the rate determining mechanism of oxygen permeation appeared to be changed from surface exchange to bulk diffusion.

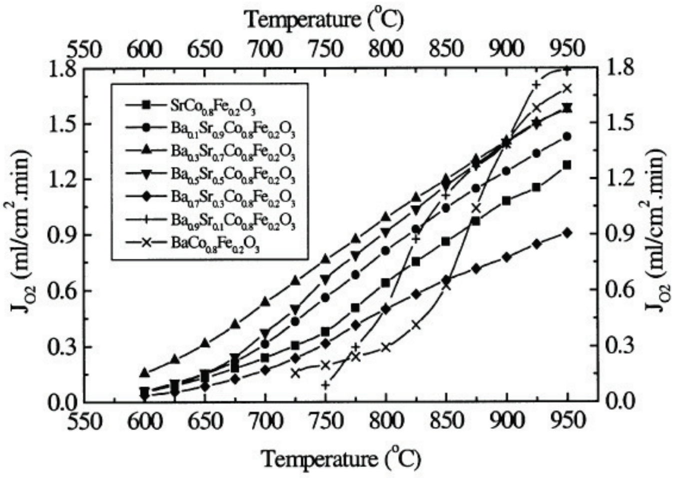

Figure 10. Permeation rates for $Ba_xSr_{1-x}Co_{0.8}Fe_{0.2}O_3$ materials [30].

Although promising permeation values were reported in the literature for BSCF, but recent long-term permeation investigations performed in the intermediate temperature range revealed a degradation of the permeation properties. Also kinetic demixing under high oxygen pressure gradients was reported [13, 52].

1.3.1. **Permeation stability**

Despite of the very high and, in the investigated time frame, stable oxygen permeation flux at 850 °C [34] and above, a significant and continuous decrease of oxygen permeation with time below this temperature was found in Refs [34, 52] (Figure 11).

Particularly at 825 °C the authors [34] report a degradation of permeation rate by about 35 % within 400 h of operation. An even larger drop (factor 5.6) is observed for the same operation time at 750 °C. The reported permeation drop was related to decomposition effects (hexagonally structured phase forms a barrier for the diffusion of oxygen ions). It should be emphasized, that no steady state in permeation is reached even after 400 h at 750 and 825 °C.

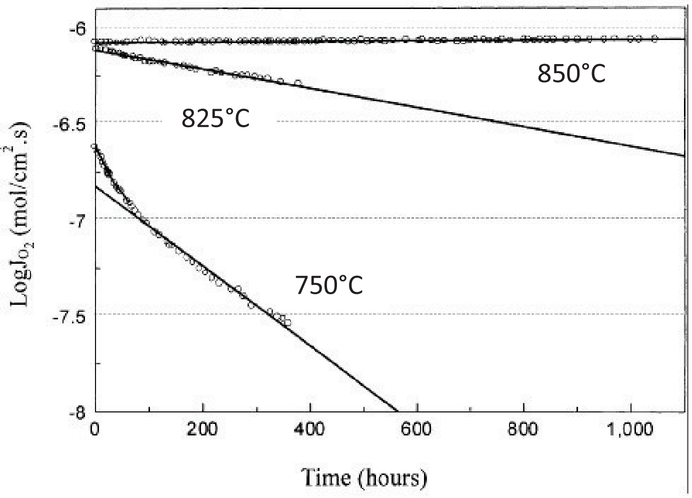

Figure 11. Time dependency of oxygen permeation for BSCF at different temperatures. At 850 °C the permeation is constant due to the stable one phase structure (a). A small decrease is visible at 825 °C (b), where decomposition is observed. A significant drop is visible for 750 °C due to fast formation of a hexagonal phase (c) [34].

Note that initial, short term phase stability analyses for the BSCF, mentioned in section 1.2, did not permit the observation of the rather slow, partial cubic to hexagonal polymorph transition taking place in BSCF at intermediate temperatures [13, 37, 53, 54].

To obtain a more clear picture of the degradation mechanism, Shao et al. [34] also carried out XRD investigation on specimens after permeation tests at 750 °C, which revealed the presence of a secondary phase with chemical composition $BaCoO_2$, created according to the reaction:

$$Ba_{0.5}Sr_{0.5}Co_{0.8}Fe_{0.2}O_{3-\delta} \rightarrow BaCoO_2 + SrCo_{0.6}Fe_{0.4}O_{3-\delta}$$

In this case, coexistence of three phases takes place: cubic BSCF, hexagonal $BaCoO_2$ and $SrCo_{0.6}Fe_{0.4}O_{3-\delta}$, which might, similarly to $SrCo_{0.8}Fe_{0.2}O_{3-\delta}$, (Figure 5), undergo a brownmillerite-like structural change at low oxygen partial pressures. This could be the reason of the observation that only cubic and hexagonal phase coexistence has been reported after annealing in air [55, 56] and additionally a rhomboidal structure was found after permeation tests [57, 58].

The transition described above is reported to be reversible [34]. This was confirmed with additional permeation experiments on samples after permeation test for 300 h at 750 °C. In this case, the specimen was annealed at 900 °C and the permeation was measured at this temperature to check whether the permeation flux can recover after the initial phase transition. A steady state permeation level (at a value close to the initial performance) was obtained after about 80 h, i.e. a three times shorter period than necessary for the initial degradation decrease at 750 °C.

Niedrig et al. [55] investigated the formation kinetics of the hexagonal phase at 800 °C by XRD, and claimed that after about 45 days at 800 °C 90 % of the saturation level was reached for the transformation of cubic phase to a hexagonal phase. This implies that a steady state of permeation should be reached after less than 1000 h at 800 °C.

Microstructural investigation related to the problem of intermediate-temperature BSCF instability and phase transition kinetics performed within the present work will be discussed in section 3.2, “microstructure after heat treatment”.

1.4. BSCF instability in CO_2 environment

The high oxygen permeation, which is the major advantage of BSCF cannot be utilized in CO_2 – containing atmospheres, since the material possesses a low stability in the vicinity CO_2 and microstructural changes take place [20, 35, 59, 60] that result in a strong decrease of the oxygen flux. In fact, CO_2 stability tests performed by Schulz et al. [59] on uncoated as well as 130 and 290 nm thick $Ce_{0.2}Gd_{0.8}O_2$ (CGO) coated BSCF membranes revealed a strong influence of carbon dioxide on the permeation, implying that even the CGO coating does not improve the situation much. During the experiment, mixtures of CO_2 in N_2 were used as a sweep gas. CO_2 concentrations were varied from 0 to 100 %. Oxygen permeability data collected after 4 h of dwell time at a constant temperature of 900 °C are presented in Figure 12. The test temperature ensured the absence of effects related to phase transformation at the grain boundaries below 850 °C.

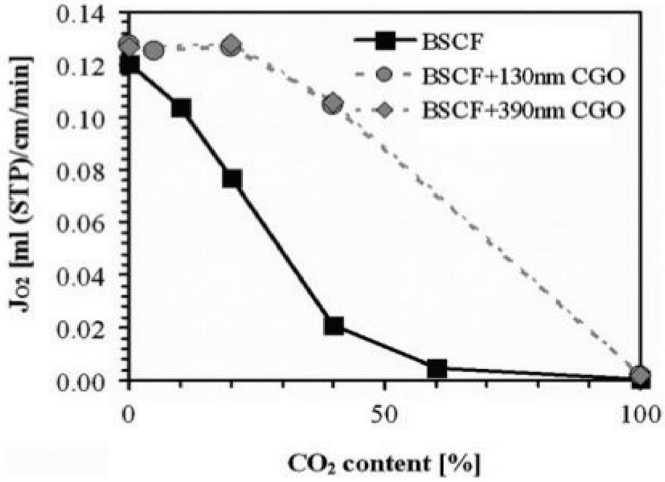

Figure 12. Oxygen permeation drop in presence of CO_2 [59].

The oxygen permeation rates, obtained for sweep gas containing 0 % of CO_2, were chosen as a reference value. An oxygen permeation drop of ~ 12 % was observed for uncoated BSCF specimen when CO_2 concentration was increased to ~10 %. Removal of CO_2 from the sweep gas caused fast resumption of the oxygen permeation to the initial values. Permeation recovery after change of sweep gas from pure CO_2 to helium at 875 °C was also confirmed by Arnold et al. [60].

Degradation of BSCF material in CO_2-containing atmospheres was also observed in other reports. Engels et al. [61] reported a permeation drop for tubular BSCF membranes after ~ 50 min at 850 °C when 15 % CO_2 was added to the sweep gas. Degradation accelerates along with the increasing amount of CO_2. In the case of pure CO_2, permeation decreases to zero within about 15 min. However, after switching to pure helium sweep gas, permeation recovers within similar time. After the permeation test performed in CO_2-containing sweep gas, a needle-structured $Ba_xSr_{1-x}CO_3$ layer was observed on the sweep side of the membrane (Figure 13) [61].

In fact, according to Yi et al. [62] the BSCF decomposition in CO_2 environment occurs according to following reaction:

$$\mathrm{Ba_{0.5}Sr_{0.5}Co_{0.8}Fe_{0.2}O_{3-\delta}} + \mathrm{CO_2} \rightarrow \mathrm{Ba_{0.5}Sr_{0.5}CO_3} + 0.8\mathrm{CoO} + \frac{0.2}{3}\mathrm{Fe_3O_4} + \ \frac{1.4}{3} - \frac{\delta}{2}\ \mathrm{O_2}$$

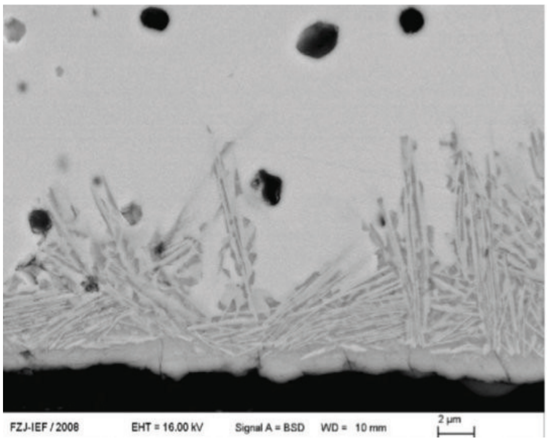

Figure 13. Degradation of the BSCF surface in the presence of CO_2 [61].

Yan et al. [20] observed a decrease of the performance of a BSCF 5528 cathode for a low temperature solid oxide fuel cell (LT-SOFC) even though only 1% of CO_2 was added to the cathode gas compartment. At 600 °C the current density decreased by about 50 % after 5 minutes of operation in the presence of CO_2. In their work the smallest drop of the current density was observed for $SrCo_{0.8}Fe_{0.2}O_{3-\delta}$ (SCF), whereas the strongest decrease (down to 0 after ~ 10 min operation) was observed for $BaCo_{0.8}Fe_{0.2}O_{3-\delta}$ (BCF). Hence, the resistance of BSCF against CO_2 appears to decrease with decreasing Sr content. Increasing the Sr amount is, however, not the solution for improving the CO_2 resistance of BSCF materials, since it results in higher chemical expansion and instability of perovskite structure as reported for SCF (Figure 5 and Figure 6).

Furthermore, Zeng et al. [63] revealed that partial substitution of B-side cations by Ti in SCF increases the stability of this material against CO_2, however, on the expense of a decrease of the oxygen permeation.

In CO_2-temperature programmed desorption experiments Faraji et al. [16] reported CO_2 desorption to take place above 600 °C due to the decomposition of carbonates on the surface. Carbonates are unstable at high temperatures, and therefore, upon CO_2 stability tests they immediately decompose when the sweep gas is changed from CO_2 - containing to pure nitrogen and the oxygen flux is recovered after complete carbonate decomposition.

However, instability of BSCF in CO_2 atmosphere should not constitute a problem in the work carried out within the framework of the current MEM-BRAIN project [5] since the membranes will have no contact with CO_2 in the OXYMEM process (CO_2 amount in air is expected to be too small to cause any degradation).

1.5. Thermal and chemical expansion

To understand the thermal and chemical expansion behavior of materials, the interaction forces between two atoms should be taken into consideration.

In Figure 14, the dependency of the inter-atomic distance on potential energy between two atoms is shown.

The potential energy between two atoms depends on attractive as well as repulsive forces. When distance between two atoms is very large, both forces are equal to zero. Higher influence of attractive forces on the atoms is visible in the range of larger atomic distances (between r_0 and r_3), whereas governing of repulsive forces is noticed at distances $r < r_0$. These two opposite forces increase asymmetrically, causing a minimum of potential energy, as indicated by r_0 in Figure 14. Moreover, the influence of temperature on inter-nuclear separation gives rise to thermal expansion. Point c represents the situation at a temperature of absolute zero, in which atoms do not oscillate due to lack of kinetic energy (equilibrium inter-nuclear separation, r_0). When the temperature rises to T_1, atoms oscillate in the range of *a'* and *b'* positions. During further temperature increment (to T_2), atoms will oscillate with larger amplitude (range of a*"* to b*"*). Their oscillations are unsymmetrical due to asymmetric distribution of potential energy. Higher inclinations in longer atomic distance direction will occur and equilibrium inter-nuclear separation will be shifted to the right (point r_3), resulting in thermal expansion.

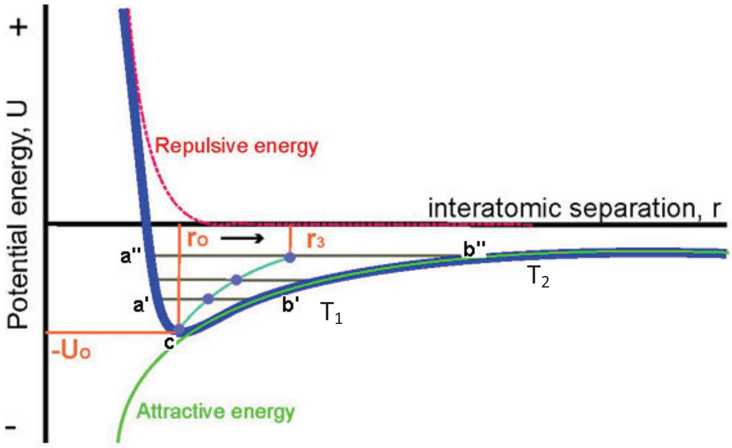

Figure 14. Potential energy between two atoms and changes of the interatomic separation ($r_0 - r_3$) with temperature.

Those thermally induced changes in the lattice constant of the material can be described by the linear thermal expansion coefficient (TEC), α:

$$\alpha = \frac{\Delta l}{l_0}\frac{1}{\Delta T}$$

Equation 1.

where: $\Delta l = l - l_0$, l_0- initial length, l – final length, and ΔT – temperature difference.

In the case of perovskite materials, which are able to transport oxygen, in addition to the thermal -, also a chemical expansion is present. This phenomenon is associated with the increasing oxygen vacancy concentration by the virtue of oxygen release from the crystal lattice upon heating. In order to maintain its charge neutrality, a reduction of cations to the lower valence state takes place. Since lower valence cations feature larger atomic radii, this phenomenon was reported to be one of the main reasons for lattice expansion during oxygen release [64]. Similar as in the case of doping of the perovskite with higher ionic radius components (as in case of Ba-doped SCF described earlier) as well as with lower valence state components, this causes an increase of oxygen vacancies concentration [64, 65]. Another possible reason for the chemical expansion occurring in MIEC materials is the repulsion between equally charged cations neighboring each other resulting from the removal of separating oxygen ions [64, 66].

The TEC of BSCF was measured inter alia by Huang [26]. The scientific TEC used in this case permits a better assessment of the influence of events at a particular temperature and is defined as:

$$\alpha_{Sci} = \frac{1}{l}\frac{dl}{dT}$$

Equation 2.

where: l – length, and T – temperature.

In the results of α_{sci} measurements performed for BSCF (Figure 15) [26], a transition can be observed in the temperature range of 400 – 600 °C, where the chemical expansion of BSCF material indicates an abrupt increase of TEC to $24 \cdot 10^{-6}$ K^{-1}.

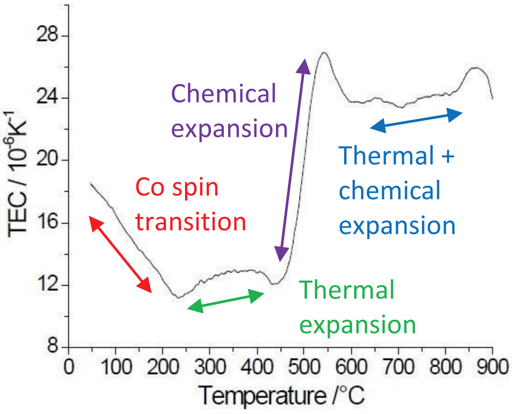

Figure 15. Temperature dependency of TEC coefficient for the BSCF and suggested scheme of events [26].

Results obtained by DTA (Figure 16) [16] indicated that for BSCF oxygen release in reducing atmosphere (nitrogen) starts at around 450 °C and a higher amount of oxygen is released under nitrogen than in air, where the chemical expansion starts at ~ 500 °C, which confirms Huang's results.

Note that temperature programmed desorption of oxygen (O_2-TDP) tests performed for BSCF [34] (Figure 7) reveal an oxygen release peak at around 350 °C which is also in agreement with Huang's results. Slight differences between these temperatures can be a result of errors in temperature measurement and slightly different chemical composition or specimen state. The additional a small peak present in Figure 15 at around 850 °C corresponds to the one obtained at the same temperature during O_2-TDP measurements [34] (Figure 7).

The decrease of TEC visible in Figure 15 below 200 °C can be related to spin transition of Co ions [26].

The chemical expansion of BSCF in air and under argon atmosphere was also investigated by Kriegel et al. [27] (Figure 17).

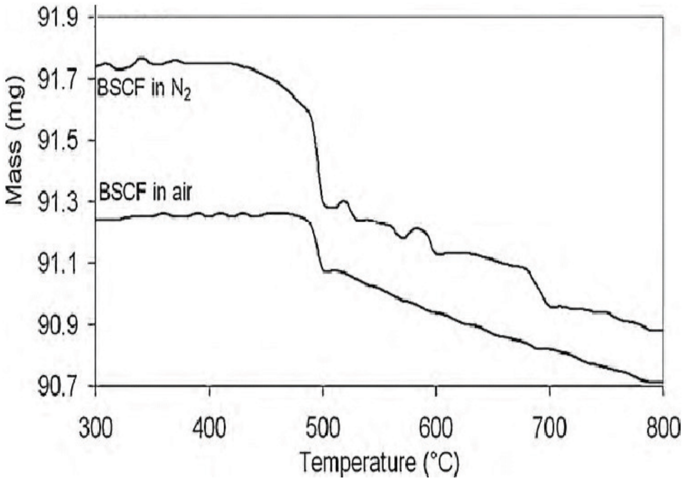

Figure 16. Temperature dependency of TG mass changes for the BSCF [16].

Starting temperature of the oxygen release in air was determined to ~ 550 °C and the process was found to be reversible: specimen's dimensions recovered to their initial values upon cooling in air. In argon atmosphere, chemical expansion was larger (as illustrated in Figure 17) due to the stronger oxygen release. This was an irreversible phenomenon, since oxygen couldn't be absorbed upon cooling due to the limited availability of oxygen in the surrounding atmosphere. Hence, these specimens did not recover to their initial dimension.

Note that a chemical expansion effect was noticed also during creep tests conducted in frame of the current thesis (see section 3.5.1).

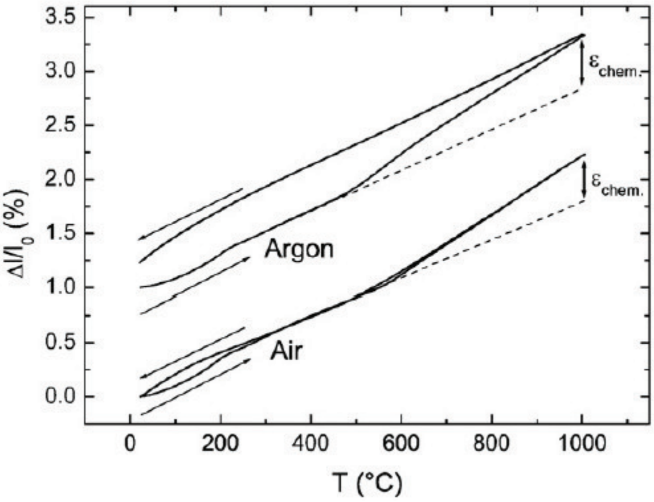

Figure 17. Thermal and chemical expansion of the BSCF measured in air and argon. In case of air, stoichiometry changes are reversible [27].

In Table 2, thermal and chemical expansion coefficients for BSCF are presented [27]. An increase of the chemical expansion is observed due to oxygen stoichiometry changes when the annealing temperature is increased at an oxygen partial pressure of 10^{-5} bar. As might be expected more oxygen can be released from the lattice at higher temperatures.

Table 2. TEC and chemical expansion for BSCF specimens annealed at *pO_2* of 10^{-5} bar at different temperatures [27].

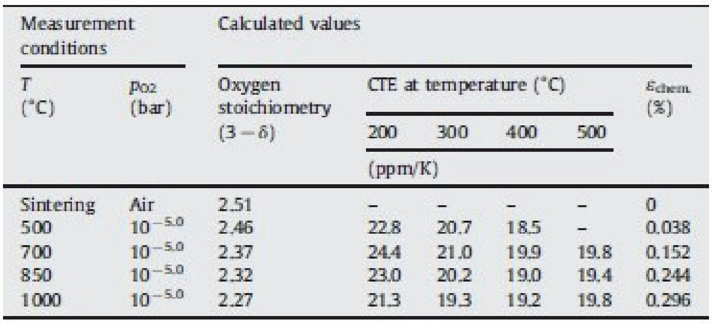

Measurement conditions		Calculated values					
T (°C)	p_{O2} (bar)	Oxygen stoichiometry $(3-\delta)$	CTE at temperature (°C)				$\varepsilon_{chem.}$ (%)
			200	300	400	500	
			(ppm/K)				
Sintering	Air	2.51	–	–	–	–	0
500	$10^{-5.0}$	2.46	22.8	20.7	18.5	–	0.038
700	$10^{-5.0}$	2.37	24.4	21.0	19.9	19.8	0.152
850	$10^{-5.0}$	2.32	23.0	20.2	19.0	19.4	0.244
1000	$10^{-5.0}$	2.27	21.3	19.3	19.2	19.8	0.296

Figure 18 illustrates (as a supplement to Table 2) the influence of pO_2 and temperature on the oxygen stoichiometry of BSCF [67].

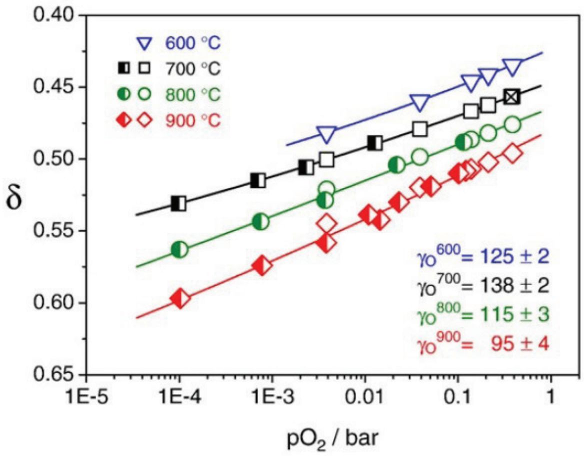

Figure 18. Dependency of oxygen stoichiometry on the oxygen partial pressure [67].

The temperature influence on the oxygen stoichiometry in an oxygen rich atmosphere is weaker than under reduced *pO_2*. In case of vacuum, similar temperature difference causes a larger stoichiometry change due to faster oxygen release. A similar influence of the atmosphere might also be expected in case of creep tests (section 3.5.1), where higher amount of vacancies (acting as diffusion paths for cations) might increase the creep rate.

1.6. **Mechanical properties of ceramic membranes**

Oxygen separation units with a large number of membrane components have to be operated at elevated temperatures (about 800 °C) under severe conditions, i.e. large pressures gradients [68, 69], which might induce high mechanical stresses. Material integrity ensuring long component life must be maintained not only during operation but also during start-up and shut-down procedures. Knowledge of the mechanical properties depending on temperature and environment for each component of the separation unit are necessary to create reasonable systems with high service reliability over long periods.

Young's modulus (E) as well as fracture strength (σ_f) and toughness (K) of the particular materials are the basic mechanical properties critical for the evaluation of the system reliability. They should give information on the materials behavior in a wide range of possible operation conditions (e.g. temperature, pO_2).

Note that mechanical properties are changing with temperature, which also need to be taken into consideration during component design – for example, a tensile stress of 50 MPa, introduced to the membrane by mounting, which can be safe for the component at room temperatures, can cause failure of whole component during first start-up or shut-down if the fracture strength decreases at elevated temperatures.

Although thin layer concepts are not considered in the current work it should be noted that the general tendency to decrease membrane thicknesses in order to obtain high oxygen fluxes results in a decreasing ability of the components to sustain mechanical loads, although the fracture stress will not necessarily be affected. Membrane concepts based on thin layers require, therefore, the use of substrate materials [70] that provide a mechanical support for the separation unit. The latter shouldn't, however, cause a significant permeation drop for the system, requiring the use of porous substrates.

1.6.1. **Young’s modulus**

Initially, the attention has to be focused on the Young’s modulus (E):

$$E = \frac{\sigma}{\varepsilon_e}$$

Equation 3.

where: $\boldsymbol{\sigma}$ – stress, $\boldsymbol{\varepsilon}_e$- elastic strain,

which describes the deformation behavior in the elastic regime and hence, permits an assessment of elastic stresses under a particular strain state. High Young’s moduli assure small elastic deformations under a given mechanical stress (components are stiff). Membrane material with lower Young’s modulus has higher ability to comply to strain induced by inhomogeneous thermal / chemical expansion leading to lower stresses and hence for a particular strength to a higher survival probability.

Values of the Young’s modulus for selected perovskite materials are given in Table 3. A detailed discussion of the effect of compositional changes on the modulus would require a consideration of preparation conditions and especially porosities that can lead to a strong decrease of Young’s modulus. Hence, the discussion is limited to some general aspects related to the current work.

The Young’s modulus of ceramics has, as is the case for most materials, the general tendency to decrease with increasing temperature [71] due to increase of the lattice constant (Figure 14). However, Huang et al. [72] reported that Young’s modulus of BSCF at room temperature was ~ 63 GPa, whereas at 200 °C it reached a minimum of 45 GPa, that was attributed to a spin transition of Co-atoms.

The Young’s modulus had a local maximum of 52 GPa at 400 °C and subsequently decreased slightly to 48 GPa at 800 °C. This kind of temperature dependence was confirmed for porous BSCF in Ref. [70].

Table 3. Young's moduli for various perovskite materials.

Material	E [GPa]	Temperature [°C]	Reference
$Ba_{0.5}Sr_{0.5}Fe_{0.8}Co_{0.2}O_{3-\delta}$ (porosity 38 %)	33	RT	[70]
$Ba_{0.5}Sr_{0.5}Fe_{0.8}Co_{0.2}O_{3-\delta}$	63	RT	[72]
	45	200	
	52	400	
	48	800	
$La_{0.6}Sr_{0.4}Fe_{0.8}Co_{0.2}O_{3-\delta}$	150	RT	[73]
$La_{0.5}Sr_{0.5}Fe_{0.5}Co_{0.5}O_{3-\delta}$	115	RT	[71]
	160	800	
	120	1000	
$La_{0.5}Sr_{0.5}Fe_{0.25}Co_{0.75}O_{3-\delta}$	115	RT	
	176	400	
	160	800	
$La_{0.5}Sr_{0.5}CoO_{3-\delta}$	122	RT	
	157	800	
$LaCoO_3$ (porosity 17%)	8	RT	[74]
$La_{0.8}Ca_{0.2}CoO_{3-\delta}$	112	RT	
$La_{0.8}Sr_{0.2}CoO_{3-\delta}$ (porosity 10 %)	64	RT	
$LaFeO_3$	213	RT	[75]
	206	800	
$BaZrO_3$	240	RT	[76]
	238	480	
$La_{0.8}Sr_{0.2}Fe_{0.7}Ga_{0.3}O_{3-\delta}$	120	RT	[77]
	86	400	
$La_{0.8}Sr_{0.2}FeO_{3-\delta}$	170	RT	
	110	340	

$La_{0.5}Sr_{0.5}CoO_{3-\delta}$ has reported to have a two times higher Young's modulus than BSCF. Doping with Fe decreases the Young's modulus at RT slightly. Changing La-Sr ratio in LSCF seems to have insignificant effect on Young's modulus at RT [73].

1.6.2. **Fracture strength and fracture toughness**

The second important property for the mechanical reliability assessment of membranes is the fracture strength, which is a statistical parameter coupling failure probability and the stress the material can withstand at fracture. Fracture in a ceramic material will occur starting from an initial defect when the bonds between atoms are broken [78]. For this, the separation distance between two atoms needs to be increased up to a value higher than the cohesive force, which depends on Young's modulus (which is correlated with the attractive force, see Figure 14), the surface energy and the equilibrium distance between atoms.

The theoretical cohesive stress is given by the following equation [78]:

$$\sigma_C = \sqrt{\frac{E\gamma_S}{x_0}}$$

Equation 4.

Where: *E*- Young's modulus, γ_S – surface energy, x_0 – equilibrium separation of atoms.

Therefore, at elevated temperatures, where inter-nuclear separation is higher, and stiffness is lower, the cohesive stress usually is lower.

However, the fracture stress of ceramic materials is mainly governed by the size and location of strength limiting flaws. They can be located at a specimen's edge due to cutting effects, as well as at surface or close to the surface, if preparation related differences between surface and bulk exist, or simply somewhere in the volume [79]. In case of bending tests (e.g. ring-on-ring tests for discs and 3- /4- point bending on beam), where maximal tensile stresses exist at one of the surfaces, the probability of failure due to flaws close to tensile surfaces will be highest. The effect of the defect size distribution related scatter in the fracture stress data can be assessed statistically by a Weibull distribution leading to a characteristic strength that is representative for the fracture stress at which 63 % of the specimens will fail and a Weibull modulus that the permits to calculate the fracture stress for any acceptable failure probability.

Table 4. Fracture stress of various perovskite materials.

Material	Fracture stress [MPa]	Reference
$Ba_{0.5}Sr_{0.5}Co_{0.8}Fe_{0.2}O_{3-\delta}$	98 ± 8	[26]
$LaFeO_3$	202 ± 18	[75]
$LaCoO_3$	86	[64]
$La_{0.8}Sr_{0.2}CoO_{3-\delta}$	76	[74]
$La_{0.5}Sr_{0.5}CoO_{3-\delta}$	138	[71]
$La_{0.8}Sr_{0.2}CrO_{3-\delta}$	49	[80]
$La_{0.5}Sr_{0.5}Fe_{0.5}Co_{0.5}O_{3-\delta}$	128	[71]
$La_{0.5}Sr_{0.5}Fe_{0.25}Co_{0.75}O_{3-\delta}$	71	[71]
$La_{0.8}Sr_{0.2}Fe_{0.8}Co_{0.2}O_{3-\delta}$	165	[73]
$La_{0.6}Sr_{0.4}Fe_{0.8}Co_{0.2}O_{3-\delta}$	155	[73]
$La_{0.4}Sr_{0.6}Fe_{0.8}Co_{0.2}O_{3-\delta}$	50	[73]
$La_{0.2}Sr_{0.8}Fe_{0.8}Co_{0.2}O_{3-\delta}$	40	[73]
$La_{0.7}Sr_{0.3}O_{3-\delta}$	234	[81]
$La_{0.8}Ca_{0.2}CoO_{3-\delta}$	150	[74]
$La_{0.75}Ca_{0.25}CrO_{3-\delta}$	122 ± 26	[82]
$La_{0.7}Ca_{0.3}CrO_{3-\delta}$	256	[81]
$La_{0.2}Sr_{0.8}Cr_{0.2}Fe_{0.8}O_{3-\delta}$	340	[83]
$La_{0.6}Sr_{0.4}Cr_{0.2}Fe_{0.8}O_{3-\delta}$	138	[84]
$La_{0.8}Sr_{0.2}Cr_{0.2}Fe_{0.8}O_{3-\delta}$	243	[84]
$La_{0.5}Sr_{0.5}MnO_{3-\delta}$	78	[85]
$La_{0.875}Sr_{0.125}MnO_{3-\delta}$	164	[86]
$La_{0.5}Sr_{0.5}Mn_{0.96}Co_{0.04}O_{3-\delta}$	38	[85]
$LaCr_{0.9}Mg_{0.1}O_3$	140	[87]
$La_{0.7}Sr_{0.3}Cr_{0.8}Fe_{0.2}O_{3-\delta}$	230	[88]

An accurate assessment of these parameters requires a significant number of specimens to be tested (according to DIN EN 843-5 [89] around 30). It has to be noted that, due to statistical aspects of the likelihood of large defects in a discrete volume or surface area the strength determined at specimens of a certain size needs to be recalculated for the size of the real component.

Average fracture stress data of various perovskites are summarized in Table 4.

Due to the large number of influencing factors (e.g. different testing methods, as well as different specimens geometries, densities, porosity, surface conditions, and various strength limiting flaw distribution), those data will not be discussed here in detail and only serve as a guide to the range of strength values possible for such materials.

With respect to the current work the results of Huang [72] can be used for comparison, who reported that the average fracture stress for BSCF at room temperature reaches a value of 98 MPa, which is almost 30 % higher than for $La_{0.5}Sr_{0.5}Co_{0.75}Fe_{0.25}O_{3-\delta}$ [71]. Similar as the Young's modulus the fracture stress of BSCF decreases with increasing temperature to 50 MPa at 400 °C. It recovers, however, with further temperature increase and reaches ~ 80 MPa at 800 °C.

The fracture toughness describes the materials' resistance to unstable crack propagation and fracture.

A comparison of RT-fracture toughness data selected from literature for various potential membrane materials is summarized in Table 5.

Table 5. Fracture toughness of various perovskite materials.

Material	Fracture toughness [$MPa \cdot m^{-1/2}$]	Reference
$LaCr_{0.9}Mg_{0.1}O_3$	2.8	[87]
$LaFeO_3$	2.5	[75]
$La_{0.8}Ca_{0.2}CoO_3$	2.2	[90]
$La_{0.9}Sr_{0.1}Ga_{0.8}Mg_{0.2}O_3$	2.1	[91]
$La_{0.8}Ca_{0.2}CoO_3$	1.9	[92]
$BaZrO_3$	1.5	[93]
$La_{0.5}Sr_{0.5}CoO_3$	1.5	[94]
$La_{0.5}Sr_{0.5}Fe_{0.5}Co_{0.5}O_3$	1.2	[94]
$LaCoO_3$	1.2	[64]
BSCF	1	[72]

$LaFeO_3$ shows a high fracture toughness value (2.5 $MPa \cdot m^{-1/2}$). Complete replacement of Fe by Co results in a decrease of fracture toughness to 1.2 $MPa \cdot m^{-1/2}$ for $LaCoO_3$. 50 % replacement of La with Sr results in $La_{0.5}Sr_{0.5}CoO_3$ which has a 25 % higher fracture toughness compared to the Sr-free compound. Further modification with Fe resulting in the $La_{0.5}Sr_{0.5}Fe_{0.5}Co_{0.5}O_3$ (LSCF 5555) compound, leads to decreased toughness of 1.2 $MPa \cdot m^{-1/2}$, contrary to the case of $LaFeO_3$ (increase of toughness from 1.2 to 2.5 $MPa \cdot m^{-1/2}$ when Co is replaced by Fe). Substitution of 20% of La by Ca has a positive influence on $LaCoO_3$ (toughness increases by about 60 %). BSCF has 20 % lower fracture toughness than LSCF 5555. These changes might be related to the different atomic radii of dopants, causing change of intermolecular distances as well as lattice deformation which may influence fracture toughness.

Note that Huang [72] performed indentation fracture toughness measurements for dense BSCF material in the temperature range from RT up to 350 °C. A strong decrease (from 1 to 0.4 $MPa \cdot m^{-1/2}$) was observed from RT to 100 °C and values remained then constant up to 350 °C. Additional measurements using the indentation strength method, performed by Chanda et al. [95] reveal continuous increase of the toughness when a temperature of 400 °C is exceeded. At around 800 °C, toughness reaches ~ 80 % of value obtained for RT. Note that toughness followed the behavior of fracture stress. Since fracture toughness data are available in literature, in the present work measurements for BSCF were only performed at room temperature.

1.6.3. **Creep properties**

Creep is inelastic deformation occurring at elevated temperature under constant stress, in most cases at a stress that is lower than the material's yield point. It is therefore a monotonous temperature and stress dependent irreversible deformation. In order to assess the creep behavior of a ceramic material experimentally, specimens (for ceramic materials usually cylinders) are typically exposed at elevated temperature to a constant compressive load (tensile creep tests at ceramics have also been reported [96, 97], however there can be severe problems regarding the fixture, especially for extremely brittle materials like BSCF in tensile configuration) while the deformation is measured by displacement sensor.

As a result, strain vs. time plot (creep curve), is obtained. An example is schematically shown in Figure 19 (upper curve corresponds to tensile, the lower one to compressive creep).

The effective strain ($\boldsymbol{\varepsilon}$) is determined from the following equation:

$$\varepsilon = \frac{l_1 - l_0}{l_0}$$

Equation 5.

Where: $\boldsymbol{\varepsilon}$ - is the strain, l_1 - specimen length after certain time of testing and l_0 - initial specimen's length. Note to determine the real strain, l_0 has to be replaced by the actual length at the time *t.*

The primary (transient) creep regime (indicated as "I" on Figure 19) is characterized by continuously decreasing creep rate due to an increase of the creep resistance by deformation-induced changes in microstructure. In the secondary (steady-state) creep regime (II) the deformation rate is constant due to compensation of hardening and softening effects taking place simultaneously. The slope of the curve in this creep regime is used for determination of the steady-state creep rate:

$$\varepsilon = \frac{d\varepsilon}{dt}$$

Equation 6.

In the tertiary creep regime (III), strain rate again changes with time. The balance between deformation and healing processes is unsettled and in tensile creep finally rupture occurs.

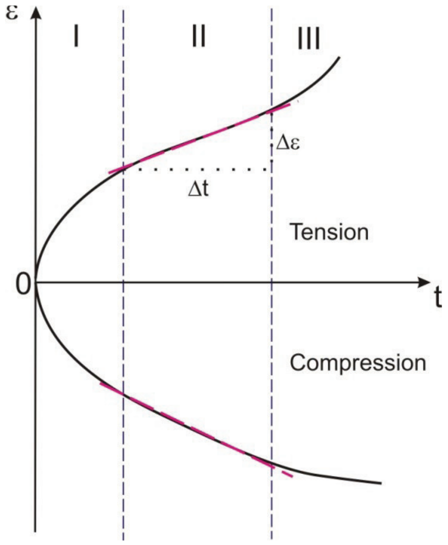

Figure 19. Exemplary time – strain plots of creep tests performed in tension as well as in compression.

The determination of creep parameters is important for high temperature applications involving long operation times, in which creep deformation may contribute on one hand to damage of the membrane but on the other hand to stress relaxation effects that has to be considered in the simulation of actual stress states that might arise during operation and thermal cycling. For example, even a relatively low creep rate equal to $3.2 \cdot 10^{-10}$ s^{-1} results in a creep strain of ~ 1 % per year. This value might be considered as a maximum acceptable strain for membrane application [98].

The parameter dependence of the creep behavior of materials obtained under different conditions (varied σ, pO_2, T) can be described by a steady state creep equation [99]:

$$\varepsilon = A\cdot \ \frac{1}{d}^{\ p} \cdot \ pO_2{}^{\ m}\cdot\sigma^{n}\cdot exp\ \ -\frac{E_a}{RT}$$

Equation 7.

where: A – constant, d - grain size, p – grain size exponent, pO_2 – oxygen partial pressure, m -oxygen partial pressure exponent, n – stress exponent, E_a – activation energy, R – gas constant, σ and T were defined earlier.

The parameters: d, pO_2, σ and T are input conditions of the experiments. The relevant exponents in Equation 7 can be fitted based on experimental results. The detailed procedure of exponents' determination will be given in paragraph 3.5.2. Note that the influence of the oxygen partial pressure on creep might be positive (increase creep rate with increase of oxygen content) as well as negative (increase of creep rate when decrease oxygen content) [100]. In case of oxygen transport membranes, this coefficient should be as close to zero as possible. In this case, creep deformation of a membrane exposed even to a high oxygen gradient will be uniform over the whole cross section. If m is different from 0, creep strain in the cross-section becomes non-uniform leading to additional stresses and faster damage. Another significant parameter is the stress exponent. In case of $n = 1$ diffusion creep is indicated [99, 101]. When $n > 1$, additional mechanisms significantly contribute to creep deformation (e.g. grain boundary sliding or deformation via dislocation movement when $n > 3$). Additional information about creep mechanisms can be obtained from the grain size exponent p, which depends on the type of diffusion process governing creep. Lattice diffusion (Nabarro-Herring creep) is indicated by p approximately equal to 2 [99].

Of course, creep deformation strongly depends on temperature. Especially, creep deformation gets faster with increasing vacancy content in the case of diffusional creep. In case of perovskites, oxygen atoms are released from the lattice at higher temperature, which can further accelerate creep due to increased amount of diffusion paths. In case of $p \approx 3$, Coble creep (grain boundary diffusion) governs deformation [99]. Of course, the above mentioned mechanisms act jointly, however their impact on creep is changing when conditions are varied (e.g. increase of temperature). For this reason, the interpretation of the determined exponents can be difficult. During diffusion governed creep, grains should change their dimensions (growing) and aspect ratio (elongation of grains). When no grain elongation after creep is noticed, and voids along grain boundaries perpendicular to the applied force direction are observed, grain boundary sliding (GBS) is indicated.

A very good microstructure evidence of GBS mechanism present in yttria- and scandia-stabilized zirconia was given by Evans [102]. In Figure 20, reprinted after [102], an example of a microstructure after deformation by grain boundary sliding is presented. Grain boundaries, which are perpendicular to the applied stress direction (marked with arrows), are widened. Grains under compressive stress are deformed perpendicular to the load axis and movement of neighboring grains which results in opening of grain boundaries parallel to the load direction, as presented on Figure 21 [102].

A comparison of apparent activation energies for various perovskite materials was performed by Huang [26]. Activation energies were normalized with respect to the melting point of the material. When the normalized values (E_a/RT_m) were higher than ~ 24, lattice diffusion governs creep, which is usually connected with high value of activation energy (E_a > 400 kJ/mol). When the normalized value is lower than ~ 24, creep is governed by grain boundary diffusion, and activation energies are usually smaller than 400 kJ/mol.

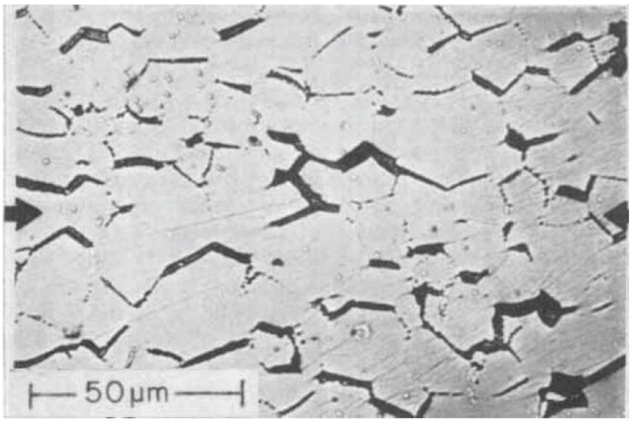

Figure 20. Results of GBS – Grain boundaries perpendicular to load direction are widened [102].

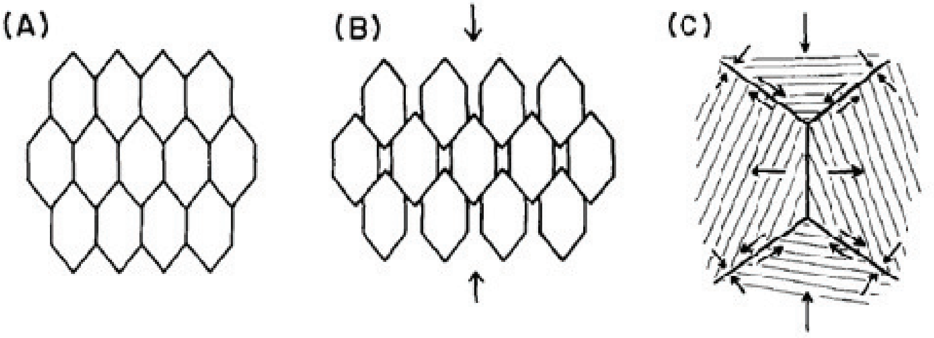

Figure 21. Deformation by grain boundary sliding [102].

Investigations of the creep properties of BSCF5582 were performed by Yi et al. [99]. Experiments were conducted in air in the temperature range from 850 to 950 °C on the material with a grain size of 6.9 µm. During the tests the temperature was kept constant, while the stress was varied from 5 to 20 MPa. The microstructure is not reported in detail, but a small amount of hexagonal phase in the as-received state might be expected. The material was tested at temperatures higher than 825 °C - in the range where the cubic phase is unstable (see section 3.2.1). However some additional amount of hexagonal phase may be created during heating. As mentioned above, the material was tested at constant temperature and with increasing load. This may result in different microstructure states at the beginning of the subsequent load stages (higher amount of hexagonal phase during the test at 5 MPa, whereas during the test at 20 MPa, material may be closer to equilibrium state due to hexagonal phase dissolution). Results of those experiments are given in Table 6. Between 880 °C and 900 °C a transition point was observed, at which pronounced (about one order of magnitude) increase of the creep rates took place (effect is visible in Figure 23, where results for 10 and 15 MPa from Table 6 are plotted). This phenomenon is most probably associated with the phase transition (dissolution of hexagonal phase) taking place in the material.

Table 6. Strain rates (s^{-1}) obtained during creep tests on the BSCF material [99].

T [°C]	Strain rates [s^{-1}] at the stress of :			
	5 MPa	10 MPa	15 MPa	20 MPa
935	$2.1 \cdot 10^{-7}$	$3.7 \cdot 10^{-6}$	$6.1 \cdot 10^{-7}$	-
920	$1.2 \cdot 10^{-7}$	$2.2 \cdot 10^{-7}$	$3.2 \cdot 10^{-7}$	-
900	$9.4 \cdot 10^{-8}$	$1.8 \cdot 10^{-7}$	$3.0 \cdot 10^{-7}$	$4.5 \cdot 10^{-7}$
880	$1.2 \cdot 10^{-8}$	$1.5 \cdot 10^{-8}$	$2.3 \cdot 10^{-8}$	$3.9 \cdot 10^{-8}$
850	$7.2 \cdot 10^{-9}$	$8.7 \cdot 10^{-9}$	$1.3 \cdot 10^{-8}$	$1.6 \cdot 10^{-8}$
800	$2.2 \cdot 10^{-9}$	$3.0 \cdot 10^{-9}$	-	$4.0 \cdot 10^{-9}$

Note that this increase of creep rate at temperatures above 880 °C was accompanied by a small change of activation energy (from 258 ± 37 kJ/mol for $T < 880$ °C to 287 ± 31 kJ/mol for $T > 880$ °C). The activation energy for the diffusion of oxygen in BSCF, reported by Shao et al. [34], is rather low (much below 100 kJ/mol). This suggests that deformation obtained in [99] was governed by cation movement. The normalized activation energy (E_a/RT_m) is ~ 30, which (according to Huang [26]) suggests lattice diffusion. Diffusion governed deformation is also indicated by the stress exponent of 0.75. However, an inverse grain size exponent of 2.45 indicates a similar contribution of grain boundary-, as well as of lattice diffusion to the creep process. The oxygen partial pressure exponent value of $m = 0.63$ indicates a strong influence of the oxygen stoichiometry on materials' creep. The influence of grain boundary sliding (GBS) on creep was not discussed.

From an engineering point of view, the influence of the Ba content on creep BSCF is very interesting; especially due to the influence of Ba on oxygen permeability and BSCF's stability described earlier (Chapter 1.2 and 1.3).

SCF was investigated by Majkic et al. [101]. Results of their experiments, determined in the temperature range from 850 °C to 975 °C for a material with a grain size of 6.8 µm are summarized in Table 7.

The most streaking difference in creep behavior compared to BSCF is a significant change of creep activation energy taking place in SCF at around 925 °C [101], visible in Figure 23, where results for 10 and 15 MPa from Table 7 are plotted.

Table 7. Strain rates (s^{-1}) obtained during creep tests on the SCF material [101].

Stress	Strain rates [s^{-1}] at the temperature of:					
[MPa]	850 °C	875 °C	900 °C	925 °C	950 °C	975 °C
10	$2.2 \cdot 10^{-7}$	$1.3 \cdot 10^{-6}$	$2.8 \cdot 10^{-6}$	$6.5 \cdot 10^{-6}$	$1.3 \cdot 10^{-5}$	$2.1 \cdot 10^{-5}$
12.5	$3.2 \cdot 10^{-7}$	$1.7 \cdot 10^{-6}$	$3.4 \cdot 10^{-6}$	$8.7 \cdot 10^{-6}$	$1.7 \cdot 10^{-5}$	$2.8 \cdot 10^{-5}$
15	$4.0 \cdot 10^{-7}$	$1.9 \cdot 10^{-6}$	$4.1 \cdot 10^{-6}$	$1.2 \cdot 10^{-5}$	$2.2 \cdot 10^{-5}$	$3.6 \cdot 10^{-5}$
17.5	$4.6 \cdot 10^{-7}$	$2.4 \cdot 10^{-6}$	$5.1 \cdot 10^{-6}$	$1.4 \cdot 10^{-5}$	$2.7 \cdot 10^{-5}$	$4.4 \cdot 10^{-5}$
20	$5.4 \cdot 10^{-7}$	$2.7 \cdot 10^{-6}$	$5.8 \cdot 10^{-6}$	$1.7 \cdot 10^{-5}$	$3.4 \cdot 10^{-5}$	$5.6 \cdot 10^{-5}$

Below this temperature, E_a reaches a value of ~ 470 kJ/mol (according to Ref. [26]) lattice diffusion takes place since (E_a/RT_m) = 35.8, whereas above 925 °C, E_a decreases to ~ 275 kJ/mol and ((E_a/RT_m) yields a value of 20.9 [26], suggesting grain boundary diffusion). The stress exponent for SCF at T = 925 °C increased from 1 to about 1.4 during an increase in stress from 10 to 20 MPa (for specimens with d = 6.8 µm), indicating that creep is governed mainly by diffusion. Majkic et al. [101] also stated that grain boundary diffusion takes place in the high temperature range, whereas bulk diffusion occurs below 925 °C, which is in accordance with the (E_a/RT_m) scheme presented by Huang [26].

Microstructural observations reported in Ref. [101] reveal that grains maintain equiaxial shape even after 70 % of deformation. The increase of grain size was also negligible. This might suggest deformation by GBS. However, grain boundary widening was not observed.

Lein et al. [103] performed creep experiments on the SCF modifications $La_{0.5}Sr_{0.5}CoO_{3-\delta}$ (LSC) and $La_{0.5}Sr_{0.5}Fe_{0.5}Co_{0.5}O_{3-\delta}$ (LSFC). The tests were performed in air as well as in

N_2 at stresses from 5 to 28 MPa. The results of these experiments are given in Table 8 (selected data are presented in Figure 23).

Creep parameters for LSFC were estimated to be: E_a = 398 kJ/mole, n = 1.7 and m = - 0.23. For LSC, the activation energy was about 55 % higher (619 kJ/mol) and the stress exponent was 27 % smaller (1.24) than values determined for LSCF. Additionally, the influence of oxygen partial pressure on the creep rate for LSC was a factor two larger (m = - 0.46) than for LSFC, which suggests that LSC is less stable than LSFC as a result of the higher oxygen release under vacuum and the associated creation of a larger amount of cation diffusion paths. However this should lead to a lower activation energy (due to easier diffusion) which is not the case. For both materials the stress exponent varied with temperature. For LSC, a temperature increase from 900 to 1000 °C resulted in a change of n from 1.3 to 2.4. In case of LSCF, the stress exponent changed from 0.5 to 2 when temperature was increased from 950 to 1050 °C. The values were extracted from plots given in Ref. [103].

Table 8. Strain rates (s^{-1}) obtained during creep tests on the LSC and the LSFC specimens [103].

Stress [MPa]	LSC			LSFC		
	Strain rates [s^{-1}] at the temperature of:					
	900 °C	1000 °C	1000 °C	900 °C	950 °C	1050 °C
5	$7.8\cdot10^{-10}$	$2.7\cdot10^{-9}$	$1.9\cdot10^{-8}$	$1.3\cdot10^{-9}$	$2.9\cdot10^{-9}$	$5.7\cdot10^{-8}$
10	$1.1\cdot10^{-9}$	$1.0\cdot10^{-8}$	$7.9\cdot10^{-8}$	$3.9\cdot10^{-9}$	$2.5\cdot10^{-8}$	$3.5\cdot10^{-7}$
15	$1.4\cdot10^{-9}$	$1.7\cdot10^{-8}$	$1.8\cdot10^{-7}$	$3.9\cdot10^{-9}$	$7.6\cdot10^{-8}$	$6.4\cdot10^{-7}$
20	$1.6\cdot10^{-9}$	$2.1\cdot10^{-8}$	$2.8\cdot10^{-7}$	$8.0\cdot10^{-9}$	$1.6\cdot10^{-7}$	-
25	$1.7\cdot10^{-9}$	$3.2\cdot10^{-8}$	$4.0\cdot10^{-7}$	$9.0\cdot10^{-9}$	$2.5\cdot10^{-7}$	-
28	$1.9\cdot10^{-9}$	-	-	$1.6\cdot10^{-8}$	-	-
	d = 10.3 µm		d = 1.7 µm	d = 1.1 µm		

Recent results on LSCF creep behavior, reported by Huang et al. [104] are presented in Figure 22. The authors [104] claim that stress exponent (n) found in the temperature range of 750 - 950 °C has a value in the range of 1.9 to 2.5. This appears to suggest contribution of diffusional- as well as dislocation creep and indicates no transition in creep mechanism. Therefore, a change in E_a from ~ 250 kJ/mol (T < 850 °C) to ~ 490 kJ/mol (T > 850 °C), was related to the creation of new vacancies, which aided creep deformation. However, on LSCF's oxygen non-stoichiometry vs. temperature plot, presented by the authors [104], there is no change in slope at around 850 °C, which could suggest that a higher amount of vacancies is created above 850 °C. Note that below 850 °C, different behavior in air (where creep seems to be affected by phase transition), and in pO_2 = 4 mbar was found. The normalized activation energy (E_a/RT_m) of ~ 37 (according to Huang [26]) suggests lattice diffusion. However, in Ref. [104] the authors suggest that since the morphology of grains (grain size, aspect ratio) stay unchanged after creep test, more than one mechanism contributes to the creep deformation.

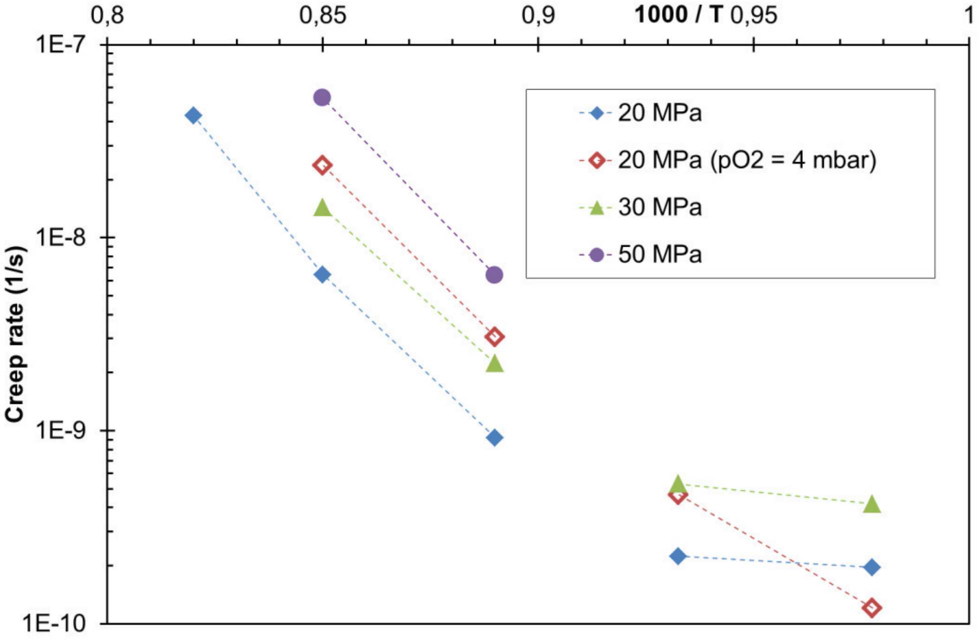

Figure 22. Creep results performed on LSCF by Huang et al. [104].

A comparison of the literature data [99, 101, 103] on creep of different perovskite materials described above is given in Figure 23. The BSCF and SCF materials in this plot had grain sizes of about 6.8 µm. The SCF shows about one order of magnitude higher creep rate than BSCF. For SCF, a change of the creep rate slope vs.

temperature, related to a change of creep mechanism is visible [101]. A similar “step” in the BSCF curve resulting from the dissolution of hexagonal phase is visible [99]. However as mentioned above, the change in activation energy is insignificant. From this comparison, it is concluded that partial substitution of Sr $^{2+}$ with Ba $^{2+}$ ions results in decreasing creep rates.

Despite the about three to six times smaller grain size of the LSC and LSFC materials investigated by Lein et al. [103], they show significantly lower creep rates than BSCF and SCF. After the creep tests the grain size of LS(F)C increased by about 30 %, but no change in the aspect ratio of the grains was found. This might suggest grain boundary sliding. However, no microstructural evidence like grain boundary widening was found. Diffusion of Sr/La cations was suggested by the authors as creep–rate controlling process.

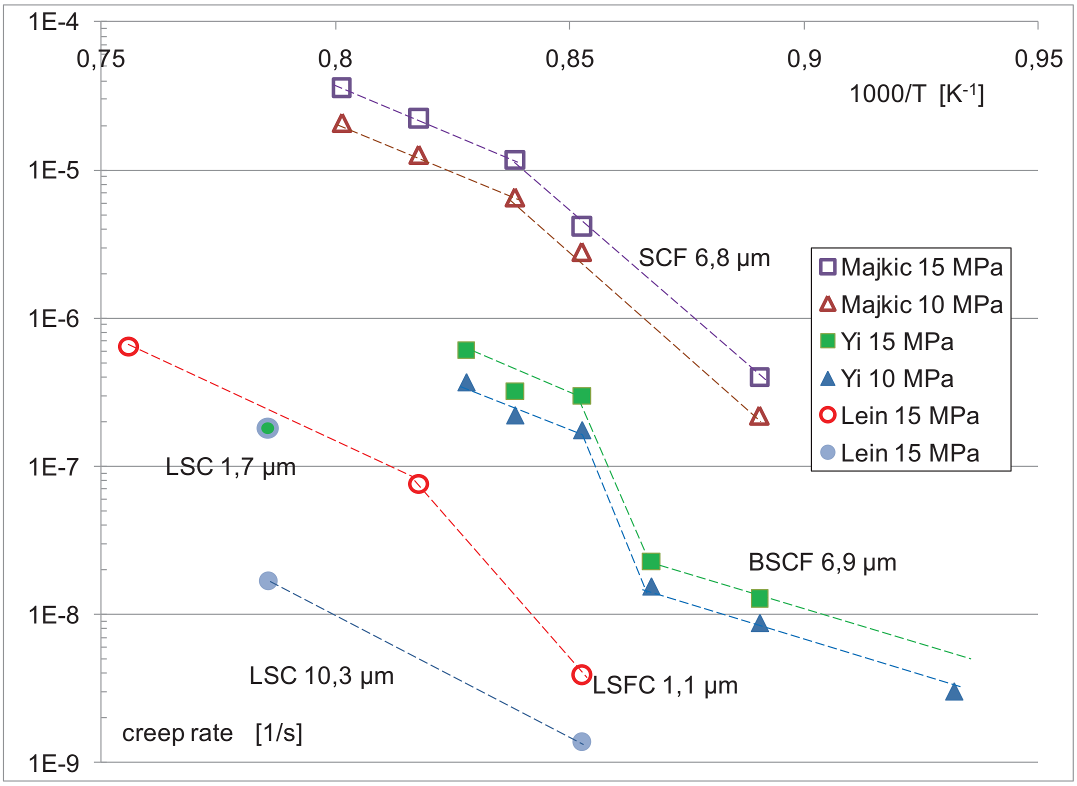

Figure 23. Creep rates of SCF (Majkic et al. [101]), BSCF (Yi et al. [99]), LSC and LSFC (Lein et al. [103]).

Another perovskite material - $La_{0.2}Sr_{0.8}Fe_{0.8}Cr_{0.2}O_{3-d}$ was investigated by Majkic et al. [100]. These experiments, performed under stresses of 10 to 80 MPa at temperatures around 1150 °C (pressure range from 10^{-1} to 10^{-7} atm), yielded an average activation energy for creep of about 500 kJ/mol, whereas for oxygen partial pressures below 10^{-7} atm, the activation energy increases to about 930 kJ/mol.

The creep rates for $La_{0.2}Sr_{0.8}Fe_{0.8}Cr_{0.2}O_{3-\delta}$, reported by Majkic et al. [100] (for a stress of 10 MPa and a grain size of 3.2 μm) are summarized in Figure 24.

Interestingly, the effect of a decrease of the oxygen partial pressure on the creep rate is rather small. This is reflected by an oxygen partial pressure exponent m equal to 0.04. However, for low pO_2 (below 10^{-8} atm) the oxygen influence becomes significant (*m* increases for about one order of magnitude to -0.5) but, opposed to the high pO_2 regime, a decrease of oxygen partial pressure results in increasing creep rate.

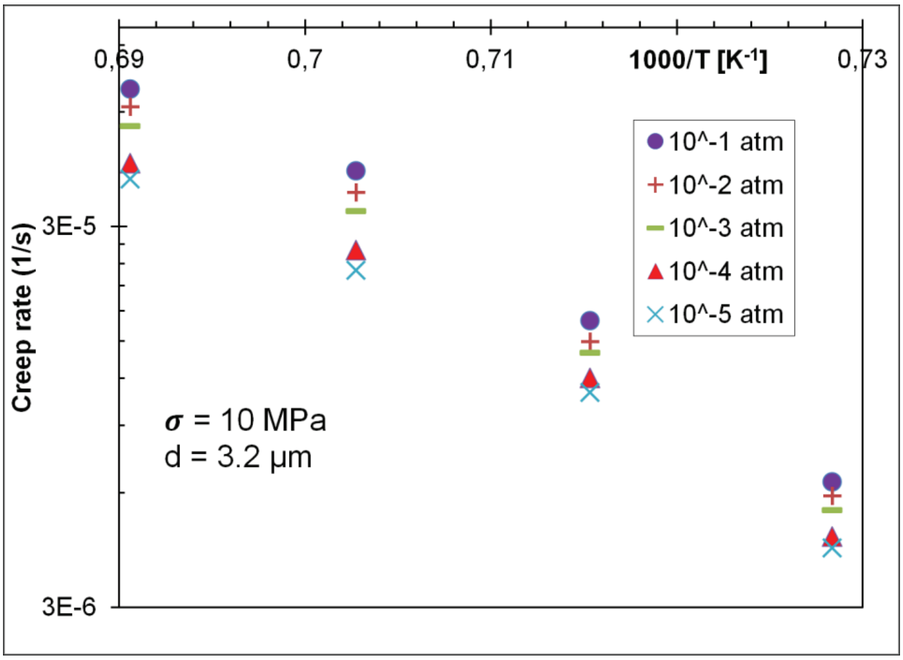

Figure 24. Creep test results of $La_{0.2}Sr_{0.8}Fe_{0.8}Cr_{0.2}O_{3-\delta}$ [100]. PO_2 was varied from 10^{-1} to 10^{-5} atm.

Wolfenstine et al. [105] performed creep investigations on $La_{0.8}Sr_{0.2}Ga_{0.85}Mg_{0.15}O_{2.825}$ (LSGM-2015) in the stress range 5 to 20 MPa. The temperature was varied from 1200 to 1300 °C. The grain size of the material was about 8 µm. The activation energy was determined to 520 kJ/mol. A stress exponent close to unity indicates diffusion creep, while the grain size exponent of 1.7 indicates lattice diffusion, which is expected for such high temperatures. However, no change in grain size as well as in grain aspect ratio was observed, which suggest creep deformation via GBS, accommodated by the lattice diffusion. Results of these tests are given in Figure 25.

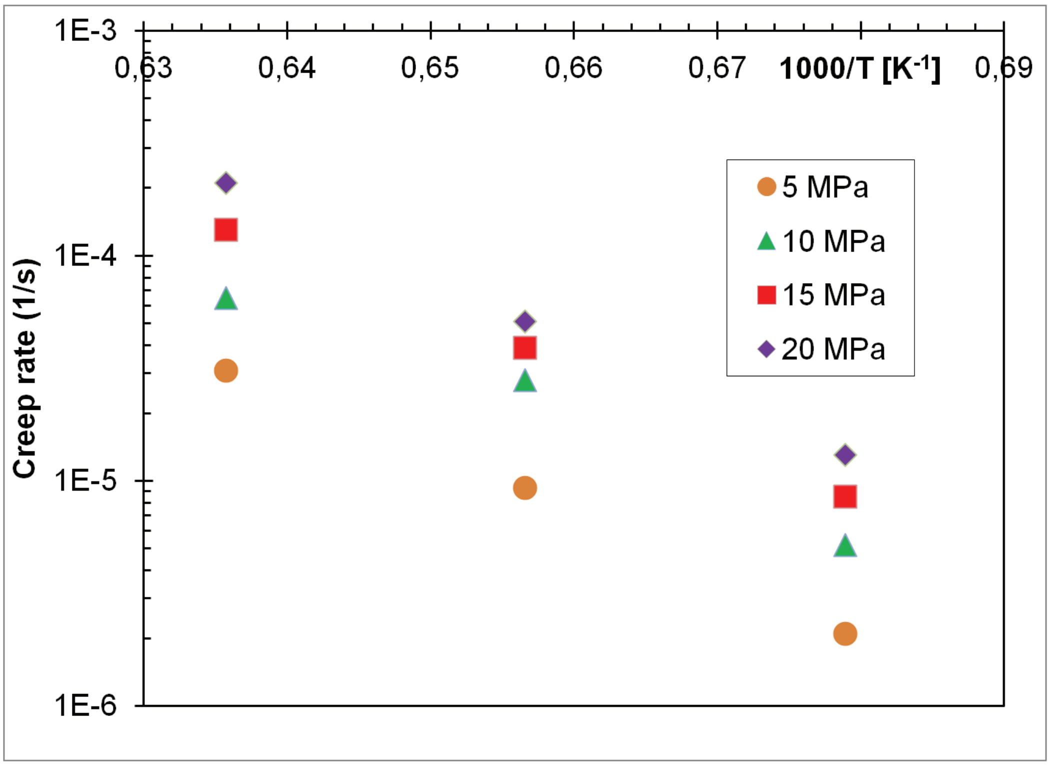

Figure 25. Results of creep experiments performed on LSGM-2015 [105].

2. **Experimental details**

In order to obtain comprehensive information concerning microstructural stability and thermo-mechanical behavior of tubular BSCF perovskite oxygen transport membranes, various mechanical tests, supported by heat treatments and microstructural investigations were performed. In particular, depth sensitive indentation (by Fischer micro-indenter) was used to determine Young's modulus and micro-hardness at room temperature for both, as-received and thermally-treated state. Fracture toughness was evaluated from measurements of the length of indentation cracks.

Micro- and macro-mechanical properties do not have to be identical. While the local measurement using indentation can reveal details on the effect of grain structure and local inhomogenities (grain boundaries, precipitates, demixing and segregation effects), the global measurement using bending tests can yield a Young's modulus that is representative of the macroscopic behavior of the material including the integral effect of all pores and can hence serve as a basis to simulate the global behavior in a membrane system. Furthermore, bending tests are widely used to characterize the fracture strength of ceramics materials, a parameter critical to assess the reliability of the final component. Hence, the Young's modulus and in addition the fracture strength was determined also from bending tests performed in O-ring geometry under various oxygen partial pressures.

The creep behavior of tubular BSCF specimens with 30 mm length and 15 mm outer diameter was investigated by compression tests, carried out both in air and under vacuum. C-ring bending creep tests were performed in order to investigate damage zone at tension loaded side. An additional set of corresponding heat treatments with subsequent microstructure analysis enabled the investigation of the influence of the thermal history on the phase transformation and, in particular, any relationship to creep behavior.

2.1. Investigated material

The $Ba_{0.5}Sr_{0.5}Co_{0.8}Fe_{0.2}O_{3-\delta}$ material was provided by Fraunhofer-Institut für Keramische Technologien und Systeme (IKTS), Institutsteil Hermsdorf (formerly Hermsdorfer Institut für Technische Keramik e.V., HITK), Germany, and prepared by a mixed oxide route from a stoichiometric mixture of the following components: $BaCO_3$, $SrCO_3$, Fe_2O_3 and Co_3O_4, which were milled together and (in case of tubes) extruded at constant speed with addition of water and paraffin / cellulose. Subsequently, the material was dried without degassing and sintered in electric furnaces in air at 1130 °C for 2 h. The heating and cooling rate were 2 K/min. The tubes of 15 mm outer diameter and 1 mm wall thickness were cut by IKTS into shorter sections of 30 mm length (for creep tests) or 10 and 5 mm in length (for O-ring bending tests). In case of discs, before sintering, the powder was pressed into 16 mm diameter pellets with a thickness of 1 or 2 mm.

Moreover, in order to compare creep properties (section 3.5.2) of the above described material with literature values [23, 99], additional BSCF specimens with cylindrical geometry were tested. One batch (l = 11 mm, Ø = 6 mm, d = 4.6 µm) was prepared by VITO - Flemish Institute for Technological Research NV (Belgium), whereas a second batch (l = 11 mm, Ø = 6 mm, d = 6.9 µm) was supplied by the University of Twente (Netherlands).

An additional set of fracture and creep tests was carried out on the newly developed MIEC material $BaCo_{0.4}Fe_{0.4}Zr_{0.2}O_{3-\delta}$ (BCFZ 1442), supplied by IKTS in O-ring geometry ($Ø_O$ =10 mm, $Ø_I$ = 8 mm, b = 10 mm).

2.2. Microstructure investigation

2.2.1. X-ray diffractometry

The phase composition was determined by X-ray diffraction using a D5000 diffractometer supplied by Siemens, equipped with an X-ray tube with copper anode (λ = 1.5418 Å), powered with an accelerating voltage of 40 kV and a current of 40 mA.

2.2.2. **Microscopy**

Microstructure investigations were performed by light microscopy (LM: Axiomat of Zeiss) and scanning electron microscopy (SEM: LEO 440 of Zeiss) on polished ceramographically prepared cross-sections. Specimens were embedded in epoxy resin and ground on silicon carbide abrasive papers with stepwise decreasing size of abrasive particles (gradation from 400 up to 4000 grit). For subsequent polishing diamond pastes and suspensions with grain sizes from 3, through 1 to ¼ µm were used. Using silica suspension for the final polishing step was avoided due to its negative influence on the specimens' surface, since polishing BSCF specimens with SiO_2 suspension results in apparent slight "etching", reducing the LM image quality. When visibility of the grain structure was required, the epoxy resin was removed and the polished ceramographic sections were thermally etched (900 °C for 20 min in air).

Image analysis (grain size, porosity and phase content estimation) was performed with "AnalySIS" software, provided by Olympus. Grain size analysis was performed on thermally-etched specimens, since thermal-etching did not appear to influence the BSCF grain structure, although a local influence on the phase composition could not be ruled out. The latter, however, is not critical for the quantitative grain structure analysis. For the grain size determination the planimetric method was applied involving automated measurement of the grain area performed by the AnalySIS software. The results were then recalculated into the diameter of a circle having an identical area as the measured grain and are given in the following as an equivalent circular diameter (ECD).

Pore size analysis was also, like in case of grain size analysis, performed using the planimetric method. The total pore area was measured on microstructure images and divided by the whole investigated area. This operation gives the volume percentage of pores in the material. The same technique was used to determine the volume content of the secondary-phase after various thermal treatments.

Fractographic analysis was performed on the specimens fractured during bending tests. Fracture origins were identified with the aid of the stereo-zoom microscope (Olympus SZH10) and SEM (LEO 440) as well as laser scanning microscope (Keyence VK 9700).

Transmission electron microscope investigations, (TEM: Philips CM 200 and JEOL 200CX) were conducted on thin foils prepared using focused ion beam technique (FIB: Neon 40EsB CrossBeam of Zeiss).

2.3. Bending experiments

Bending experiments were carried out on an electromechanical test machine (Instron 1362). Two specimen geometries were investigated: 16 mm diameter discs with two different thickness (1 and 2 mm), used for ring-on-ring test (Figure 26a), as well as segments cut from tubes with two lengths (~ 5 and ~ 10 mm) for O-ring tests (Figure 26b). Additional measurements on BCFZ 1442 O-rings ($Ø_O$ =10 mm, $Ø_I$ = 8 mm, *b* = 10 mm) were performed.

During testing, tension and compression stresses are present on the inner and the outer surface of the O-ring specimens, respectively, depending on the axial and radial position of the specimen. If a contact point of specimen and the upper pushing rod will be taken as a reference point (Figure 26b) on the sample cross-section (α = 0°), the highest tensile stresses at the inner surfaces are localized at the sample-traverse contact points indicated by the vertical axis (α = 0° and α = 180°). The highest tensile stresses at the outer specimen surface are present at the positions for which α = 90 and 270°, respectively. Although in this case, fracture origins might be present close to the inner surface (for α = 0°, 180°), as well as near the outer surface (for α = 90°, 270°), where local maxima of tensile stresses are present, the highest stress for the current specimen geometry will arise at the outer surface in the positions 90 and 270°.

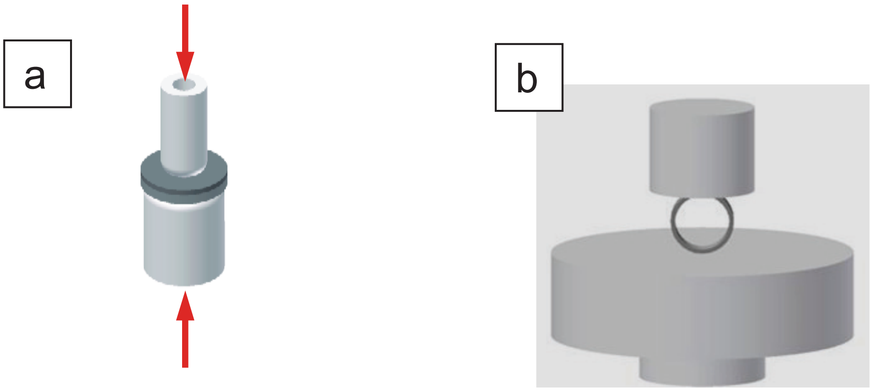

Figure 26. Sketch of set-up used for bending tests: a) ring-on-ring, b) O-ring.

2.3.1. **Fracture stress**

Initial fracture stress measurements were performed in ring-on-ring geometry at RT following the procedure outlined in the standard ASTM C1499-05 [106] for thick 2 mm thick discs. A loading rate of 100 N/min was chosen in order to avoid slow crack grow effects [107]. The fracture stress was calculated from Equation 8:

$$\sigma = \frac{3P}{2\pi \cdot k^2} \quad 1 + \nu \ ln \ \frac{R_2}{R_1} + \frac{1-\nu}{2} \ \frac{R_2^2 - R_1^2}{R_3^2}$$

Equation 8.

where: P - applied force, k – specimen thickness, ν - Poisson's ratio, R_1,R_2 - radii of loading and supporting ring, respectively, and R_3 - specimen radius

In subsequent tests, 1 mm thick discs from another batch were tested in order to check the effect of the specimen thickness on the material properties.

In addition to RT also the temperature dependency of the fracture stress was determined from O-ring tests, performed at temperatures ranging from 25 °C (RT) up to 850 °C. Since the tubular material was prepared via an extrusion process, whereas the plates were cold pressed and sintered it could not be assumed a priori that they have identical properties. At least 3 specimens were tested for every temperature, which allows to limit the effect of experimental uncertainties. One set of tests was also performed under reduced oxygen partial pressure (10^{-2} mbar). The fracture test conditions followed the procedures recommended by Bongartz [108]. Again a loading rate of 100 N/min was used. The data were evaluated using equations for linear bending theory. Accordingly, the fracture stress (Equation 9) was derived for the positions of maximum tensile stress at the outer side of the specimens (90° and 270°) from [108]:

$$\sigma = M\frac{k\ \ 2-e}{bke\ \ r-k\ \ 2}, \qquad M = \frac{F_B\ \ r-e}{\pi}, \qquad e = r-k\ \ \ ln\frac{r+k\ \ 2}{r-k\ \ 2}\ ^{-1}$$

Equation 9.

where: k - wall thickness, b - width, r - average radius, and F_B – maximal applied force.

The quality of ceramic components can be assessed by evaluating the Weibull distribution of failure probability:

$$P_s\ \ V_0\ \ = exp\ \ -\ \ \frac{\sigma}{\sigma_0}\ ^{u}$$

Equation 10.

where: P_S – survival probability, V_0 – characteristic volume of tested specimen; σ – applied tensile stress, σ_0 - the tensile stress which cause failure of 63 % of tested specimens and u – Weibull modulus.

The Weibull modulus was determined from the RT data (from at least 8 specimens), following the procedure outlined in the standard ISO 20501 [109]. All results obtained during fracture tests can be further evaluated using Equation 10. Note that σ_0 also depends on the sample geometry.

In addition the Weibull modulus (u*)* gives valuable information on the survival probability of materials. It can be determined from a graphical representation of strength data [109].

The slope of ln[ln[1/(1-P_f)]] vs ln(σ) plot is u. In this case, σ_i is the individual fracture stress of the sequentially ordered values, and (P_f) refers to probability of failure, defined by following formula:

$$P_f \;\; \sigma_i \;\; = \frac{i - 0{,}5}{N}$$

Equation 11.

where: i - order number, N – number of tested specimens.

To investigate the influence of phase stability on the fracture stress, an additional set of bending experiments was performed (chapter 3.4.1) on the specimens annealed in different conditions (chapter 2.5).

2.3.2. **Young's modulus**

Another mechanical property determined from the bending tests is the Young's modulus (E) of the material. It can be calculated from the load displacement data obtained in bending tests. For O-ring tests, the following formula is used for calculation of E [108]:

$$E = \frac{P_B r^2}{d_B bke} \;\; \frac{\pi}{4} - \frac{2}{\pi} \;\; 1 - \frac{e^2}{r^2} \;\; + 2\frac{e}{r} \;\; \frac{2}{\pi} \;\; 1 - \frac{e}{r} \;\; - \frac{\pi}{8} \;\; + 1.9 \;\; 1 + \nu \;\; \frac{e}{r} \;\; ; \quad e = r - k \;\; ln\frac{r+\frac{k}{2}}{r-\frac{k}{2}} \;\; ^{-1}$$

Equation 12.

where: P_B – fracture load, r - average radius, k - wall thickness, b - specimens' width and d_B- specimen's deflection

In case of ring-on-ring tests the following formula was applied to determine Young's modulus [110] :

$$E = \frac{3 \;\; 1 - \nu^2 \;\; \cdot R_1^2 \cdot \Delta P}{2\pi \cdot \Delta d_e \cdot k^3} \cdot \;\; \frac{R_2}{R_1} \;\; ^2 - 1 - 2ln \;\; \frac{R_2}{R_1} \;\; + \frac{1}{2} \;\; \frac{1 - \nu}{1 + \nu} \;\; \cdot \;\; \frac{R_2^2 - R_1^2}{R_3^2} \qquad \frac{R_2^2 - R_1^2}{R_1^2}$$

Equation 13.

where: d_e - central deflection of specimen (for other parameters description see Equation 8)

It should be noted that at temperatures higher than 500 °C, measurement can be influenced by creep and chemical expansion effects due to oxygen release (chapter 3.5.1).

2.4. Depth sensitive indentation

Indentation testing is based on loading a sharp tip made of diamond or other hard material and pressing it into the surface of a material to be tested. Five main tip types are most commonly used: Vickers, Berkovich, cone, cube-corner and sphere. For the indentation investigation performed in the frame of present work, the most common Vickers tip was used. A Vickers indenter geometry corresponds to a square pyramid with an angle of 136° between triangle faces (Figure 27) [111].

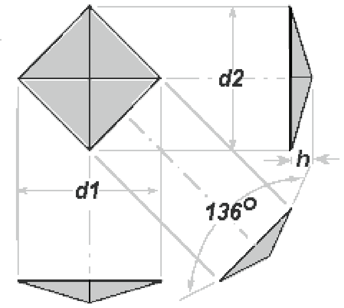

Figure 27. Geometry of a Vickers indenter tip [111].

In the case of depth-sensitive indentation measurement the force applied to the indenter tip and the indenter penetration depth are continuously recorded during loading and unloading. A typical load – displacement curve obtained during depth-sensitive indentation of the BSCF in the present work is shown in Figure 28.

The slope (S) of the linear part of the unloading load-displacement curve (Figure 28b) allows the calculation of Young's modulus (E_{IT}). Note that E of indenter tip is not infinite. Combined Young's modulus (E_r), according to the Hertz equation [112], can be written as:

$$\frac{1}{E_r} = \frac{1-\nu_i^2}{E_i} + \frac{1-\nu_s^2}{E_{IT}} \rightarrow E_{IT} = \frac{1-\nu_S{}^2}{\frac{1}{E_r} - \frac{1-\nu_i^2}{E_i}}\ ; \quad E_r = \beta \frac{\sqrt{\pi}}{2} \frac{S}{\sqrt{A_c}}$$

Equation 14.

where: E_{IT} – indentation Young's modulus; E_i – Young's modulus of indenter, ν_s and ν_i – Poisson's ratio of specimen and indenter tip, respectively; β – correction factor for Vickers indenter (1.0124); S = dP/dh, P – applied load; h - indentation depth; A_c – projected contact area.

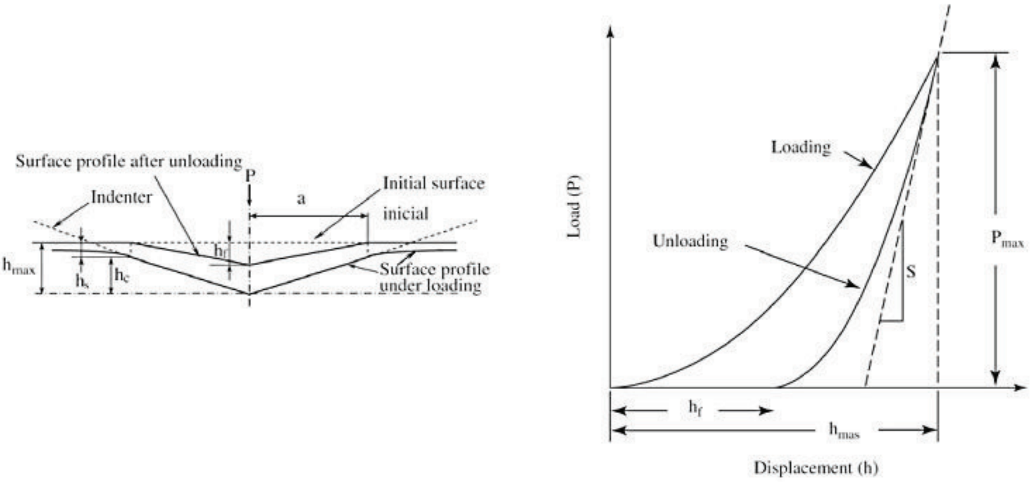

Figure 28. Indentation results [112], a) main parameters describing the impression, b) schematic representation of load - displacement curve obtained during indentation.

For determination of Young's modulus (E_{IT}) and microhardnes (H_{IT}), the projected contact area (A_c) of the indentation imprint (Figure 29) needs to be known. A_c, as a function of contact depth (h_c), is calculated from the unloading slope (Figure 28b) and may be represented by Equation 15:

$$A_c = 24.5h_c^2$$

Equation 15.

where: A_c - projected contact area; h_c - contact depth.
Additional terms are normally added to calibrate the indenter shape.

Micro-hardness can be calculated according to the Equation 16 [113].

$$H_{IT} = \frac{P_{max}}{A_c}$$

Equation 16.

where: H_{IT} – indentation microhardness; P_{max} – peak load

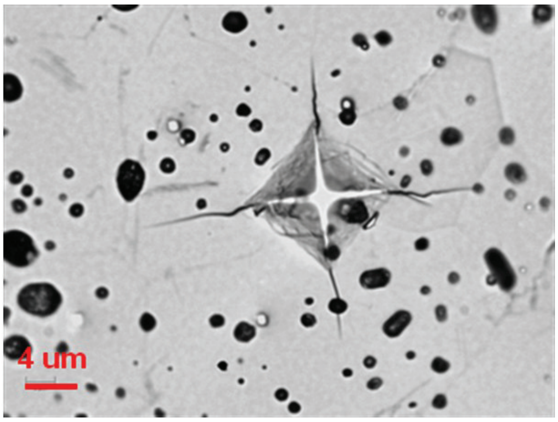

Figure 29. Typical Vickers impression in BSCF. Cracks, propagating from the corners are visible on the diagonals' extension.

The fracture toughness of the material can be determined from the length of cracks induced by the indentation (Figure 29). Depending on the indentation crack geometry, a multitude of equations relating the size of the indentation crack with the fracture toughness is reported in the literature [114]. In the current work, for the typical Palmqvist propagation of indentation cracks observed in the investigated BSCF material, the equation proposed by Niihara [115] (Equation 17) was applied for indentation toughness determination based on impressions carried out with a load of 1 N:

$$K_{ind} = 0.018 \; \frac{E}{H_{IT}}^{0.4} \; H_{IT} a^{0.5} \; \frac{l}{a}^{-0.5}$$

Equation 17.

where: E – Young's modulus, H_{IT} – indentation hardness, a – half of imprint's diagonal length, l – crack length (measured from the end of imprint).

Note the most frequently used Anstis equation [115] could not be used due to too small crack to diagonal length ratio ($c/a \approx 2.2$ is lower than the limit for the validity of equation of 2.5).

2.5. Additional heat treatment

To gain information on the temperature dependence of the phase stability and phase transition kinetics at operating conditions, and in order to correlate mechanical properties (like creep resistance) with potential microstructural changes, the following set of heat treatments was performed:

Five BSCF specimens in as-received state were annealed in a box furnace (type LT9/13, supplied by Nabertherm) in air for 336 h at temperatures from 750 to 950 °C with 50 °C steps. These experiments, followed by microstructural investigations of the annealed material, provided vast qualitative and quantitative information about stability of BSCF at elevated temperatures.

A further set of annealing tests aimed to characterize the kinetics of the phase transitions occurring in the BSCF: A specimen, which was previously annealed at 800 °C for 336 h, was divided into smaller parts and three of them were heat treated according to the scheme given in Figure 30.

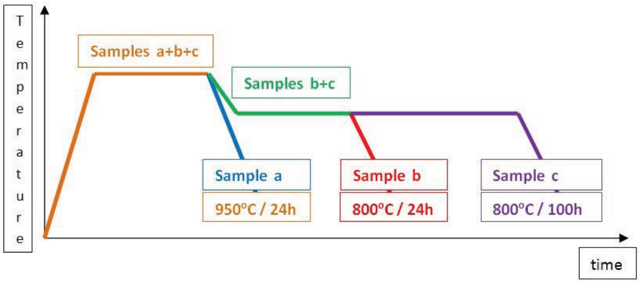

Figure 30. Temperature sequence of the heat treatment, used to characterize phase transformation kinetics.

The three specimens were first placed into the furnace and heated up to 950 °C with a subsequent dwell time of 24 h, corresponding to the duration of a single-temperature creep test (see section 2.6.1). Afterwards, one specimen was taken out of the furnace and its microstructure was investigated in order to clarify whether annealing affected potential secondary phases, which might have formed during previous annealing at 800°C (section 3.2.1). The remaining specimens were cooled down to 800 °C within the furnace at a cooling rate of 8 K/min and the annealing was continued at this temperature. After 24 h the second specimen was taken out, in order to investigate microstructure at this point of heat treatment. The third specimen was removed from the furnace after 100 h of annealing at 800 °C.

To gain complete overview of the BSCF stability within a wide range of possible operating conditions, an additional set of annealing experiments was performed in vacuum (pO_2 of 10^{-5} and 4 mbar) for 100 h at temperatures of 950, 750, 700 and 600 °C (section 3.2.2). Before annealing, all specimens were thermally equilibrated at 950 °C for 24h.

An additional annealing treatment was performed reproducing the thermal history during creep testing shown in Figure 33 to investigate the microstructural changes induced by the thermal treatment applied in a creep test, however, without considering the influence of deformation on the microstructure (see Figure 53).

To determine the influence of the material's grain size on creep behavior, a set of heat treatments was performed in air at 1150 °C for 2 h and 50h, resulting in substantially different grain size of 88 ± 33 μm and 140 ± 52 μm, respectively. Those specimens, additionally to the basic material with its grains' d = 26 μm, were subsequently subjected to creep tests.

In order to check the influence of hexagonal phase on fracture stress (chapter 3.4.1), a set of 10 mm width O-ring specimens were annealed in air at 750 °C for 150 h in order to create significant amount of hexagonal phase in the microstructure. Additionally, a second set of specimens was annealed in vacuum of 10^{-2} mbar at 950 °C for 24 h to assure a one phase (cubic) structure.

2.6. Creep experiments

2.6.1. Experiment setup and methodology

The majority of the compressive creep tests was performed on tubular BSCF specimens with a length of 30 mm and an outer and inner diameter of 15 and 13 mm, respectively, supplied by the IKTS. Additionally, the BSCF cylinders (described in section 2.1) and a limited number of the BCFZ 1442 specimens were tested.

Before the tests, the flat sides of the specimens were carefully ground and polished to obtain parallel contact surfaces to the specimen fixtures. To assure proper alignment and to avoid superimposed bending loads as far as possible, the specimen fixtures (Alumina plates) were coupled to the load rig by a half sphere as shown in Figure 31.

Compressive creep experiments were performed using two Instron 1362 electromechanical testing machines, equipped with high temperature furnaces, mainly under laboratory-air and high-vacuum (pO_2 10^{-5} mbar). Additionally, a set of tests at intermediate pressure (pO_2 4 mbar) was carried out. Creep tests performed in these various environments enabled the analysis of the oxygen partial pressure influence on deformation processes (section 3.5.2).

A linear variable differential transformer (LVDT, Sangamo, range ±1 mm, precision 1.25 µm), placed in the lower part of the testing machine, was used to measure the traverse displacement. The LVDT was coupled with the bottom of the half-sphere in the clamping device by an alumina rod. Therefore the position change of the lower traverse relative to the upper specimen fixture was measured providing information about sample deformation.

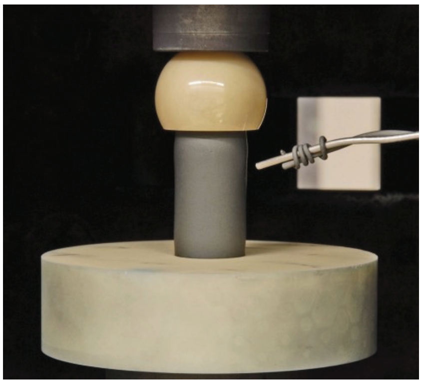

Figure 31. Setup for compressive creep tests. Specimen is mounted between alumina table and half sphere.

All tests were performed in the constant stress mode. The applied force was measured by load cells (Interface Company). In the case of creep tests performed in air, a load cell with 10 kN measuring range (1210 ACK) was applied, while in the load frame used for vacuum tests, a 1.5 kN (1210 BLR) load cell was used. Various stresses (20, 30 and ~ 63 MPa) were applied in order to determine the influence of stress on the creep rate (section 3.5.2).

Tests were conducted within a temperature range from 650 to 950 °C with 50 K increments. Both, increasing- and decreasing- temperature sequences during creep testing were applied. However, after processing the data, test results obtained below 700°C were not further considered due to the high uncertainty of measurements. Every specimen was pre-annealed at 850 °C before creep testing (section 3.5.1). A schematic presentation of the testing procedure with increasing temperature is given in Figure 32: The first test was performed at 650 °C on the sample previously annealed at 850 °C and subsequently cooled down to the test temperature. The stress was applied after an equilibration time of 1 h at 650 °C (Figure 32).

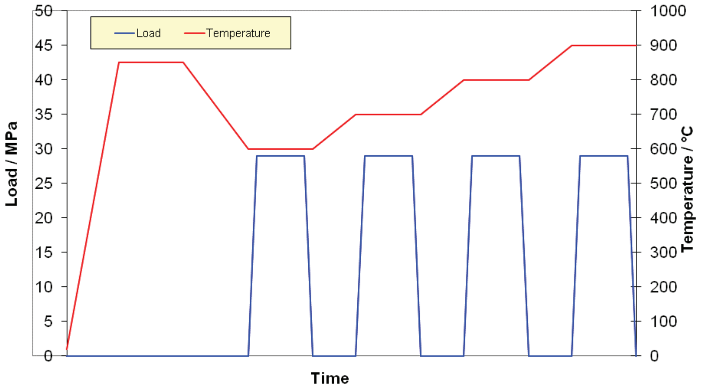

Figure 32. Typical temperature and load history for compressive creep tests.

After at least 24 h of creep and at least 20 h of steady state creep, the specimen was unloaded and temperature was increased to the next value. After a subsequent temperature-equilibration period of 1 h, the creep load was applied again. This procedure was repeated up to 950 °C with 50 K temperature increments. In most cases, the experiment was terminated after creep at 950 °C, although some exceptions were made. For one group of specimens, creep experiment was modified by addition of cooling sequence (Figure 33), which allows to investigate specimens with one phase microstructure, maintained after the test at 950 °C (see annealing results in section 3.2.1), instead of the two-phase microstructure, generated at 750 °C during the heating sequence (see microstructural issues described in chapter 3.2.1).

Data concerning temperature, stress and strain during the tests were collected with a sampling rate of 0.5 Hz. Figure 34 shows an example of an experimental strain – time curve. Two creep regimes, primary and secondary (see Figure 19), can be distinguished.

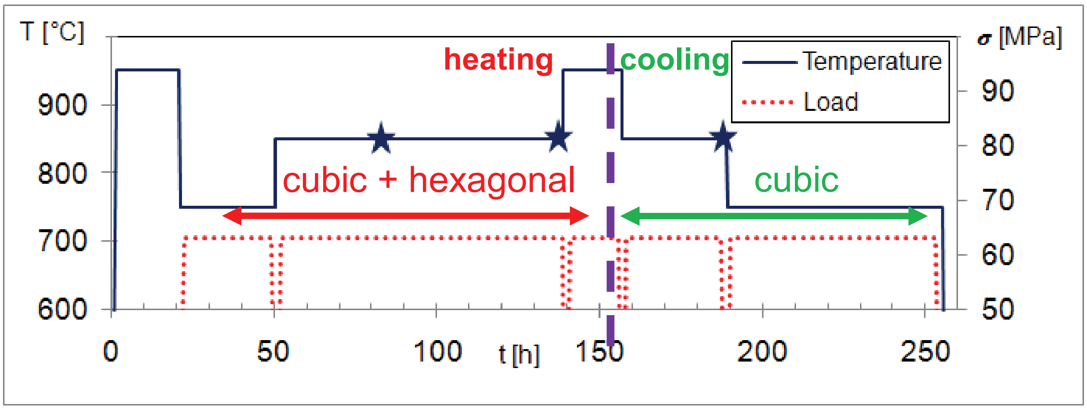

Figure 33. Thermal and load history used while additional compressive creep tests (63 MPa) – both, while heating as well as cooling, allowing to find hysteresis effect.

In order to find a reliable procedure for creep rate evaluation, that minimizes the influence of uncertainties in the transition between primary and secondary stage and nonlinearities as well as data scatter during secondary creep, two different types of fitting routes were considered: linear and 2nd order polynomial.

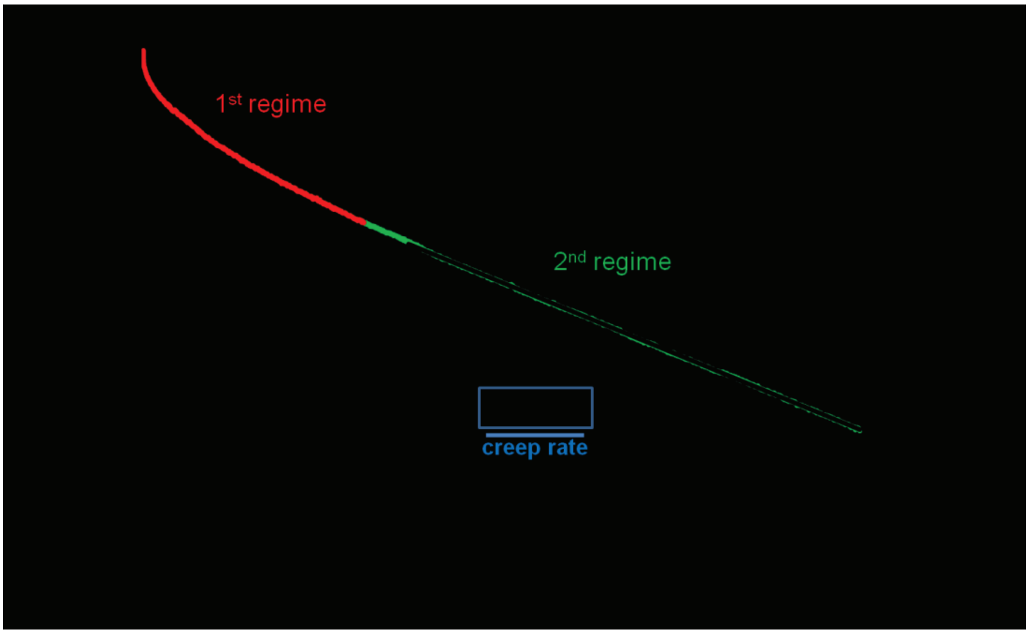

Figure 34: Time – strain curve obtained during creep at 850 °C. The primary regime is marked with red, the secondary with green color. Creep rate value ($9.14{\cdot}10^{-9}$ s^{-1}) is marked with red circle in Figure 93.

In Figure 35, a typical comparison of fitting results, obtained for the curve displayed in Figure 34 is shown. The first points for linear and polynomial fitting are results of fitting the whole curve (including primary creep regime). The abscissa axis gives the time, from which point of the curve shown in Figure 34 fitting starts. For example, for *t* = 60000 s in Figure 35 the part of the curve from *t* = 0 to *t* = 60000 s in Figure 34 is excluded, such that fitting is performed on all data collected after 60000 s. Note that good agreement in values obtained with these two fitting methods is visible for the last part of creep curve (up from 140000 s). The results obtained by linear fitting route are close to this value already after 60000 s. Furthermore, the linear fitting procedure resulted in a higher stability of results (Figure 35) and was therefore applied for evaluation of all creep-rate data in the present study.

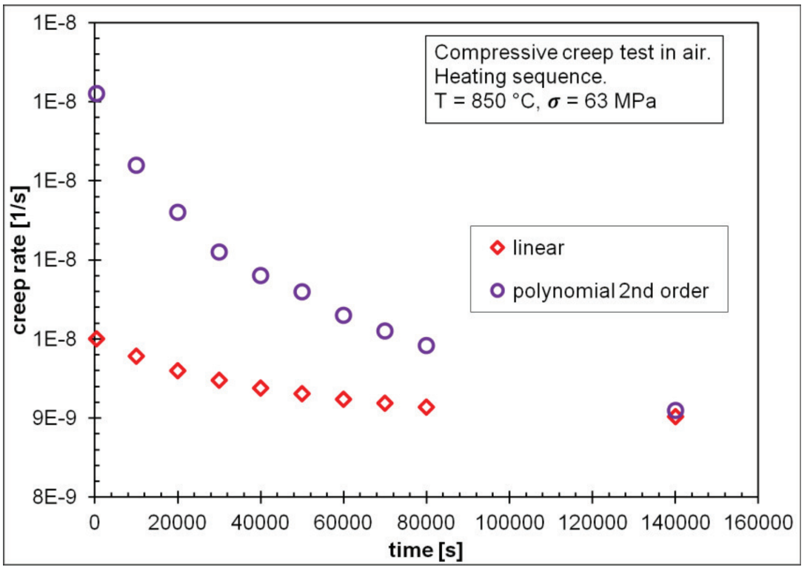

Figure 35. Comparison of linear and 2nd order polynomial fitting of curve displayed in Figure 34.

In case of the compressive creep tests also the Young's modulus, was determined. The value was determined directly from the slope of the linear part of the stress – strain curve obtained during loading the specimen ($E = \Delta\sigma / \Delta\varepsilon$).

Creep damage occurring under tensile load was investigated by dead-load bending creep tests of specimens with C-ring geometry (Figure 36) prepared from 10 mm width

O-ring samples (see chapter 2.1) by machining an additional section along the sample’s longitudinal axis, ensuring free specimen movement during deformation.

A constant load of 6.7 N was applied. The setup (Figure 37) was inserted into a furnace installed on an Instron 1362 electromechanical testing machine (usually used for compressive creep tests in air) and heated up to 900 °C with a heating rate of 8 K/min. The duration of the following holding time was 100 h.

Figure 36. Geometry of C-ring specimen. $Ø_{O}$ = 15 mm, $Ø_{I}$ = 13 mm, t = 10 mm.

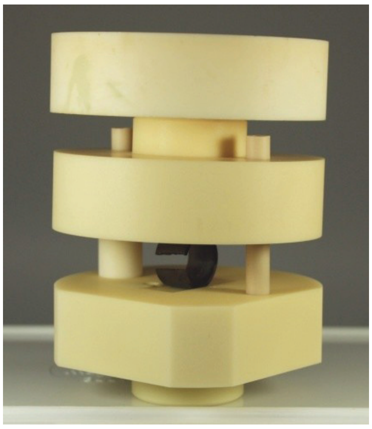

Figure 37. Dead load set-up for bending tests.

One cross-sectional side of each tested C-ring specimen was ground and polished (see procedure in chapter 2.2.2) before the creep experiment in order to enable observation and comparison of the grain structure before and after the test (section 3.2.4).

2.7. Post operational analysis

In order to correlate the results of basic research on microstructure – mechanical properties relationships with the behavior of components under realistic conditions, membrane tubes damaged during operation in a demonstration unit [116] were investigated.

The demonstrator unit was designed by the IKTS, Hermsdorf. It consists of a chamber with hexagonal profile, containing heating elements which provide an operation temperature of about 850 °C. An aluminum holder is placed at the bottom of the unit, which allows mounting 19 tubular ceramic membranes for oxygen separation with a length of 470 mm (Figure 38b). The tubes are closed at their upper end, and their outer surfaces are placed in air at ambient pressure. The extracted oxygen is removed from the inner side of the tubes (via openings localized in the lower tube part fixed to the aluminum holder) by a vacuum pump.

Figure 38. Demonstrator unit built up by the IKTS, Hermsdorf. a) Outer view of the system in operation. b) Array of tubular BSCF membranes mounted in a metal holder inside of demonstration unit [117].

Three tubes, which failed during operation as well as one intact tube were demounted at the IKTS and sent to FZ Jülich for post operational microstructure analyses.

Neither thermal history (stationary operating time as well as the duration of start-up and shut-down sequences) nor the position of the investigated elements in the tube array was known, since the tubes were removed from the system for maintenance reasons without detailed documentation.

The tubes were investigated in a large-chamber SEM at the RWTH Aachen University (Gemeinschaftslabor für Elektronenmikroskopie, GFE). Subsequently, the tubes were sectioned into O-ring samples with 10 mm length. The 40 segments obtained in this way were numerated, according to their position along the tube. Fracture stress and Young's modulus were measured using O-ring tests (section 3.6.1) at room temperature and evaluated for each segment. Selected samples were submitted to post-experimental microstructure characterization (after appropriate ceramographic preparation of their cross sections). The microstructures were compared with the reference microstructures of the BSCF with specified thermal / environmental history (see chapter 2.5 and 3.2.1). From matching microstructures of samples taken from the demonstrator and reference samples, the thermal history of particular segments could be identified. On this basis, the axial temperature profile of a whole tube was estimated (section 3.6.2). In order to verify the correctness of thermal history estimation from microstructure, a comparison with temperature profiles measured in situ for particular tube positions in the demonstrator under operation was performed.

3. Results and discussion

3.1. Microstructure of as-received material

A detailed investigation of the microstructure is a prerequisite for the understanding of the mechanical behavior of a material. This requires in addition to an investigation of the initial, as-received material also a consideration of annealing and operational effects that might degrade the mechanical properties of a material.

In order to analyze the morphology of the BSCF material (grain size, porosity and chemical / phase composition) in the as-received state, a series of microstructural investigations was performed (for details, see chapter 2.2.2).

3.1.1. Microscopy

Initial microstructural investigation of the as-received BSCF tubes was carried out using light microscopy (LM). A typical micrograph of the as-received material is shown in Figure 39.

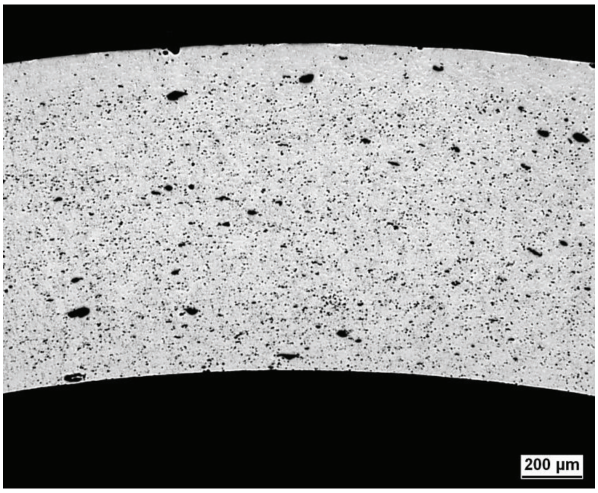

Figure 39. LM micrograph of a tubular BSCF membrane (transversal cross section).

The porosity of the as-received material determined from LM micrographs is 8 ± 3 %.

Since the grain boundaries are not visible on the polished cross-sections of the BSCF specimens, thermal etching was applied in order to reveal details of the grain structure. Polished samples were etched at 900 °C for 20 min. The average grain size of as-received BSCF tubes, determined on thermally-etched material cross-sections can be represented by an average equivalent circular diameter of d = 26 ± 12 µm.

In addition the grain size was determined at the outer surface of the tube resulting in similar value as obtained for the cross-section. The average grain size of the BSCF demonstrator tubes (see section 3.6) was d = 35 ± 12 µm.

With this, the grain size of the material supplied by the IKTS is about 5 times larger than the grain size of BSCF specimens reported in [99] and those which have been produced at FZ Jülich, IEK-1 and investigated in Ref. [26].

For comparison, grain size analysis was also performed for sets of the BSCF specimens in disc geometry, supplied both by the IKTS and the Institute of Energy and Climate Research - 1 (IEK-1) of FZ Jülich, respectively.

The IEK-1 material had a fine grain structure with an average ECD = 6 ± 3 µm (Figure 40), whereas the average ECD of the grains of IKTS discs is about 3.5 times larger (22 µm). This difference originates from different sintering conditions (1000 °C / 12 h for IEK-1 and 1130 °C / 2 h for the IKTS materials).

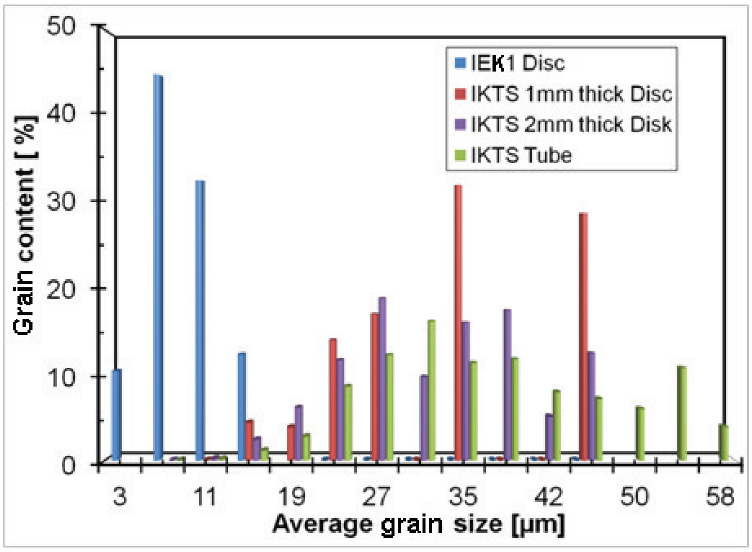

Figure 40. Comparison of the grain size distribution for the BSCF materials produced in various geometries by different suppliers (IKTS and IEK-1).

The microstructure of the BSCF material, supplied by the IKTS, in the as-received condition is also influenced by the very slow cooling rate (2 K/min), which was chosen to avoid thermal stresses resulting in crack formation during fast cooling. Microstructural investigation revealed the presence of a small amount (2 %) of secondary phase nucleating at the grain boundaries, which can be seen as dark grey regions in Figure 41.

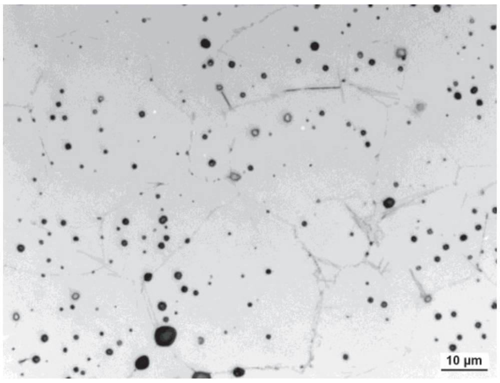

Figure 41. LM micrograph of an un-etched cross-section of an as-received BSCF tube. Traces of hexagonal phase are visible on the grain boundaries. Black spots, also visible on the image, are pores.

LM was supported by SEM investigation, which allowed a determination of the local chemical composition by the EDX analyses. Results of these analyses are given in Table 9 (oxygen was excluded from quantification).

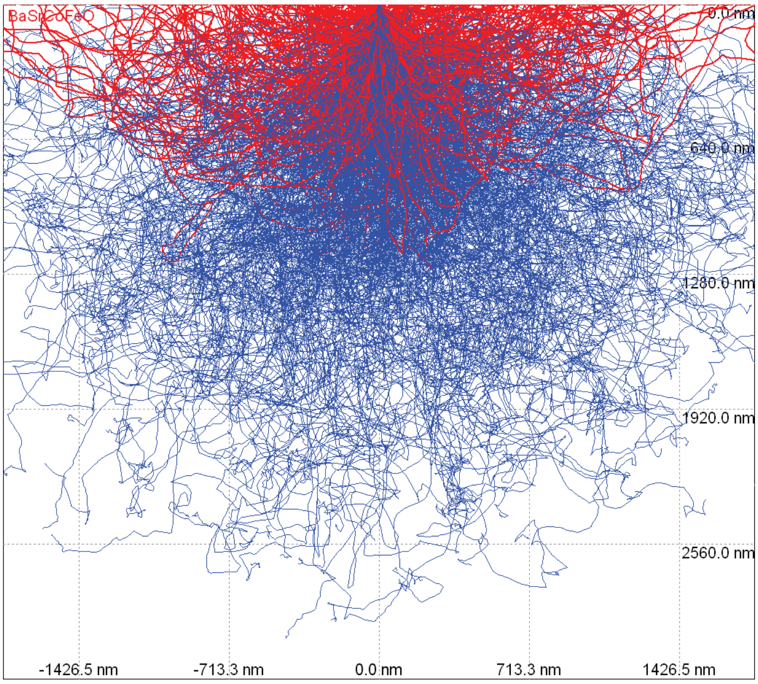

Figure 42. Results of CASINO simulation for SEM-EDX measurements on the BSCF specimen.

Simulation performed with “Monte Carlo Simulation of electron trajectory in solids” (CASINO) V2.4 software, reveal that during EDX analysis of the BSCF specimens with a voltage of 20 kV, the beam penetrates the area of~ 7 μm^2 on the depth of ~ 2.5 μm (see Figure 42). Hence, the SEM is not appropriate to investigate thin precipitates of hexagonal phase that might be expected to be localized only at the grain boundary.

Table 9. Chemical composition of the BSCF tube supplied by the IKTS.

Element:	SrL	BaL	FeK	CoK	Total
wt%	29	38	6	27	100
at%	28	23	9	39	100

The chemical composition obtained from the EDX analysis corresponds very well to the general chemical formula of ABO_3 perovskites. For the IKTS material, minor amounts (0.4 %) of cobalt oxide (Co_3O_4) were found as randomly localized inclusions of a round shape with an average diameter of about 2 μm, probably as a remnant of the manufacturing process. The VITO material exhibits a higher amount of Co_3O_4 (~ 2 %) in comparison to the BSCF provided by the IKTS, whereas the TWENTE material contains 0.3 % of (Co_3O_4). Although microstructural investigations performed on 4 tubes showed a mostly homogenous microstructure, an irregular near-surface inclusion with a length of ~ 200 μm could be noted (Figure 43), which might initiate failure under mechanical loading.

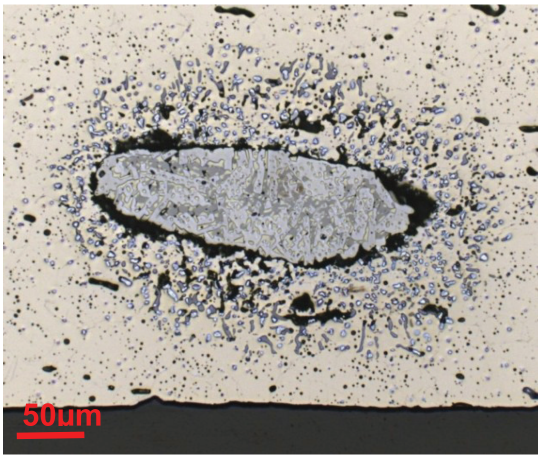

Figure 43. Irregular agglomerate, about 200 μm length, localized close to the surface of the BSCF tube.

3.1.2. **Phase composition.**

Results of XRD analysis, performed in air at RT on as-received BSCF specimens, confirmed the presence of a single-phase material with cubic structure (Figure 44) and a lattice parameter of *a* = 3.978 Å, corresponding to the BSCF perovskite [27, 55].

Small amounts of secondary phases, revealed during initial (chapter 3.1) LM and SEM investigation (as Co_3O_4 inclusions or hexagonal phase at the grain boundaries) could not be detected in the XRD measurements. Most probably, the amount of the secondary phases was below the detection limit of the XRD method, which is about 2 %.
Note that neither Svarcova et al. [56] on their own produced BSCF specimens, sintered in air at 1000 °C for 12 h, nor Niedrig et al. [55], on the BSCF specimens supplied by the IKTS, detected the hexagonal BSCF phase in as-received specimens by the XRD. However, the authors reported the presence of a hexagonal phase in the BSCF after thermal treatment in air at selected temperatures in the range from 700 °C to 850 °C [55, 56]. Note that investigation reported in Ref. [55] were conducted in parallel to stability investigation described in chapter 3.2.1 in frame of MEM-BRAIN project. The existence of a hexagonal phase was investigated in detail by Mueller et al. [118] and Efimov et al. [119].

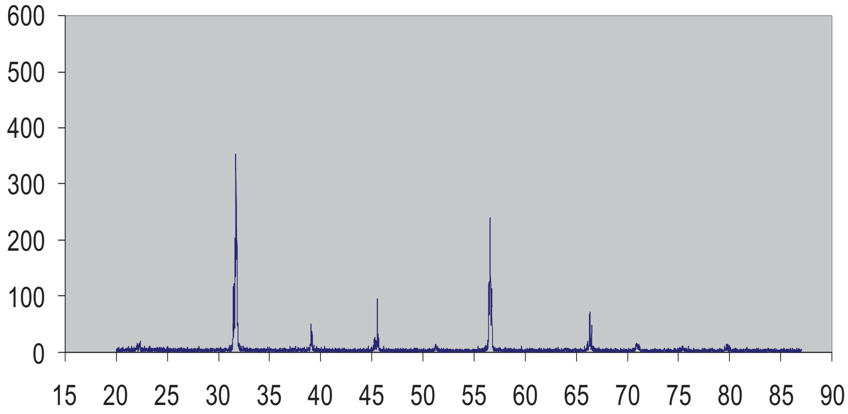

Figure 44. XRD results indicating a single-phase cubic BSCF material.

3.1.3. **Fractography**

In order to gain information on material defects that might initiate fracture under mechanical loading a set of microstructural investigations was performed at fracture surfaces of specimens tested in O-ring geometry (tests described in section 2.3).

Figure 45 shows an O-ring specimen fractured in a bending test at RT. The specimen broke into 4 parts, indicated with numbers from 1 to 4. The corresponding fracture stress (125 MPa) was one of the lowest values obtained during tests performed on 8 as-received BSCF specimens at RT. The strength, determined for a set of 8 BSCF specimens in air at RT, was 143 MPa (see chapter 3.3.2).

Figure 46a shows the probable failure origin found in the fracture surface of specimen piece “1” (side indicated by red arrow on Figure 45). In the upper part of the fracture surface a compression curl is visible. The fracture origin appears to be located at a position loaded in tension at the inner side of the tube. This position is surrounded by a “fracture mirror”, typically indicating the fracture origin [79].

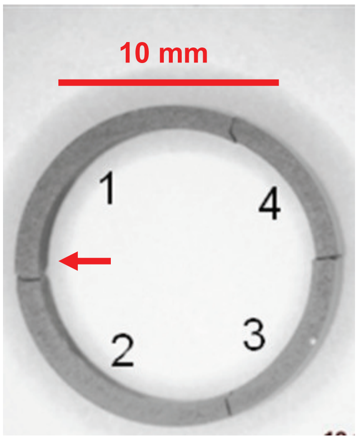

Figure 45. O-ring specimen fractured in bending test [120]. Red arrow indicating position in which micrograph shown in Figure 46 was taken.

The SEM image presented in Figure 46b shows the area indicated by a red circle on Figure 46a in a higher magnification. A pore with 80 µm length acting as a stress concentrator is visible a few µm under the sample surface. In the vicinity of this pore other elongated (although smaller) pores can be seen.

The fractographic analysis, performed by Yang [120] on other specimens tested in vacuum ($\sigma \approx 66$ MPa at 400 °C and $\sigma \approx 72$ MPa at 800 °C) also showed larger pores and surface defects which were assumed to be fracture origins.

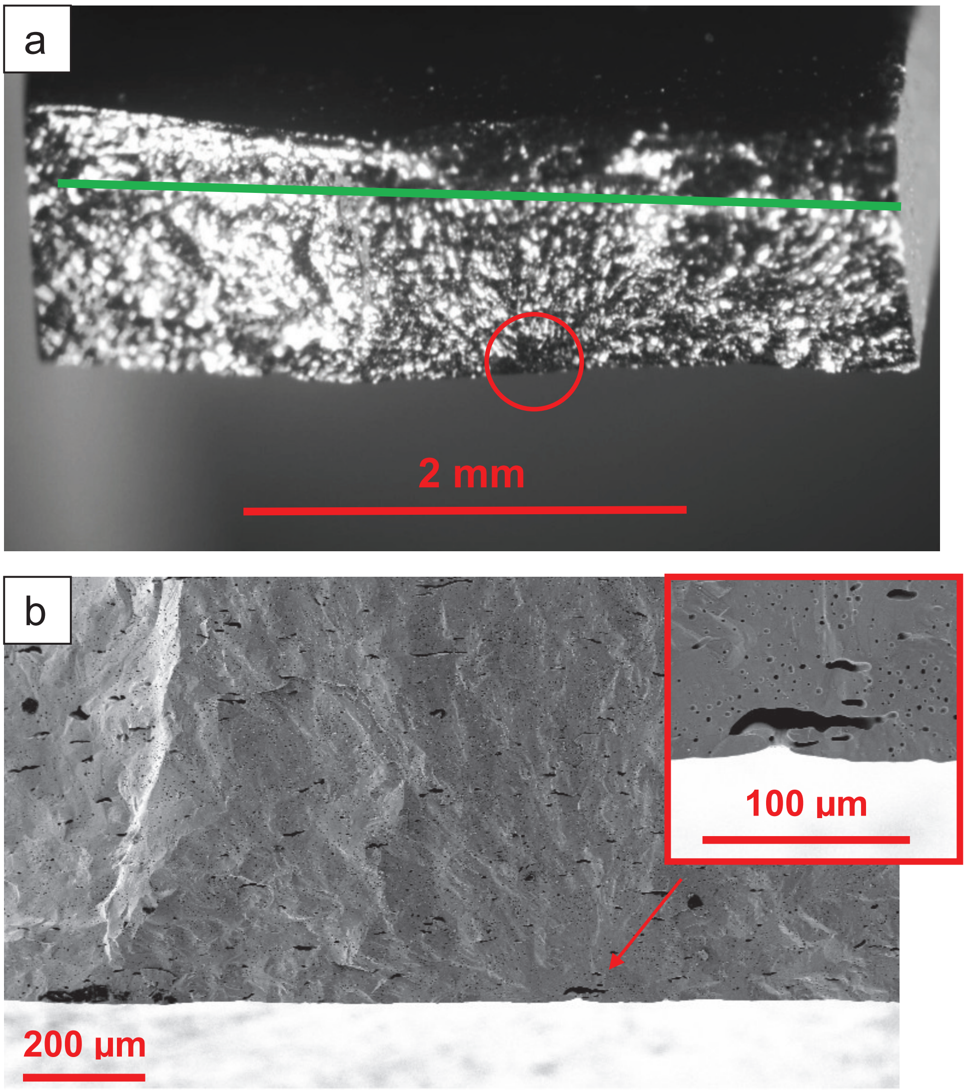

Figure 46. Fracture surface of the part 1 of specimen shown in Figure 45 a) overview of the fracture surface (stereoscopic LM), b) region of interest in higher magnification (SEM). Elongated pore localized below the sample surface (probable fracture origin) is indicated by a red arrow [120].

Further investigation of disc shaped BSCF specimens, supplied by the IKTS and tested in ring-on-ring configuration (see chapters 2.3.1 and 3.3.2), revealed a significant number of defects (Figure 47) like agglomerates, gaps and porous regions, which are presented in high magnification in Figure 48.

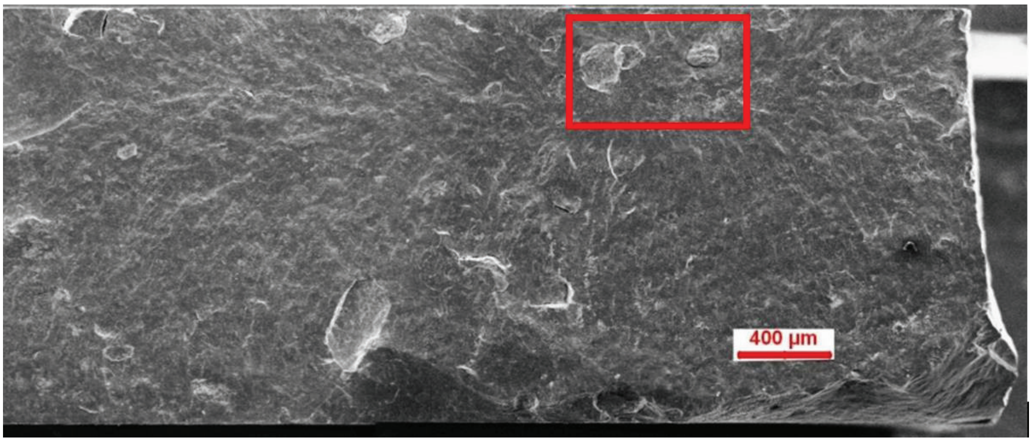

Figure 47. SEM image of fracture surface of a disc after ring-on-ring testing. The area marked by the red rectangle is shown in higher magnification in Figure 48.

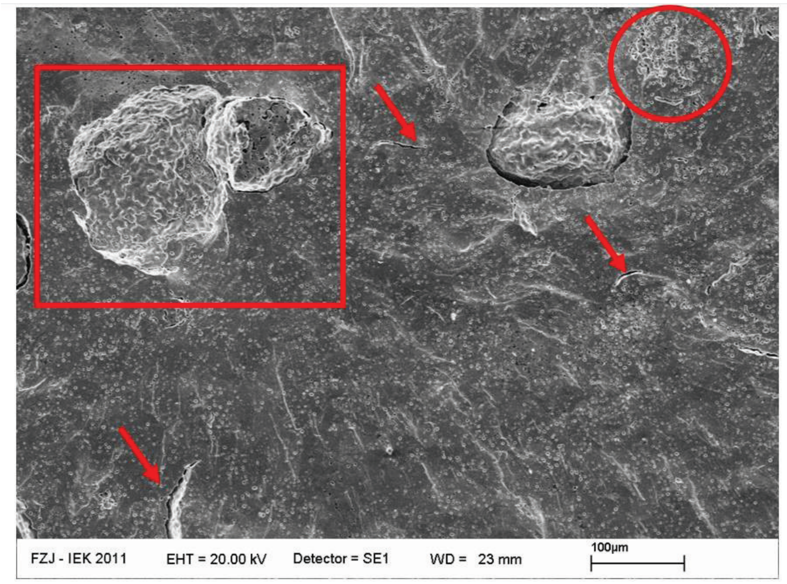

Figure 48. SEM image of details of the fracture surface from Figure 47. Agglomerates are marked by rectangles, voids by arrows, whereas the porous areas are marked by a circle.

One of the agglomerates, with a diameter of around 200 µm, placed closed to the surface in Figure 49, surrounded by a fracture mirror, appears to be the fracture origin of this specimen. Note that similar agglomerates were found in the tubes (Figure 43).

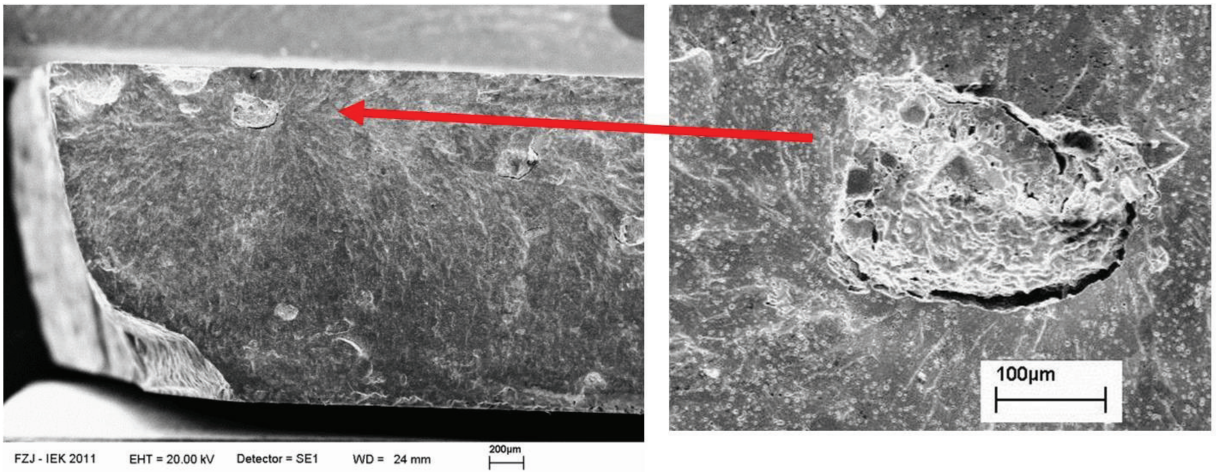

Figure 49. SEM image of a large agglomerate that acted as a fracture origin in BSCF material.

This proves that the production process has to be improved to avoid the presence of such large defects in order to improve the mechanical properties of the material.

3.2. Microstructure after heat treatment

In order to check the influence of annealing on the microstructure, microstructural investigation on heat treated specimens (following the procedure outlined for as–received specimens, reported in section 3.1) was carried out.

3.2.1. After annealing in air

In order determine the influence of the grain size on the creep behavior a set of heat treatments was performed to increase grain size of the BSCF specimens. Annealing at 1150 °C for 2 and 50 h resulted in a grain size increase from 26 ± 12 µm (as-received material) to 88 ± 33 µm and 140 ± 52 µm, respectively. Figure 50 presents the microstructures of the investigated specimens.

Local melting traces were found at the surface of the specimen annealed for 50 h. Analysis of the metallographic cross-section identified these molten zones as a surface effect only. Hence, these defects should not affect creep behavior.

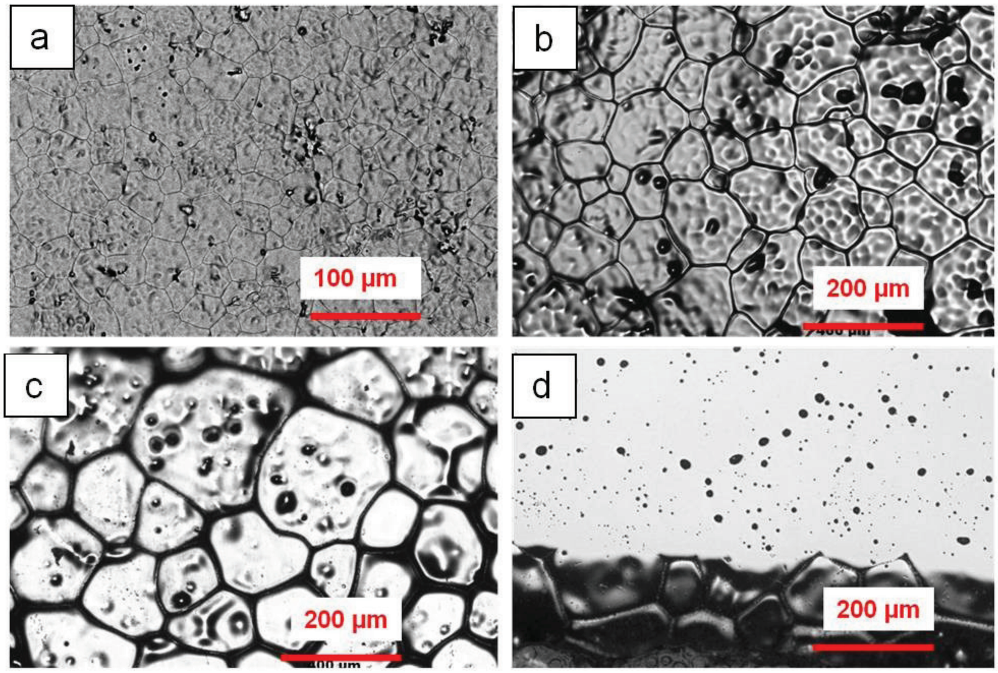

Figure 50. LM micrographs of the as-received BSCF (a); and after annealing at 1150 °C for: 2 h (b); 50 h (c); and 50 h (cross section of specimen showed on fig (b)). Images are taken from outer surface of tubes.

Due to four times higher cooling rates compared to the manufacturing process, no hexagonal phase was present after the annealing experiments, which was confirmed by LM investigation.

In order to investigate the phase equilibrium of the BSCF material at typical operating conditions, a set of long-time annealing experiments in the temperature range between 750 and 950 °C (with 50 K intervals) in air was performed. A dwell time of two weeks (336 h) was chosen for each treatment.

This thermal treatment revealed a significant influence of temperature on phase stability. At intermediate temperatures (between ~ 750 and ~ 850 °C) the cubic BSCF-phase was not stable. The material exhibits a two-phase microstructure, where the largest amount of the hexagonal phase was formed in the material annealed at 750 °C (Figure 51a).

In this case the hexagonal phase nucleates at the grain boundaries and inside the grains. The amount of hexagonal phase decreases when the annealing temperature is increased. Figure 51b shows the microstructure of a specimen annealed at 800 °C. It is clearly visible that the amount of hexagonal phase is smaller than in the previous case. Furthermore, at 800 °C precipitates nucleated only at the grain boundaries. Annealing performed above 850 °C resulted in a pure cubic BSCF structure (Figure 51c-e).

The above given results on the microstructure stability agree with the results on the long-term stability performed within the MEM-BRAIN project by Niedrig et al. [55]. The authors investigated cubic-to-hexagonal phase transformation by the XRD. About 40 days of annealing time at 800 °C was necessary to reach 90 % of the saturation level for the transformation of the cubic to the hexagonal phase (resulting in cubic to hexagonal phase ratio of 1:1). Note that short-term XRD measurements will not show hexagonal phase presence due to sluggish transformation kinetics and that the temperature range of hexagonal phase presence as well as the kinetics of its precipitation [55] are in good agreement with permeation drops reported in Ref. [34].

In order to investigate the kinetics of hexagonal phase transition in more detail, further annealing experiments were performed on material with an enhanced hexagonal phase quantity. A partition of the specimen subjected to annealing at 800 °C for 336 h (a microstructure shown in Figure 51b) received an additional heat treatment. The specimen was divided into three parts, and subsequently subjected to a thermal treatment according to the temperature – time sequence given in Figure 30. Microstructural analysis of the annealed specimens allowed the quantitative characterization and comparison of the hexagonal phase content after additional annealing at various conditions (Figure 52).

The microstructure of the first specimen (Figure 52a), which was removed from the furnace after annealing at 900 °C for 24 h, revealed that this relatively short annealing is already sufficient to dissolve the hexagonal phase that was created during the pre-annealing at 800 °C for 336 h (Figure 52d).

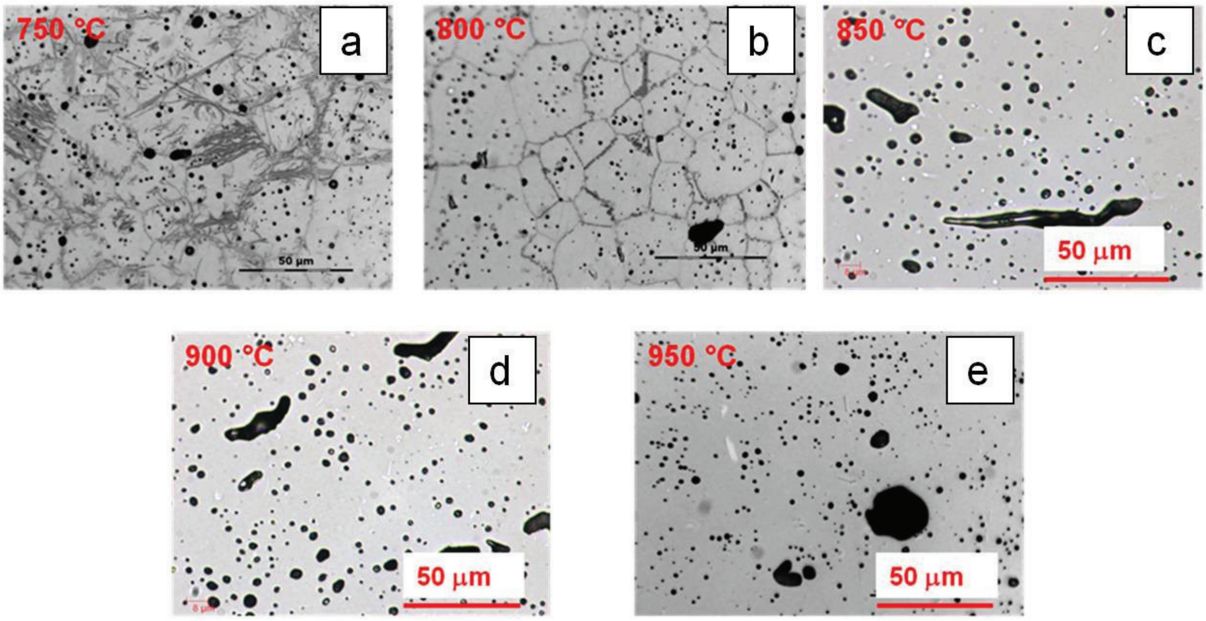

Figure 51. Microstructure of the BSCF specimens annealed in air for 336 h at: a) 750 °C, b) 800 °C, c) 850 °C, d) 900 °C and e) 950 °C.

The second specimen, treated additionally at 800 °C for 24 h, contains a small amount (2 %) of hexagonal phase, which nucleated at the grain boundaries (Figure 52b). A further increase of dwell time at 800°C to 100 h resulted in an increase of the hexagonal phase amount to 7 % (Figure 52c).

An additional annealing experiment was carried out according to the thermal history of a typical creep test (Figure 33). The first part of the experiment aimed on simulating (producing) the microstructure of the specimen subjected to the creep test at 850 °C during the heating sequence. Accordingly, the specimen was annealed at 850 °C for 88 h after being previously kept for 24 h at 750 °C. The subsequent cooling from 850 °C to RT was performed in air. Microstructural investigation performed after annealing revealed a two-phase microstructure (cubic + hexagonal) (Figure 53a) despite the fact that at 850 °C only the cubic phase is stable (according to previous annealing results presented in Figure 51 and in Ref. [55]).

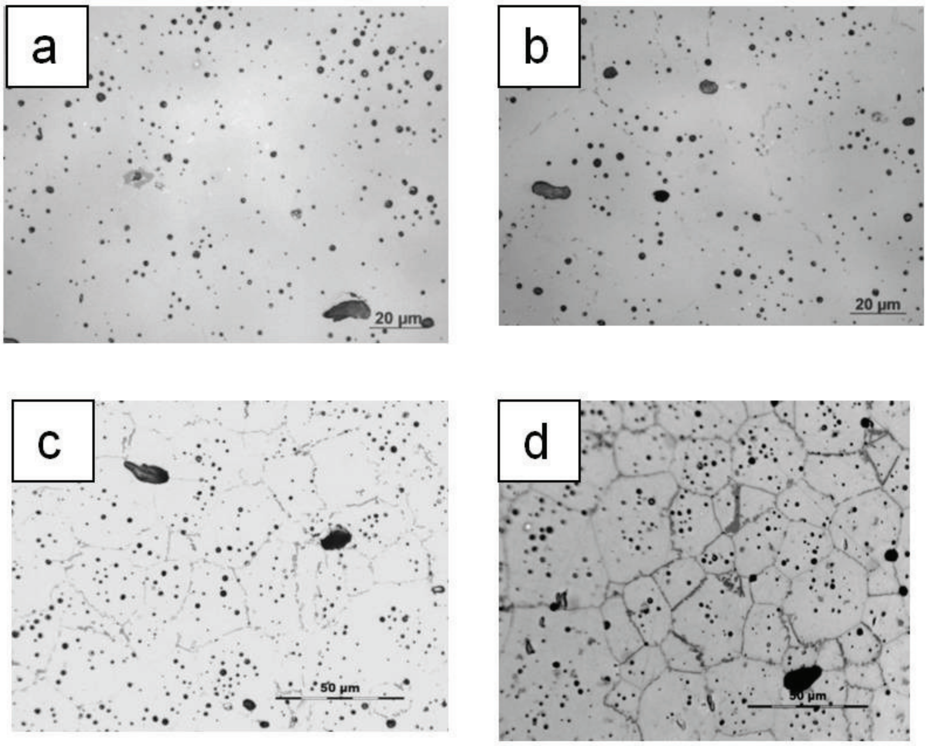

Figure 52. Microstructures of specimens annealed at 800 °C for different times: a) 0 h, b) 24 h, c) 100 h and d) 336 h.

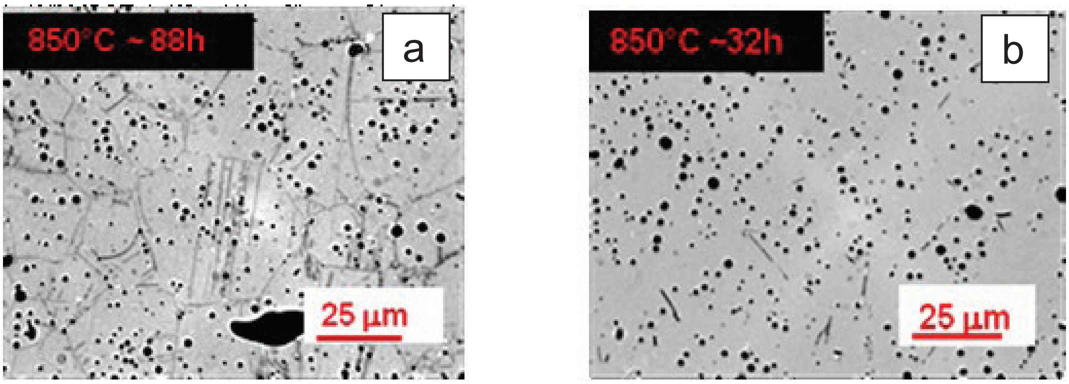

Figure 53. Microstructures of a specimen annealed in air at 850 °C a) 88 h during heating sequence and b) 32 h during cooling sequence.

The second part of the heat treatment aimed to simulate the microstructure of the BSCF tube subjected to creep at 850 °C during the cooling sequence. Therefore, after annealing at 950 °C for 24 h, the specimen was cooled down to 850 °C and annealed at this temperature for 32 h. Subsequently, it was cooled to RT in air. Microstructural investigation performed after this heat treatment revealed a single-phase BSCF microstructure (Figure 53b).

From the results described above it can be concluded that the kinetics of the hexagonal phase creation at 750 °C (24 h were sufficient to create significant amount of the hexagonal phase) is rather fast and the kinetics for the reverse transition at 850 °C (88 h were not enough to dissolve the previously formed hexagonal phase) is sluggish.

During the cooling sequence starting at 950 °C BSCF has an entirely single-phase cubic structure, since hexagonal phase dissolution takes place very fast after heating to 950 °C (around 24 h are sufficient to obtain homogeneous cubic phase). Upon further cooling the necessary conditions for the formation of the hexagonal phase do not exist, unless the material would be cooled down to a temperature lower than 850 °C.

The length of the membrane tubes which are exposed in the separation unit shown in section 2.7 is about 0.5 m, in large scale application the dimensions might be at least one order of magnitude larger. For such large dimensions, the potential effect of the inhomogeneous temperature field inside the operation unit needs to be taken into consideration. Accordingly, significant temperature gradients which might occur along the tube length can result in the corresponding microstructure variation of the membrane. Such differences in microstructure might influence mechanical properties of the membrane. This issue will be discussed later in section 3.6.

3.2.2. **After annealing in vacuum**

A similar set of heat treatments as described in the section above for annealing in air was performed under vacuum (section 2.5). However, the annealing time was limited to 100 h and, in order to exclude the possibility of distortion introduced by hexagonal phase residues after manufacturing process (Figure 41), an additional pre-annealing at 950 °C/ 24h was applied. Note that annealing in air at 800°C for 100 h generates noticeable amount of hexagonal phase (Figure 53c) and in case of 750°C even 24 h is enough to observe a phase transformation (Figure 53a, where hexagonal phase was created in air at 750°C / 24 h and did not dissolute completely after annealing at 850°C for 88h). Neither annealing tests performed under pO_2 of 10^{-5} mbar at various temperatures between 650 and 800 °C (with 50 K intervals), nor one treatment carried out at 800 °C under 4 mbar oxygen partial pressure, resulted in recognizable cubic-to-hexagonal phase transformation. These results agree with the results of XRD measurements performed by Ovenstone et al. [33].

In Figure 54 the microstructure of the specimen annealed at 800 °C for 100 h under oxygen partial pressure of 10^{-5} mbar is shown.

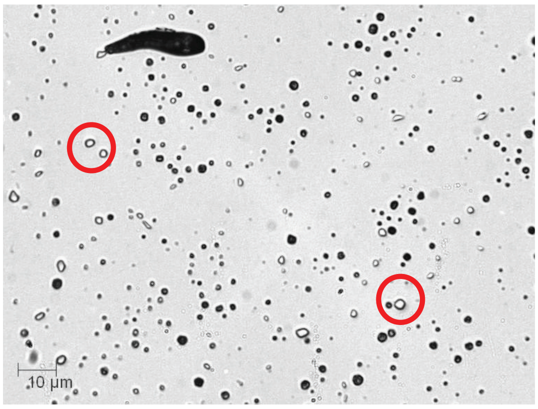

Figure 54. Microstructure after annealing at 800 °C for 100 h under oxygen partial pressure of 10^{-5} mbar. Small CoO precipitates are visible (indicated by red circles).

In the specimen presented above, as well as in all other specimens annealed under pO_2 of 10^{-5} mbar for 100 h (see section 2.5), cobalt oxides (CoO) were found, which is in agreement with Co-O phase diagram presented by Niedrig [121] (Figure 55).

Quantitative analysis of the CoO content was not performed. However, the pre-annealing at 950 °C for 24 h (performed to dissolute possible hexagonal phase in the material) seems to affect the number of the precipitates. Note that raised CoO density was found close to surface.

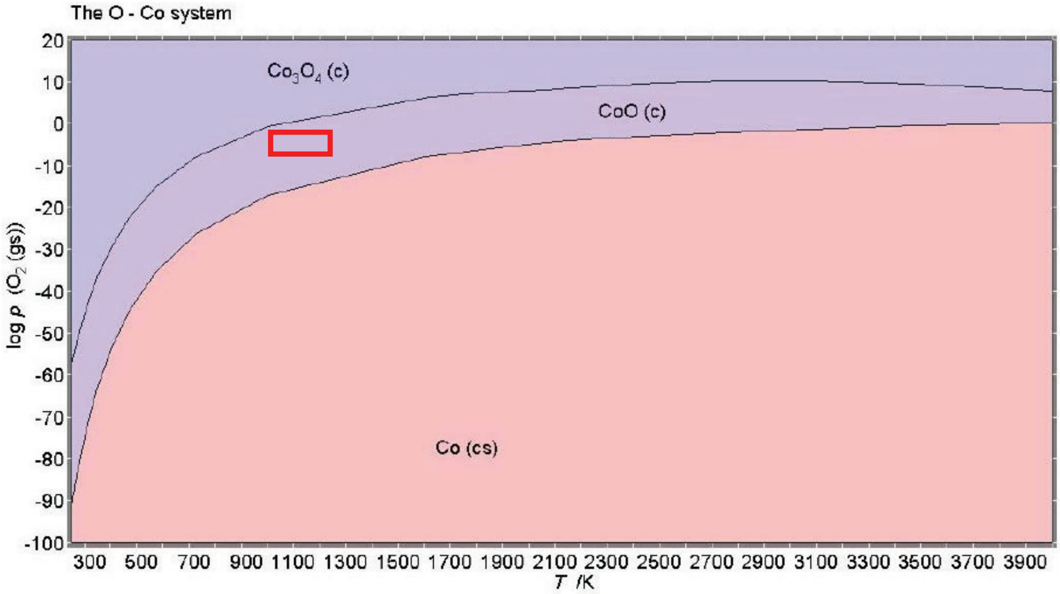

Figure 55. Co-O phase diagram, reprinted after [121] showing the stability region of CoO. The area marked with the red rectangle shows the range in which annealing experiments were performed.

Additionally, after annealing at 800 °C for 100 h under pO_2 of 10^{-5} mbar, a thin layer of CoO has been formed close to the surface, right below the layer formed by deposition of elements evaporated from heating elements (Figure 56). This CoO layer might result from cobalt diffusion to the surface layer deposited from the furnace's heating elements (Figure 63, Table 10).

In the demonstrator tubes cobalt oxides were not observed, probably due to a higher oxygen content over the complete cross section than under vacuum annealing as a result of the transport of oxygen during the operation of the demonstrator tubes. However, presence of cobalt oxide was revealed for the specimen subjected to a creep test under 10^{-5} mbar (chapter 3.2.4). Accordingly, it can be concluded that BSCF is not stable for low oxygen partial pressures. However, measurements to determine a time dependency of CoO formation were not carried out. Accordingly, no information was obtained if the 3 % of CoO revealed by XRD after creep test in vacuum (Figure 64) already corresponds to a saturation level.

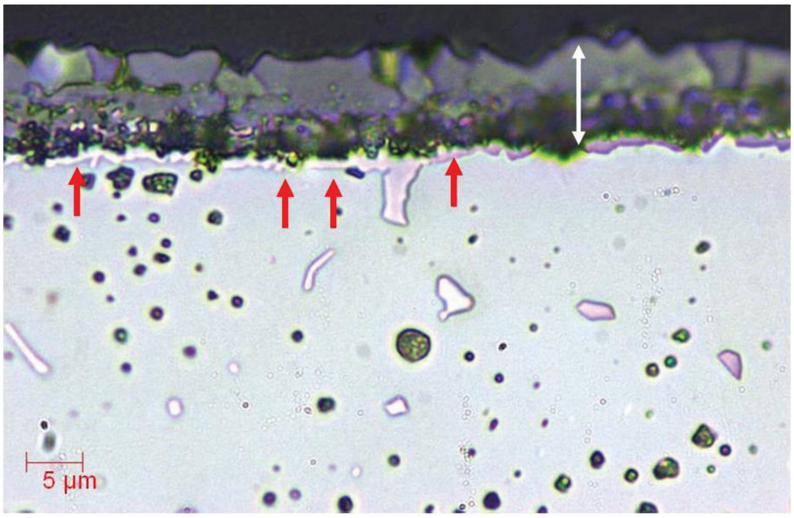

Figure 56. Microstructure of specimen annealed in 10^{-5} mbar. A thin CoO layer is indicated with red arrows.

However, it can be stated that under vacuum conditions the chemical stability problems of the BSCF are not due to hexagonal phase formation but might be due to cobalt oxide reduction, which proceeds according to the following reaction [122]:

$$Co_3O_4 \xrightarrow{830\text{-}890^{\circ}C} 3CoO + 1/2O_2$$

Note that in as-received material only Co_3O_4 precipitations were found. The number of CoO after treatment in vacuum is significantly higher than that of Co_3O_4 in the as received material. This means that not only a cobalt oxide transition takes place, but also local diffusion of Co ions from the BSCF matrix is present (resulting in growth of the oxides). Reduction of Co ions in the BSCF lattice can lead to incorporation of oxygen ions to maintain charge neutrality, which can result in a decrease of oxygen permeation.

In the case of heat treatment under air the reaction given above can be reversed [123]. The oxygen present in air enables the CoO to be changed to the Co_3O_4 upon cooling. In vacuum, however, the insufficient amount of oxygen in the atmosphere precludes the oxygen re-absorption and diffusion into material. Accordingly, a cobalt oxide that was reduced at the elevated temperature remains in its reduced state to room temperature.

3.2.3. **Fractography of annealed material**

Fractographic investigation was also performed for heat treated specimens, after fracture testing in O-ring geometry. All specimens showed an intergranular fracture mode.

The specimens whose fracture surfaces are presented in Figure 57 and Figure 58 were loaded under an oxygen partial pressure of 10^{-2} mbar at 200 °C after pre-annealing at 950 °C / 24 h, which was carried out to dissolve the hexagonal phase in the as-received material. Fracture stress in this case was calculated to be 65 MPa. Surface defects (Figure 57) and large pores (Figure 58) were identified as probable fracture origins.

Note that presence of hexagonal phase appears not to have an influence on fracture stress up to 600 °C (see section 3.4.1).

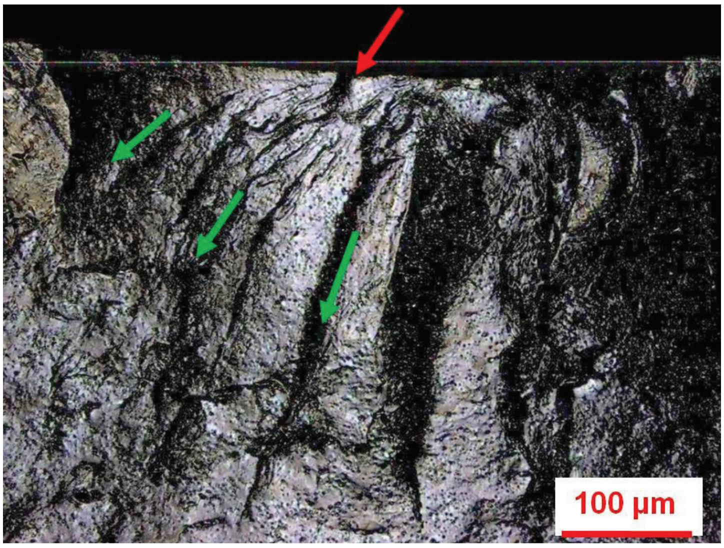

Figure 57. Fracture surface of a specimen tested under an oxygen partial pressure of 10^{-2} mbar at 200 °C. Twist hackles are marked by green, the fracture origin by a red arrow.

The pronounced twist hackles shown in Figure 57 allow an identification of the fracture origin (indicated by red arrow) and the direction of local crack propagation (marked by green arrows). Note that the upper part of the fracture surface was loaded in tension and the crack propagation was roughly perpendicular to the applied principal stress direction.

Figure 58 shows another part of the fracture surface of the previously described specimen, also located close to the outer surface loaded in tension. Again, a transgranular fracture mode is well visible. The large elongated pore obviously influences the stress distribution. Additional thinner, long pores are visible too. The wake hackles are originating from small round pores, indicating the crack propagation direction (marked by green arrows).

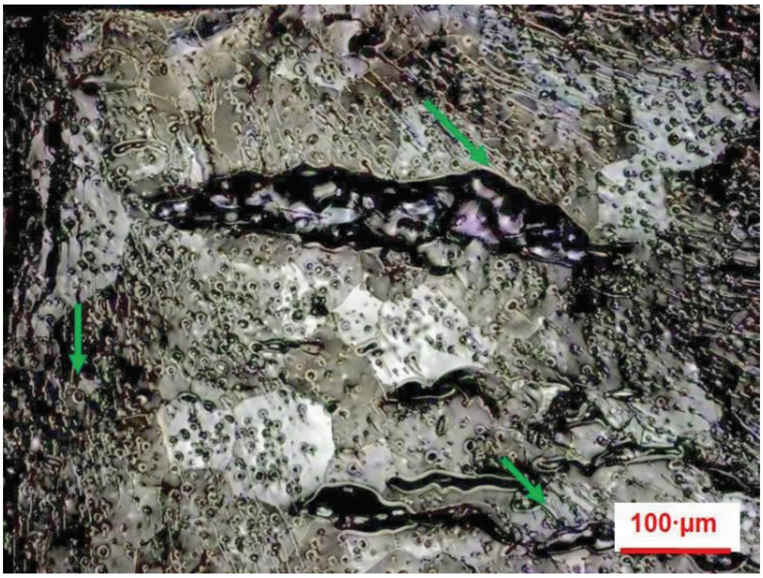

Figure 58. Fracture surface of a specimen tested under $pO_2 = 10^{-2}$ mbar at 200 °C. Large pores are visible. The green arrows indicate the crack propagation direction.

In Figure 59 a specimen tested in air at 400 °C, after being previously annealed at 750 °C for 150 h, is shown. The preceding annealing was performed to create a large amount of hexagonal phase in the material. A fracture stress of 57 MPa was obtained. The fracture origin was found to be localized close to the outer sample surface. In spite of the large amount of hexagonal phase (not visible in Figure 59 due to a rough surface and too low magnification) the fracture mode was similar as for material without hexagonal phase.

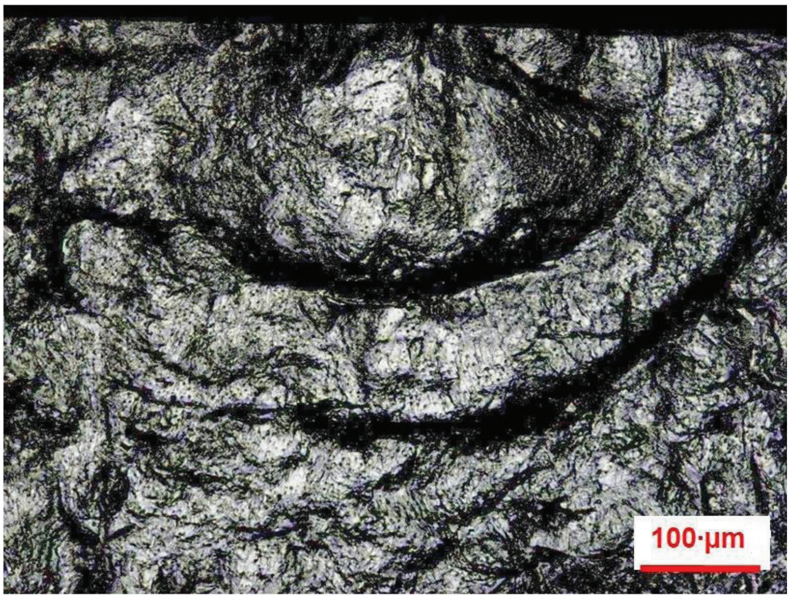

Figure 59. Fracture surface of a specimen tested in air at 400 °C after pre-annealing at 750 °C/150 h.

3.2.4. **BSCF tubes after creep test**

Microstructural investigation was performed on the specimens subjected to the creep tests (described in more detail in section 2.6.1) in air as well as under vacuum.

In case of compressive creep of tubular test pieces in air at 30 MPa the microstructural analysis was performed at the outer surface of the specimen. Opening of the grain boundaries oriented parallel to the load direction was observed (Figure 60a).

Similar investigation of specimens after compressive creep in vacuum (10^{-5} mbar oxygen partial pressure; applied creep stress = 30 MPa) was more difficult due to evaporation of material from the furnace's heating elements and subsequent reaction with the tube's outer surface (Figure 60b). Therefore, the grain structure was observed at the inner surface of the specimen (Figure 60c). The average grain sizes of the two BSCF specimens separately tested under vacuum and air environment was 30 ± 12 µm and 32 ± 13 µm, respectively. These small differences compared to the as-received material, are within the standard deviation and can therefore be neglected. Very fine secondary-phase precipitations, identified as cobalt oxide particles, were found at the inner surface of the sample subjected to creep in vacuum (Figure 60c). Additionally, some indications of grain boundary sliding (the surface of some grains lies above the average level surface after creep), were observed in case of both atmospheres.

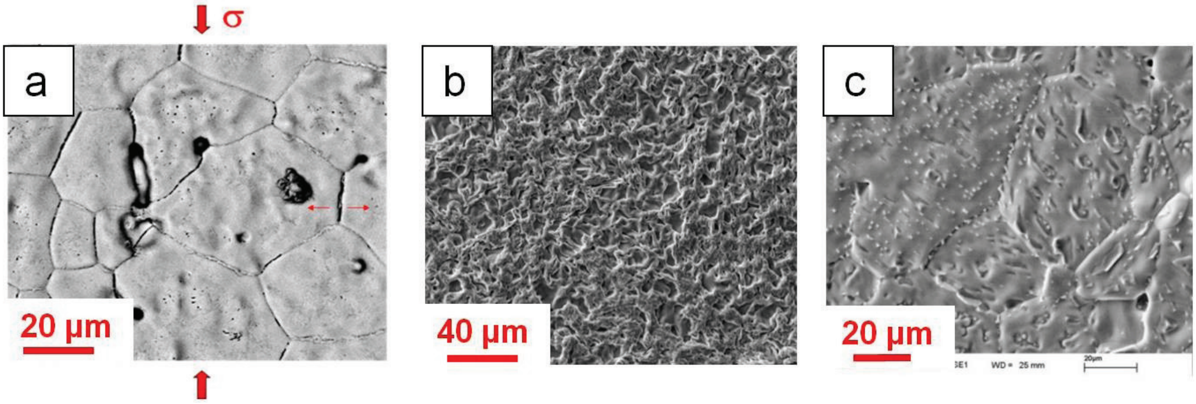

Figure 60. BSCF specimens after creep test at 30 MPa. a) In air - outer surface, b) in vacuum (10^{-5} mbar) - outer surface and c) in vacuum (10^{-5} mbar) - inner surface.

Microstructural analysis after compression creep under a load of 63 MPa in air revealed a large amount of widened grain boundaries parallel to load direction, implying more creep rupture (Figure 61) than observed after creep testing with a load of 30 MPa (Figure 60a).

The grain boundary sliding (GBS) mechanism, responsible for widening of grain boundaries is explained in Figure 21 [102]. Grains subjected to compressive loading are sliding relative to each other along grain boundaries inclined to the load direction, where the applied compressive stress is converted to shear stress. The resulting horizontal grain movement results in widening of the longitudinally directed grain boundaries

(Figure 61a). The occurrence of grain boundary widening in the radial direction is additionally indicated by some “push out” of surface grains in radial direction.

Moreover, micro-cracks (as a result of testing or subsequent cooling) propagating from surface pores were found inside the material (Figure 61b), being a further potential fracture origin in creep loading.

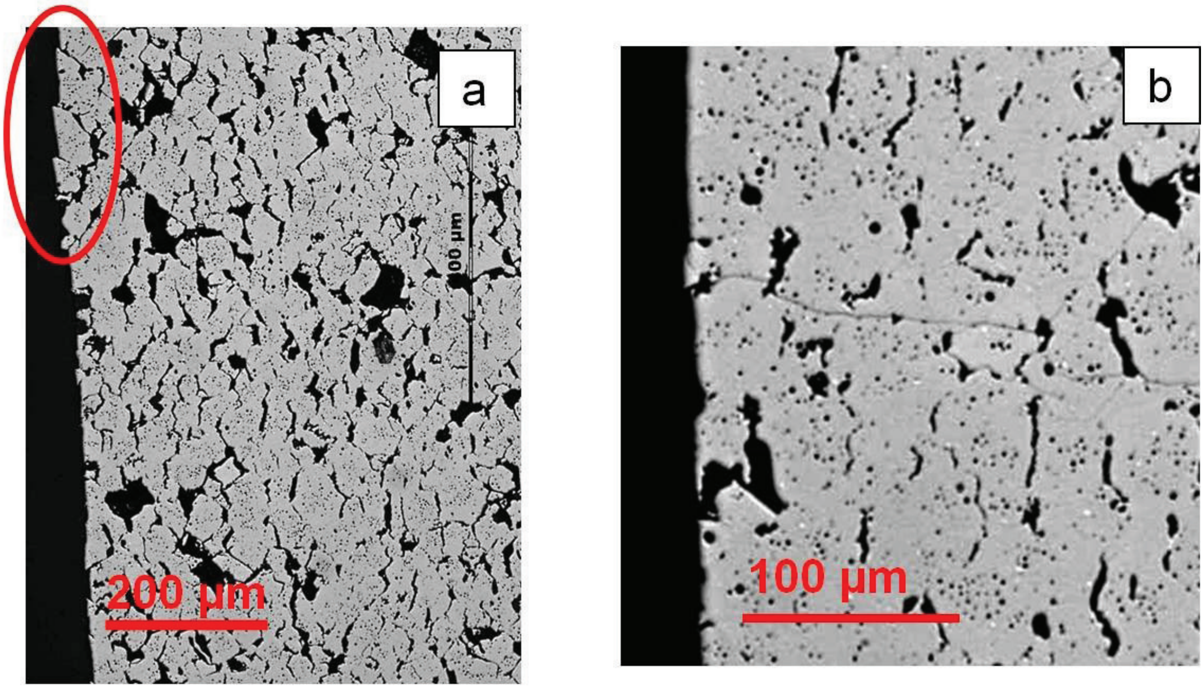

Figure 61. Creep damage observed in the cross-section of a specimen tested under a load of 63 MPa in air, a) large amounts of voids as a result of local transverse tensile stress induced by GBS (see Figure 20 for reference), and b) micro-crack which could be a potential fracture origin.

Beside the creep damage investigation, also phase composition changes were investigated at cross-sections of creep specimens loaded with a compressive stress of 30 MPa. The microstructure of the specimen tested in air is similar to that of specimens annealed in air at temperature of 950 °C (Figure 62a). A specimen creep tested under vacuum of 10^{-5} mbar at a stress of 30 MPa showed an increased amount of CoO precipitates in the microstructure (Figure 62b), similar as observed in the case of material annealed in vacuum (Figure 54). However, the influence of creep on CoO amount was not investigated in detail.

Further SEM analysis performed at cross-sections of the specimen tested in vacuum at 30 MPa revealed that differences in surface morphology were caused by evaporation from the molybdenum-containing heating elements of the furnace and subsequent deposition on the specimen surface.

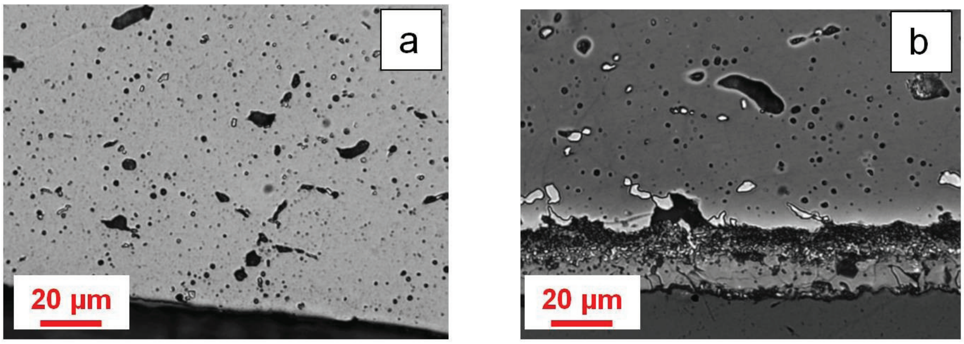

Figure 62. LM micrographs of the cross-sections of specimens crept at 30 MPa in: a) air, and b) 10^{-5} mbar vacuum.

An SEM image of a cross-section of a specimen creep tested in vacuum is presented in Figure 63. At the left side of the image, two molybdenum-rich layers with overall thickness of 20 µm are visible. Those thin layers can have influence on the specimen’s oxygen stoichiometry due to possible reduction of oxygen permeation (similar to carbide layers forming on surface in case of CO_2 presence – see chapter 1.4). However, this should have no influence on creep behavior due to obligatory pre-annealing at 850 °C for 24 h applied for each specimen in order to reach an equilibrium state (see chapter 3.5.1). Note that similar layers at the surface were observed for BSCF specimens annealed in vacuum. Microstructures after annealing in vacuum are given in chapter 3.2.2.

The white precipitations visible in the LM image at the sample cross-section (Figure 62b) were identified by SEM-EDX as CoO-phase (Figure 63, Table 10) with a volume fraction of 3 %, confirmed by XRD (Figure 64). Due to different properties (TEC, *E*) of

CoO than of BSCF, the presence of CoO precipitates might induce changes of the local stress field during both, heating (cooling) as well as after longer time of operation, which might lead to crack formation and accelerated material failure.

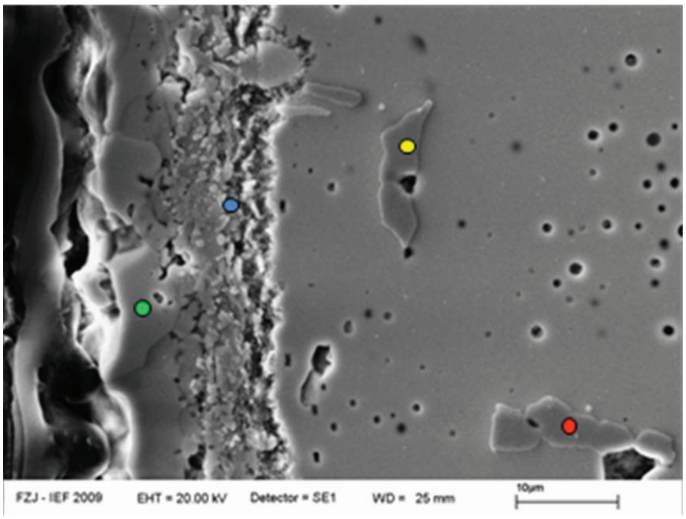

Figure 63. SEM image of a cross-section of a specimen creep tested at 10^{-5} mbar oxygen partial pressure at 30 MPa.

Table 10 Results of EDX measurements performed at the four points marked in Figure 63.

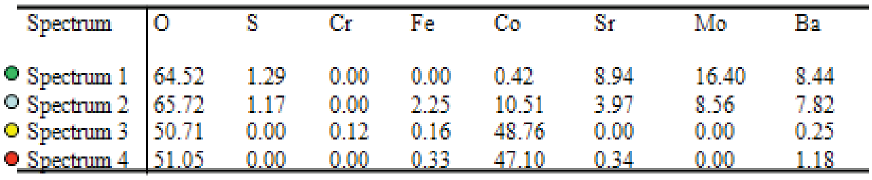

Spectrum	O	S	Cr	Fe	Co	Sr	Mo	Ba
🟢 Spectrum 1	64.52	1.29	0.00	0.00	0.42	8.94	16.40	8.44
🔵 Spectrum 2	65.72	1.17	0.00	2.25	10.51	3.97	8.56	7.82
🟡 Spectrum 3	50.71	0.00	0.12	0.16	48.76	0.00	0.00	0.25
🔴 Spectrum 4	51.05	0.00	0.00	0.33	47.10	0.34	0.00	1.18

In addition to the microstructure analyses of specimens loaded in compression creep, some specimens were also investigated after creep testing in C-ring bending geometry. The large macroscopic deformation obtained during creep of a C-ring specimen at 900 °C is illustrated in Figure 65 which compares a deformed specimen with the geometry in the as-received material.

An analysis of grain size at two different positions (across the wall thickness) of the C-ring (Figure 65) after creep test was performed. After creep deformation for 100 h at 900

°C with an applied load of 6.7 N, no difference in grain size or aspect ratio (AR) between areas exposed to high temperature only (d = 27 ± 13 μm, AR = 1.4 ± 0.28) and areas exposed to stress and temperature (d = 26 ± 12 μm, AR = 1.4 ± 0.26) was found (see Figure 65). However, continuous chain of small precipitates at the grain boundaries and inside the grains were found (Figure 66).

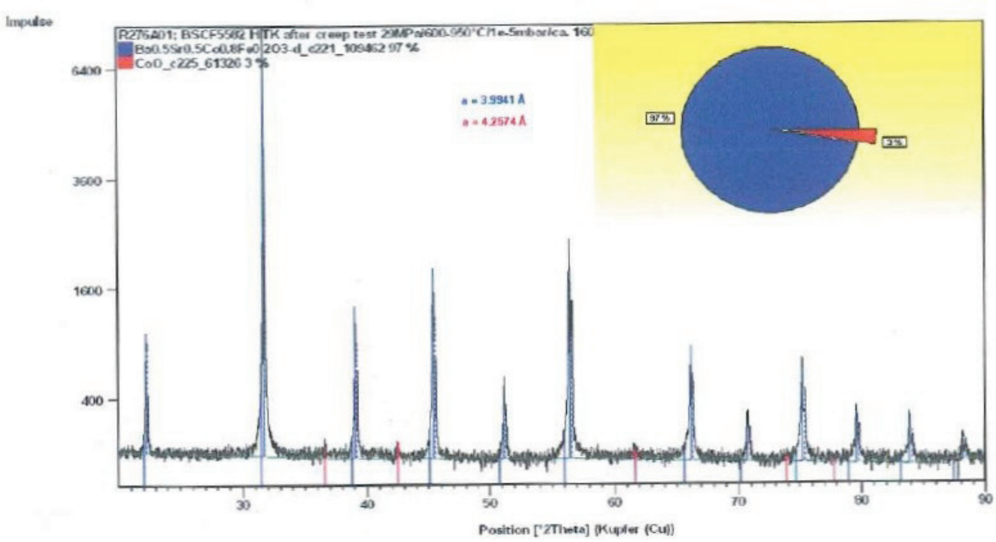

Figure 64. XRD results showing presence of cobalt oxides after creep in vacuum.

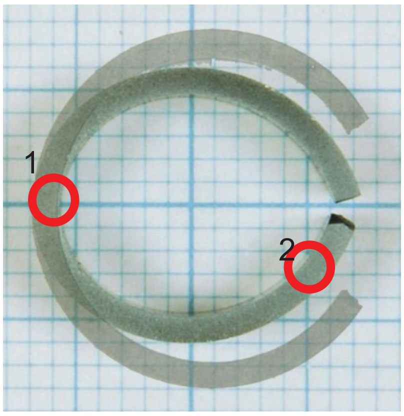

Figure 65. Comparison of as-received C-ring specimen with the geometry after creep at 900 °C. Marked areas indicating the places exposed to load and high temperature (1) and only high temperature (2).

The SEM-EDX analysis performed at surface grains containing such precipitates revealed sulfur, oxygen, barium as well as chromium, whereas strontium, iron and cobalt could not be found (Figure 67).

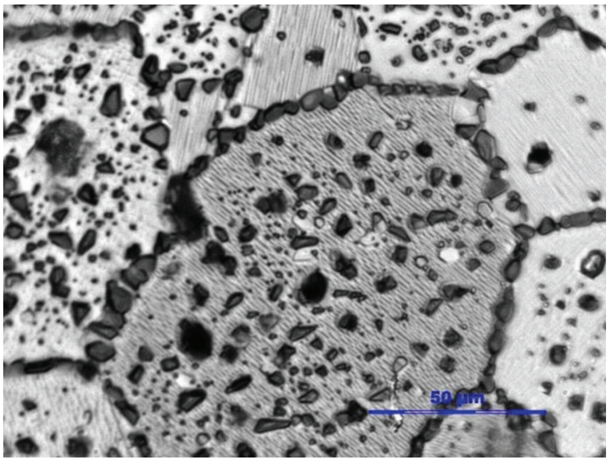

Figure 66. LM image of a specimen after creep in C-ring geometry.

The presence of chromium can be explained by evaporation from the furnace’s heating elements and sublimation at the specimen surface, like in case of molybdenum found in specimen after compressive creep tests under vacuum (Figure 63). Note that these two types of creep tests were performed in different furnaces with different chemical composition of the heating elements.

For the sulfur enrichment at the specimen surface, at least three reasons could be found: 1) sulfur is dissolved in $BaCO_3$, which is one of the basic ingot components used for the BSCF production. During thermal treatment, sulfur might diffuse to the surface; 2) sulfur might be adsorbed from laboratory air and 3) sulfur is present in the refractory ceramics used for the furnace padding. Note that presence of barium sulfates ($BaSO_4$) was also reported in the literature for BSCF hollow fibers [124, 125].

The SEM investigation performed on the material after creep testing in C-ring geometry proved that creep damage indicated by void formation occurs at the grain boundaries in the tensile loaded regions of the specimen (Figure 68).

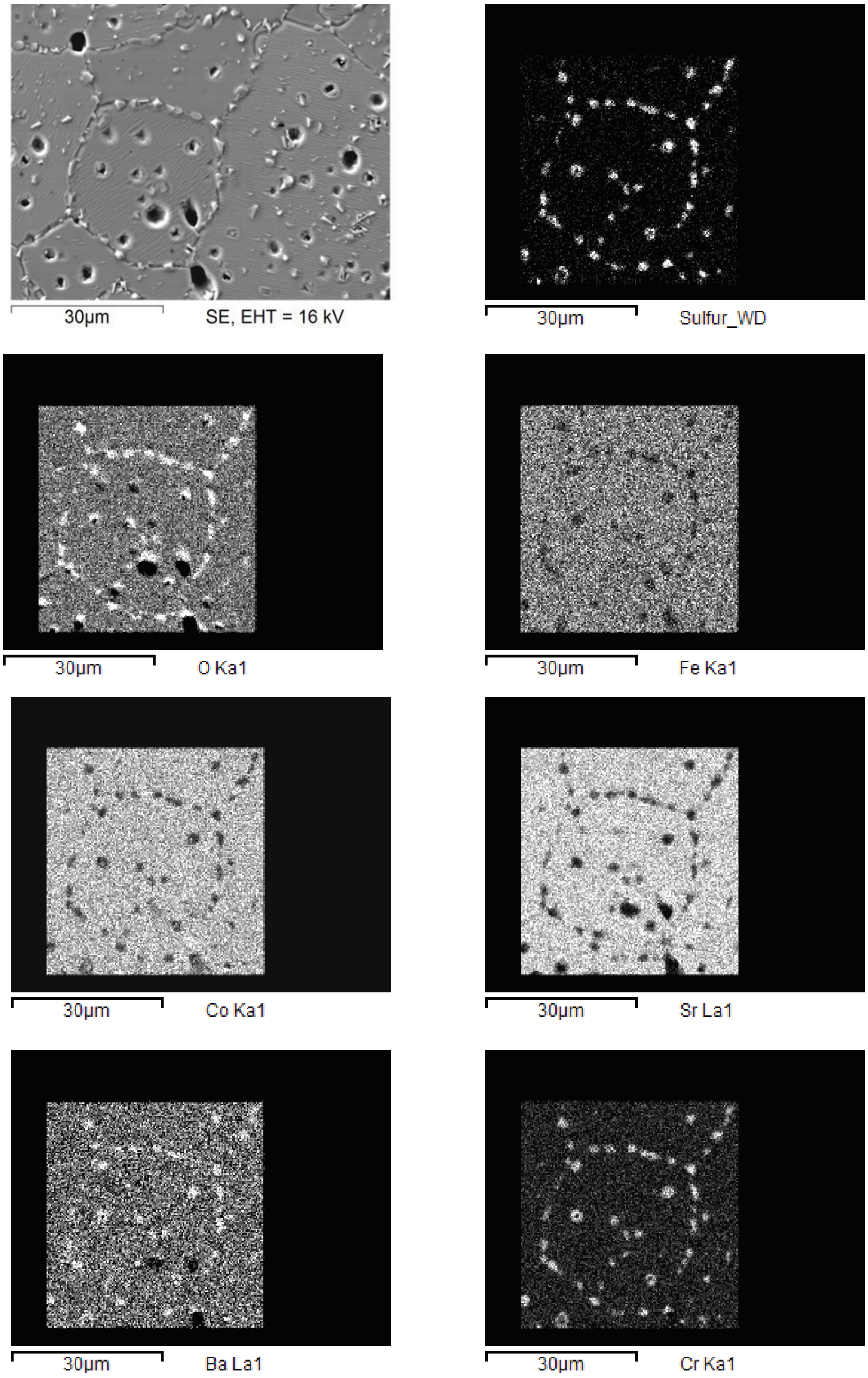

Figure 67. SEM-EDX element mapping of near surface grains of a C-ring specimen after creep test in air at 900 °C for 100 h.

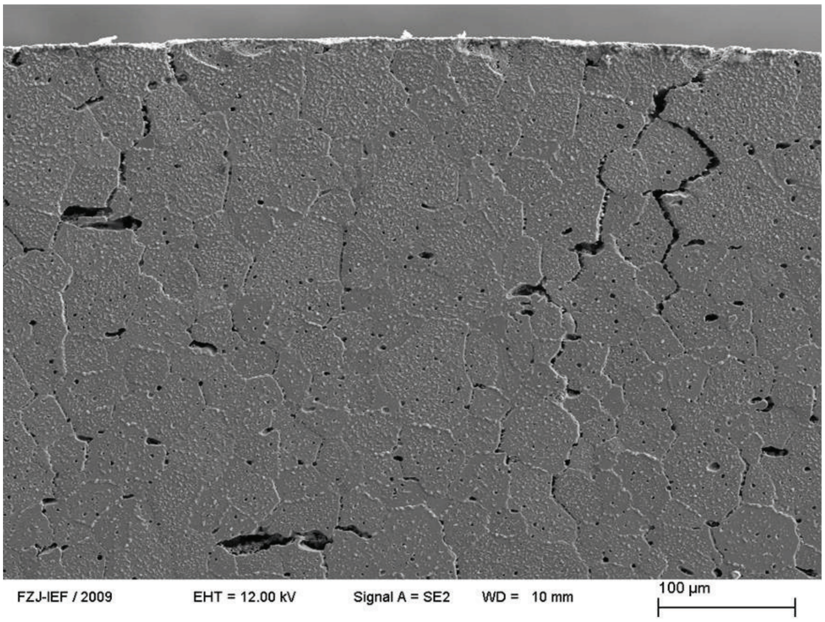

Figure 68. SEM image showing grain boundary damage after C-ring creep test.

More detailed microstructural analysis allows to identify the damaged zone in creep tested C-ring specimen (Figure 69). The limit of the region where cracks could be observed is marked with a red line.

Also the curvature of C-ring specimens after creep testing was measured. The red circle in Figure 69 indicates the margin of the area, in which significant non-elastic deformation occurs. Material at the right hand side of the red spot was deformed mainly elastically, since the observed curvature after unloading follows the shape of the as-received specimen. At the left side of this critical point, curvature is different from that of the as-received state. The critical strain, at which elastic deformation starts, was estimated to 0.2 %, using the following procedure: From the Equation 18 [126], describing elastic stress distribution in a C-ring specimen the stress in the area, where transition from elastic to non-elastic deformation took place (red circle in Figure 69) was calculated. Then, elastic strain was calculated from stress, using the Equation 19.

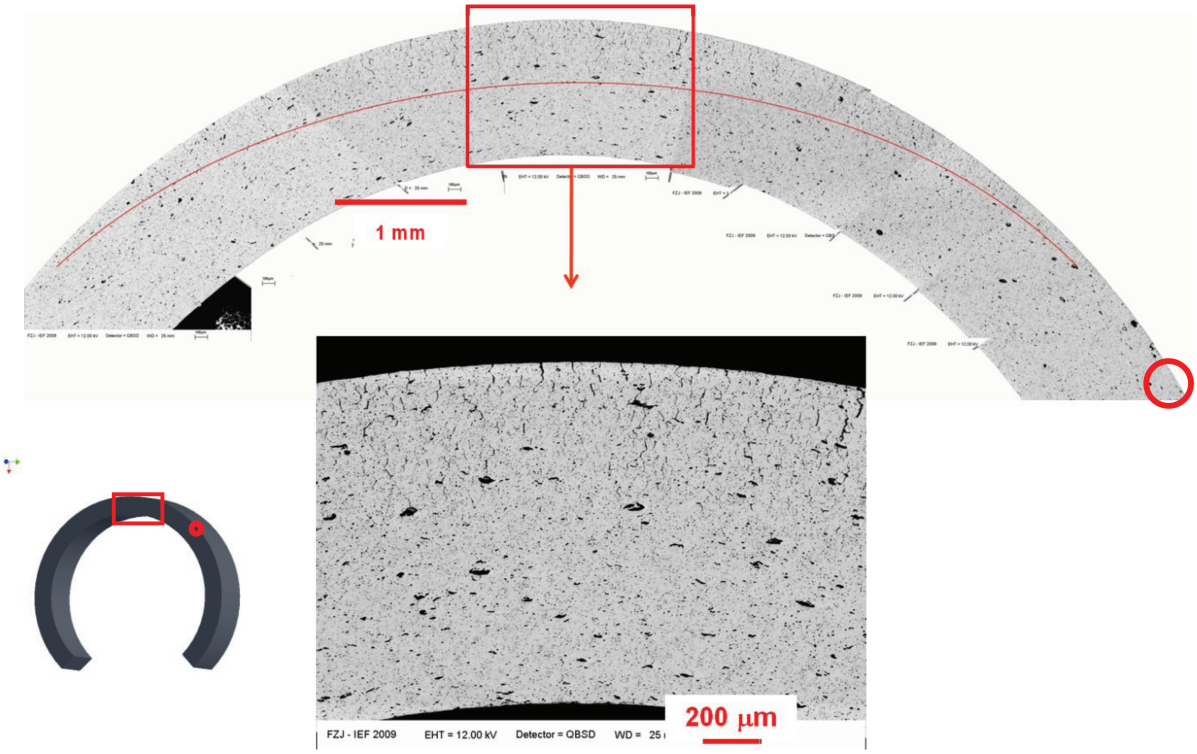

Figure 69. Detailed view of the damage zone (upside the red line).

$$\sigma_e = \frac{P}{bk}\frac{R}{r}\frac{r-r_a}{r_a-R}\cos\theta$$

Equation 18.

where: σ_e – elastic stress, P – applied load, b – width, k– thickness, $r_a = (r_o+r_i)/2$, $R = (r_o-r_i/\ln(r_o/r_i)$, r_o – outer radius, r_i – inter radius.

$$\varepsilon_e = \frac{\sigma_e}{E} * 100\%$$

Equation 19.

where: ε_e – elastic strain.

Hence, creep rupture damage of the tubes is assumed to occur as soon as the tensile strain limit of 0.2 % is exceeded. Under compression, creep rupture perpendicular to the loading direction occurred when the strain reached~ 4 %.

3.2.5. **Fractography**

The defects previously observed for disc-shaped material (see section 3.1.3), were also observed for tubular specimens and may contribute to material failure. Figure 70a presents a BSCF tube after creep at T = 750 °C with a creep stress of 30 MPa under an oxygen partial pressure of 4 mbar. A “chip-like” fracture, caused by high stresses generated by presence of a flaw, is visible at the outer specimen side (Figure 70). Failure started at this fracture initiator, marked by a red arrow in Figure 70b, and propagates across the tube. The chip described above is the primary fracture origin which is proved by its presence on both fracture surfaces [79].

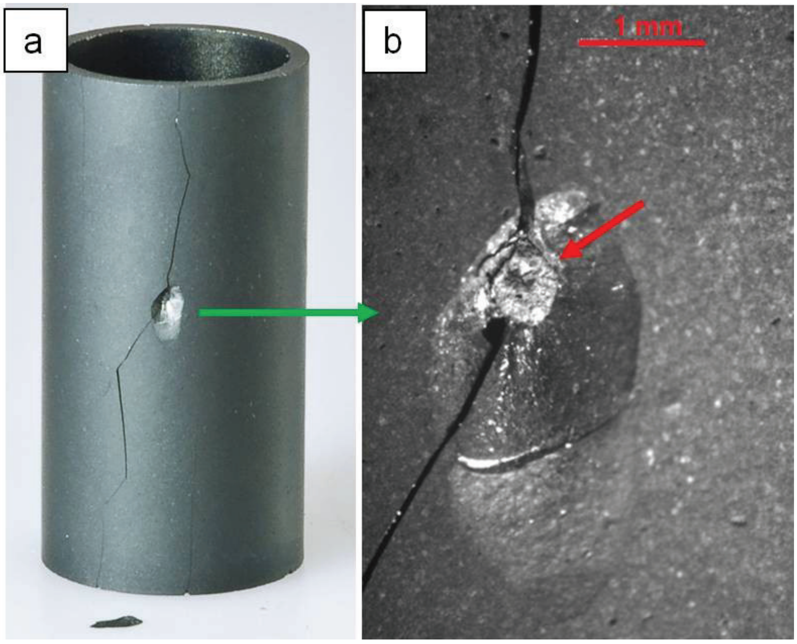

Figure 70. Tubular specimen after compressive creep test. a) overview, b) chip fracture at the outer surface in higher magnification.

Additionally, a crack propagating from an edge defect generated by grinding was found (Figure 71).

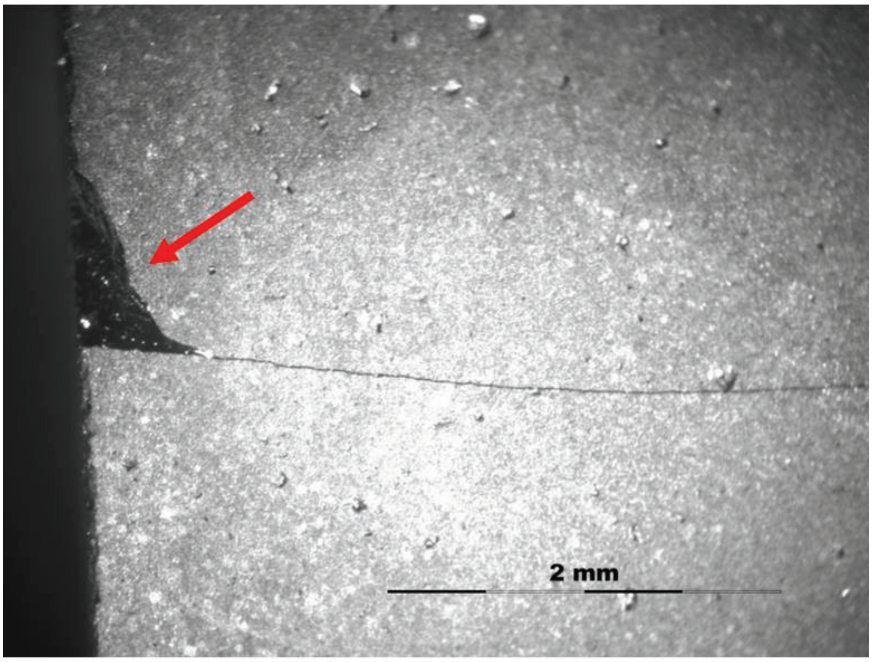

Figure 71. Edge damage introduced during grinding as a crack initiator.

3.3. Mechanical properties of as-received material

In addition to micro- and macro-mechanical tests at RT, macro-mechanical tests at elevated temperatures were performed on as-received material in order to obtain a comprehensive characterization of the BSCF mechanical behavior.

3.3.1. Depth-sensitive Indentation

To obtain mechanical properties of single grains and phases, depth sensitive indentation was used to measure local Young’s modulus, micro-hardness, and fracture toughness of the BSCF at room temperature.

Young’s modulus and micro-hardness were measured by applying a load between 10 mN and 1 N. The fracture toughness estimation was, in order to assure a critical load to induce measureable cracks, based on imprints with a load of 1 N. A typical indentation imprint after applying a load of 1 N is shown in Figure 29.

The local porosity of the material had a significant influence on indentation results. Pores that are relatively large compared to the indentation imprint can result in a large scatter of the measured local properties which is reflected in an increased standard deviation. Obviously erroneous results (mainly caused by individual large pores) were excluded from the subsequent evaluation. The average values and corresponding standard deviations were calculated from the remaining data.

Resulting Young's moduli and micro-hardness values are displayed in Figure 72. A clear decrease of average Young's modulus is visible when the applied load is increased from 50 mN to 1 N; Young's modulus and micro-hardness decrease from 82 to 63 GPa and from 7 to 5,5 GPa, respectively. The average *E* value of 63 GPa obtained at the highest indentation load is in good agreement with the results of macro-mechanical tests given in section 3.3.3 as well as those reported in Ref. [72], whereas indentation-results reported in Ref. [72], were 14 % higher than those reported currently. Such variance might be a result of slightly miscellaneous material (another supplier), different material state (various temperature and time of sintering), as well as different test equipment and calibration procedures.

A micro-hardness value of 5.5 GPa (load of 1N) reported in [26] agrees within the limits of uncertainty with the current data. A decrease of the micro-hardness with increasing indentation load is commonly known as indentation size effect (ISE) [127-129]. The origin of such materials behavior is, however, still under discussion. Several explanations have been suggested: work hardening [130], indentation elastic recovery [131], strain gradient plasticity [132] as well as insufficient sensitivity of load cell [133] and friction between indenter tip and material [134]. However, since both, hardness and Young's modulus decrease, these explanations appear not to be applicable to the current observations. The most likely reason of Young's modulus and hardness decrease with increasing indentation load is the interaction of a larger material volume with the indenter induced deformation zone and to the effect of the local microstructure such as grain boundaries and pores.

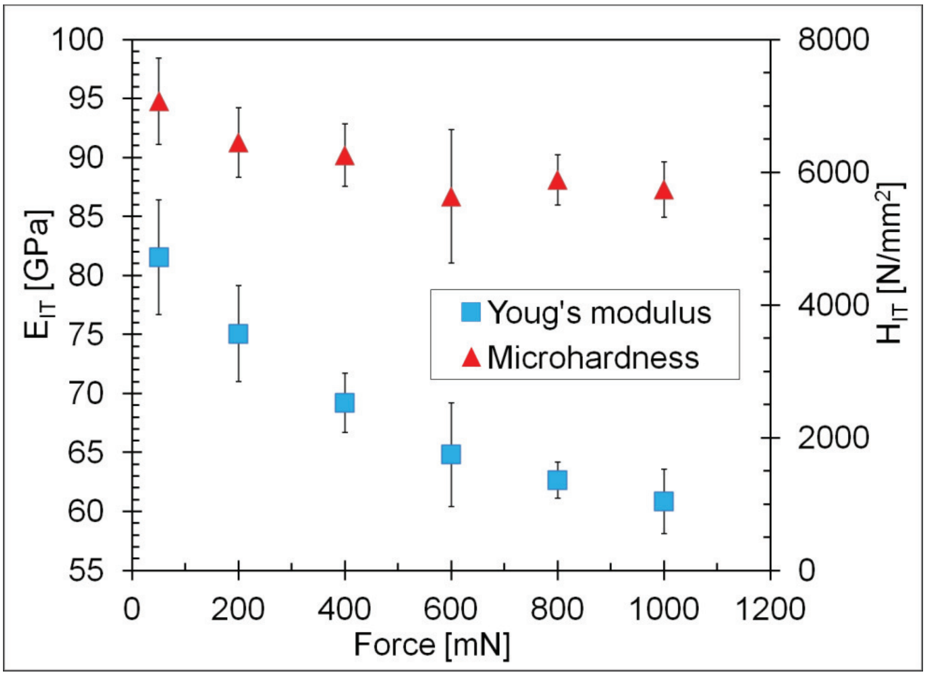

Figure 72. Indentation results: Young's modulus (blue rectangles) and micro-hardness (red triangles).

However, low standard deviation of the results obtained at higher indentation load indicates that the material is rather homogenous.

In order to analyze Young’s modulus and micro-hardness distribution in the BSCF tubes, 10 lines of indentation marks with 20 indents per line with a load of 1 N were positioned in a longitudinal cross-section (Figure 73a). As shown in Figure 73b, both, Young’s modulus and micro-hardness, did not change significantly over the wall thickness and the values oscillated around 62 ± 1 GPa, and 5.6 ± 0.1 GPa, respectively.

Fracture toughness measurements, performed for lines No. 1 and No. 10, yielded results of 0.74 ± 0.024 and 0.71 ± 0.040 MPa·m$^{0.5}$, respectively, which are ~ 25 % lower than the value reported in Ref. [72], where the indentation fracture toughness was calculated from the Anstis equation [115] although the *c* / *a* ratio was smaller than 2.5. In fact, if this relationship is used to calculate the fracture toughness from the current data a value of 0.57 ± 0.026 MPa·m$^{0.5}$ is obtained.

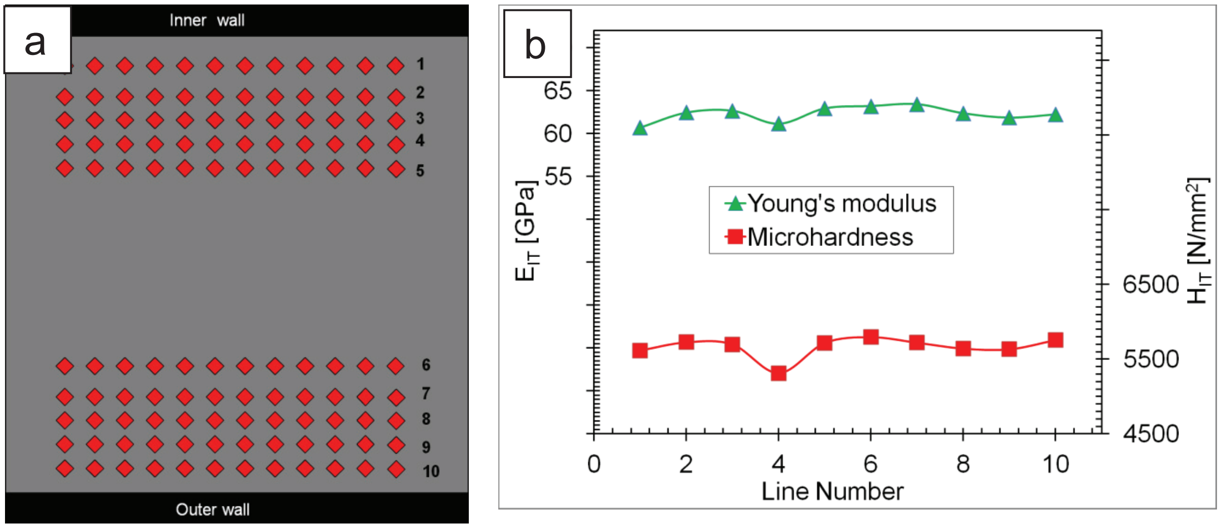

Figure 73. a) Sketch of the indentation array in the longitudinal section of a BSCF tube, b) results of indentation tests in the as-received state

3.3.2. **Fracture stress**

The initial fracture stress determination at RT was based on bending experiments of disc shaped specimens with a diameter of 15 mm and a thickness of 1 and 2 mm, respectively. These data were analyzed using the Weibull approach. Additionally, the temperature dependency of fracture stress was investigated based on specimens with O-ring geometry, with two different widths (4 and 10 mm), machined from the BSCF tubes. To permit a limited statistical analysis, at least three specimens were investigated at elevated temperatures in air and in vacuum.

A loading rate of 100 N / min was chosen in order to minimize eventual influence of stable crack growth on strength [107].

Bending test results obtained for 2 mm thick discs at room temperature with a loading rate of 100 N/min are given in Figure 74.

The Weibull modulus of 9 indicates reflects the variation of the fracture stress (experimental data 72 – 101 MPa). The characteristic strength (for failure probability of 63 %) is 86 MPa. The strength is obviously influenced by the strength-limiting volume flaws (see chapter 3.1.3).

The results of measurements performed on disc shaped specimens with 1mm thickness in air at RT are plotted in Figure 75.

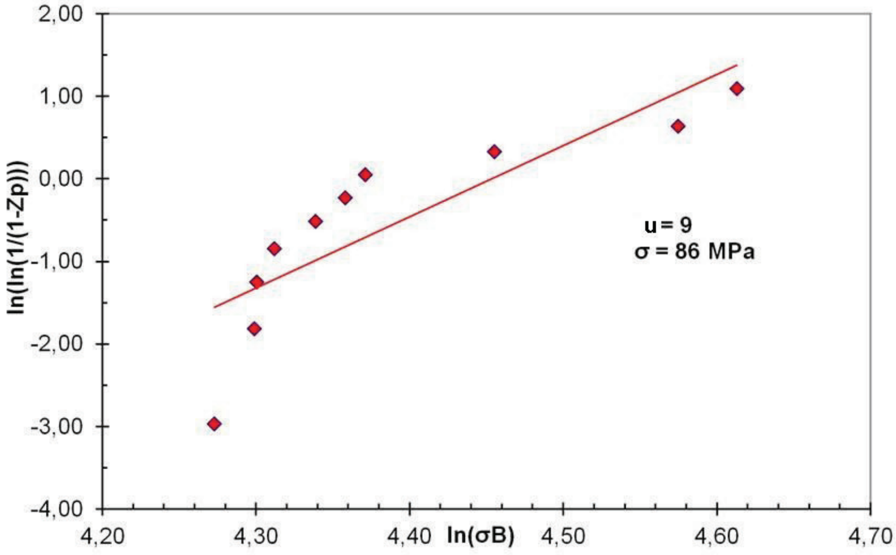

Figure 74. Weibull statistics for discs with 2 mm diameter.

The Weibull modulus as well as the characteristic strength (11 and 90 MPa, respectively) are slightly higher than in the previous case. The results are in good agreement with Ref. [135] according to which the higher probability of strength-limiting large size flaws in specimens with higher volume should lead to a ~ 10 % lower strength for the thicker specimens.

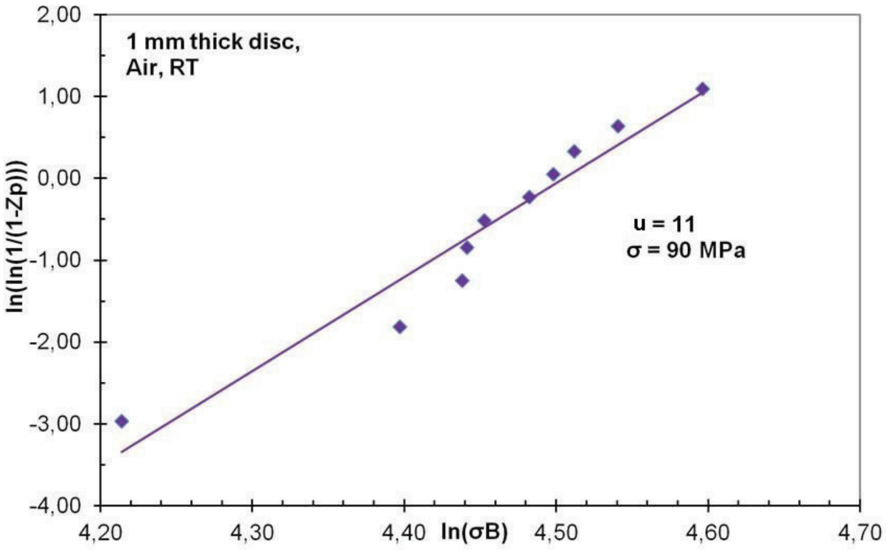

Figure 75. Weibull statistics for discs with 1 mm diameter.

Since the membranes used in the demonstration unit [116] have a tubular shape, fracture tests were also carried out at specimens in O-ring geometry, machined from tubes. Initial measurements were carried out at room temperature on 8 specimens with a width of 4 mm (to fulfill the requirements of the standard) and resulted in a characteristic strength of ~ 143 MPa (Figure 76), probably due to a more homogenous microstructure of tubes and significantly lower amount of strength-limiting flaws in comparison to plates. Additionally, differences in the deformed volume of specimens with different geometries may have an effect on the test results. The surface quality should also be taken into account since the highest stresses arise at the surface.

The Weibull modulus (*u*) was 16, which is a high value even for engineering ceramics. The higher value of *u* indicates that failure stresses had a smaller scatter (measured values 120 – 144 MPa) than in case of discs. Higher strength and Weibull modulus indicate a better quality of the tubular material (in comparison to discs) with significantly smaller amount of large defects (see section 3.1.3).

Results of the measurements at elevated temperature are shown in Figure 77. It was not possible to apply Weibull statistics for results obtained at *T* > 25°C due to limited number of tests, hence only average values are given. The average fracture stress in air and vacuum decreases with increasing temperature and reaches a minimum value of ~ 50 MPa at 200 °C.

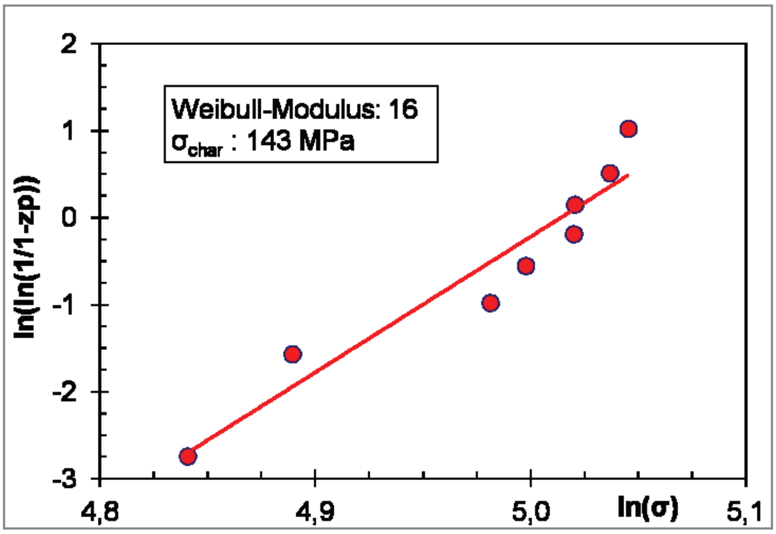

Figure 76. Weibull statistics for O-ring specimens with 4 mm width.

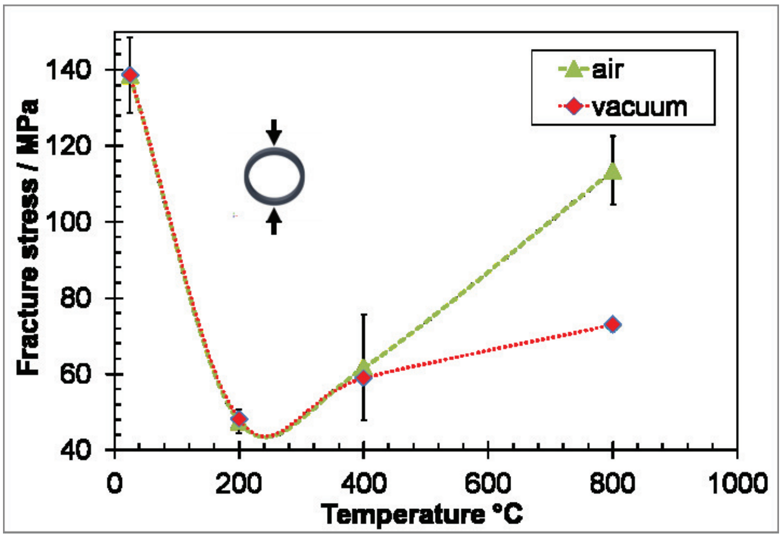

Figure 77. Temperature dependence of fracture stress in air and vacuum.

Further temperature increase results in an increase of the fracture stress to ~ 113 MPa at 800 °C in air and ~ 70 MPa in vacuum. A similar temperature dependence of the fracture stress was reported by Huang et al. for disc-shaped BSCF specimens [72]. However, the fracture stress at RT as well as at 800 °C was 30 % lower than the values given here, which might be a result of different specimen geometries and a different flaw size distribution. Note that the strength value reported by Huang et al. for RT is similar to that obtained for 1 mm thick discs in the present work (Figure 75).

The origin of the rather strong fracture stress decrease at around 200 °C seems to be associated with the spin transition of Co-ions [72, 136]. Magnetic susceptibility measurements reported by Huang et al. [72] (Figure 78) revealed a linear increase of susceptibility with increasing temperature reaching a maximum at about 250 °C. This temperature corresponds very well with the temperature range where the minima of the mechanical properties are observed (Figure 77).

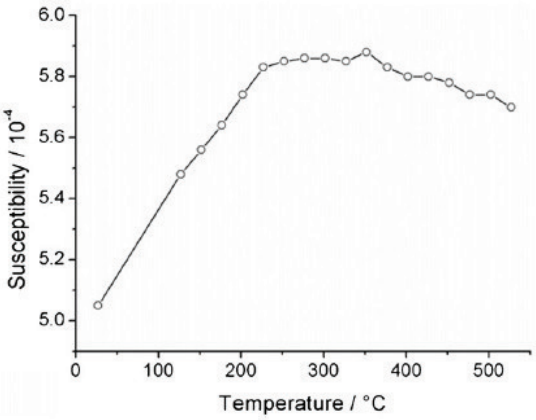

Figure 78. Temperature dependence of the magnetic susceptibility of the BSCF [26].

In the case of tests carried out under vacuum, fracture stress values were similar to the ones obtained in air up to 400 °C. However, at 800 °C a significant difference appears: The fracture stress under vacuum reaches a value of 73 MPa, which is 32 % lower than the value obtained in air. At a first glance, this behavior might be associated with the chemical expansion of BSCF, occurring above 500 °C [27, 37]. Under vacuum, a larger amount of oxygen is released with increasing temperature resulting in a stronger lattice expansion (Figure 16, Figure 17), which is connected with decreasing inter-atomic attraction forces (Figure 14), resulting in a decrease of cohesive strength (Equation 4).

However, temperature dependence of fracture stress and Young's modulus measured in air by Huang [26] shows a similar decrease with increasing temperature only up to 200 °C. Above this temperature, the Young's modulus increases, whereas the average fracture stress further decreases. At around 400 °C, the Young's modulus still decreases slightly, whereas the fracture stress increases strongly. This suggests that additional factors lead to differences in elastic and brittle behavior that might be related to differences in surface and bulk behavior of the material.

Note that the minimum of average fracture stress occurs at 200 - 400 °C, i.e. well below the range where chemical expansion phenomena might be expected.

Using Equation 20, an estimation of the fracture stress of longer membrane tubes (with a characteristic volume V) is possible on the basis of fracture tests performed on smaller specimens in O-ring geometry (with small characteristic volume V_0).

As mentioned in a Chapter 1.1, for a 500 MW power plant, a membrane area of around 140000 m^2 is needed. If one tubular membrane has an area of 0.02 m^2 (length and outer diameter of 0.5 m and 15 mm, respectively), around 7000000 membranes should be used to provide the oxygen demand of the power plant. If it will be assumed, that at room temperature only one tube of a 1 million may fail, according to Equation 20 [135], a stress of 47 MPa should not be exceeded. If the failure probability will be increased 1/100000 the tolerable stress can be increased to 55 MPa.

$$P_S \; V \; = exp \; -\frac{V}{V_0} \; {\frac{\sigma}{\sigma_0}}^{u}$$

Equation 20.

where: *V* – characteristic volume of the component; other parameters were defined in Equation 10. In current case, P_s, V, V_0, σ_0 and u are input data and σ is calculated.

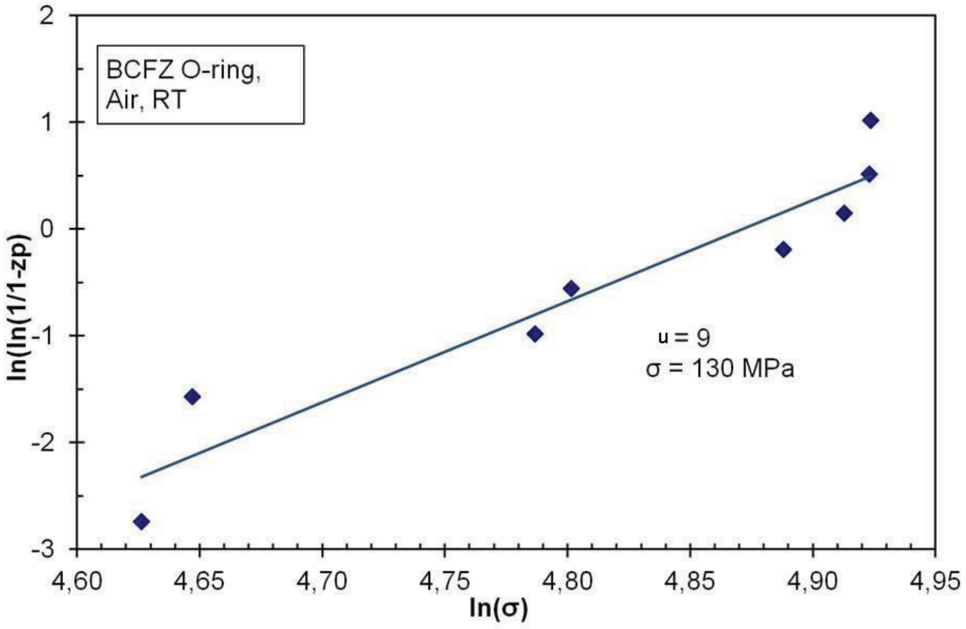

Figure 79. Weibull statistics for the BCFZ 1442 material.

In order to compare BSCF's properties with another membrane materials resulting from the ongoing development and materials improvement, an additional set of measurements on $BaCo_{0.4}Fe_{0.4}Zr_{0.2}O_{3-\delta}$ (BCFZ 1442) specimens, supplied by the IKTS, in O-ring geometry ($Ø_O$ =10 mm, $Ø_I$ = 8 mm, *b* = 10 mm) was performed. Results are given in Figure 79.

As shown in Figure 79, Weibull modulus and strength of the BCFZ 1442 at RT are similar as for the BSCF.

3.3.3. **Young's modulus**

In addition to the indentation tests, the Young's modulus of BSCF was also calculated on the basis of the ring-on-ring and O-ring bending results (chapter 2.3.2). Furthermore, Young's modulus was determined from the stress-strain curves obtained during the loading part of compressive creep tests (chapter 2.6.1). For the BCFZ 1442, investigation was performed only in O-ring geometry. All specimens were tested at selected temperatures in the range RT to 900 °C in a heating sequence. A load-free holding time of 1 hour at constant temperature was introduced before testing to reach thermal equilibrium. Results obtained for the BSCF are shown in Figure 80.

The room temperature Young's modulus of 62 GPa obtained from O-ring test is in good agreement with the values determined form the depth-sensitive indentation tests (section 3.3.1).

The data obtained on the basis of the compression tests show a smaller temperature dependence than those determined from ring-on-ring tests. However, the overall temperature dependence of the results from both methods is similar. It might be suggested that the decrease of Young's modulus at around 200 °C has a similar origin as the decrease of fracture stress in the same temperature regime. A further temperature increase results in an increase of Young's modulus to ~ 50 GPa at 350 °C.

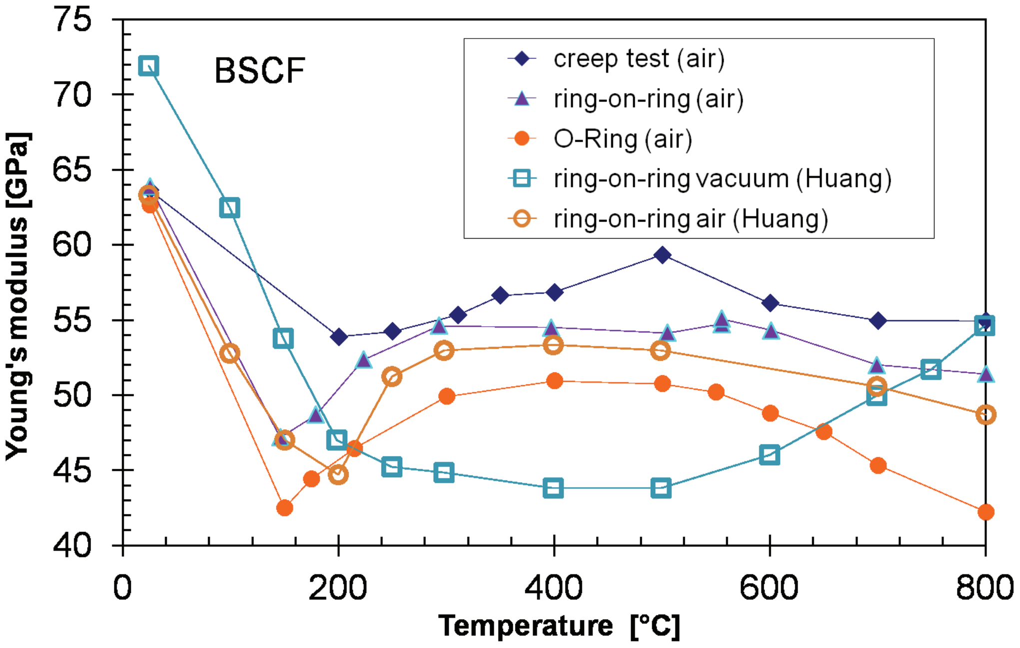

Figure 80. Temperature dependency of Young's modulus obtained in various tests. Data points marked with open symbols are taken from Huang et al. [26].

This value remains rather constant in case of compressive and ring-on-ring tests. This is in good agreement with results obtained using impulse excitation technique (where the applied stresses are rather low) reported by Huang et al. [137]. In the same report Young's modulus is found to be almost constant above about 600 °C.

In the case of O-ring tests, Young's modulus decreases above 500 °C with increasing temperature and reaches a value of ~ 40 GPa at 800 °C. The decrease at higher temperature might be a result of inelastic deformation, which may be enhanced by oxygen release (see chapter 3.5.1). Ring-on-ring data are in excellent agreement with results obtained for air using same method by Huang et al. [26] for BSCF material from another supplier. Results obtained by Huang et al. [26] under vacuum at $T > 500$ °C, showing continuous increase of Young's modulus. It could be possible that hexagonal phase, formed at moderate temperatures in air, compensates the increase of Young's modulus.

Systematic differences between values obtained during compressive creep- and O-ring tests might be a result of differences in Poisson's ratio correction in Equation 12 and Equation 13 or errors in measuring the specimen's deformation, since in compressive tests E is derived directly from the slope of stress-strain curve.

A similar influence of creep on fracture stress determined from O-ring test data is expected, whereas the other effects quoted above will have a smaller influence since the calculation of the stress is only based on the load, not on the rather small deformation (here in the range of 50 µm).

Young's moduli, obtained for the BCFZ 1442 specimens by the O-ring method are presented in Figure 81. The behavior of the BCFZ 1442 tested in air is similar to that expected for engineering ceramics [71]. In comparison to the BSCF, also a decrease of Young's modulus is visible at ~ 200 °C. However, this change is much less pronounced than in the BSCF. Values obtained between 300 - 400°C are higher than in case of the

BSCF. This might be caused by the smaller amount of cobalt in the BCFZ 1442. Measurements above 500 °C are also affected by creep. Under vacuum, a stronger decrease of Young’s modulus at 200 °C than in air was noticed, and it is as pronounced as in case of BSCF. Similar as in air, *E* for BCFZ 1442 keeps rather constant value between 200 and 300 °C. After reaching 300 °C, Young’s modulus decreases monotonously. This is a significant difference to the BSCF, that has been reported by Huang [26] for testing in vacuum. As mentioned earlier, the results of O-ring tests performed at T > 500 °C can be influenced by creep, which is probably the case for the tests presented here.

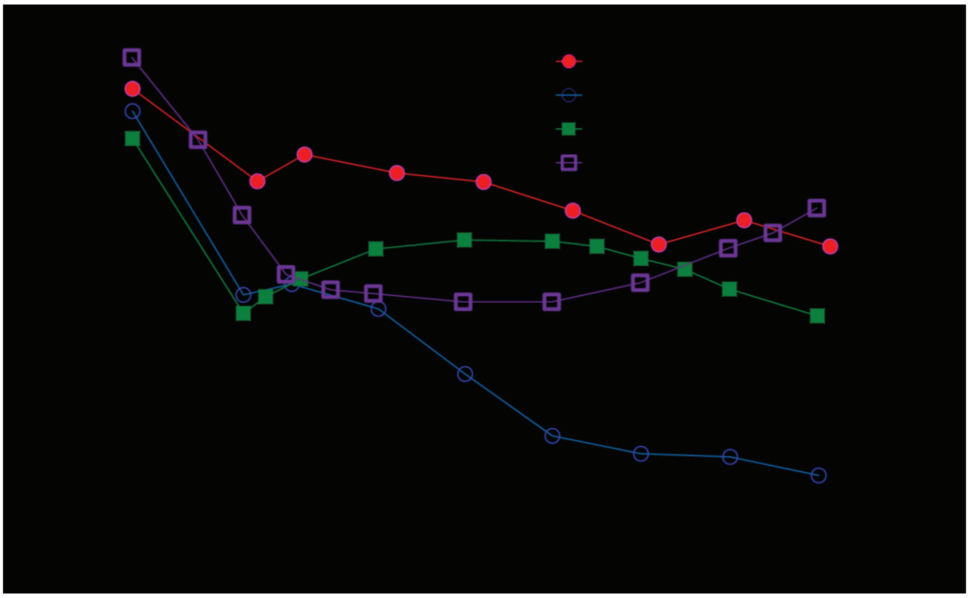

Figure 81. Comparison of Young’s modulus for BSCF 5528 and BCFZ 1442 obtained from O-ring tests. Data represented by open rectangular are obtained by Huang [26] by ring-on-ring method.

3.4. Mechanical properties after thermal treatment

3.4.1. Fracture stress

In order to gain information on the influence of the presence / absence of hexagonal phase on the mechanical properties of the BSCF, fracture stress measurements were performed on specimens after the heat treatments described in section 2.5. The microstructure resulting from these heat treatments is discussed in section 3.2, where the temperature range and oxygen partial pressures resulting in the coexistence of cubic and hexagonal phase are identified. On this basis, two additional types of heat treatment (see section 2.5) resulting in distinctly different microstructure were performed: A first set of specimens (annealed in air at 750 °C for 150 h in air) contained significant amount of the secondary hexagonal phase, whereas the second set (annealed at 950 °C for 24 h under 10^{-2} mbar vacuum) showed a single (cubic) phase microstructure.

The resulting fracture stresses vs. temperature are shown in Figure 82.

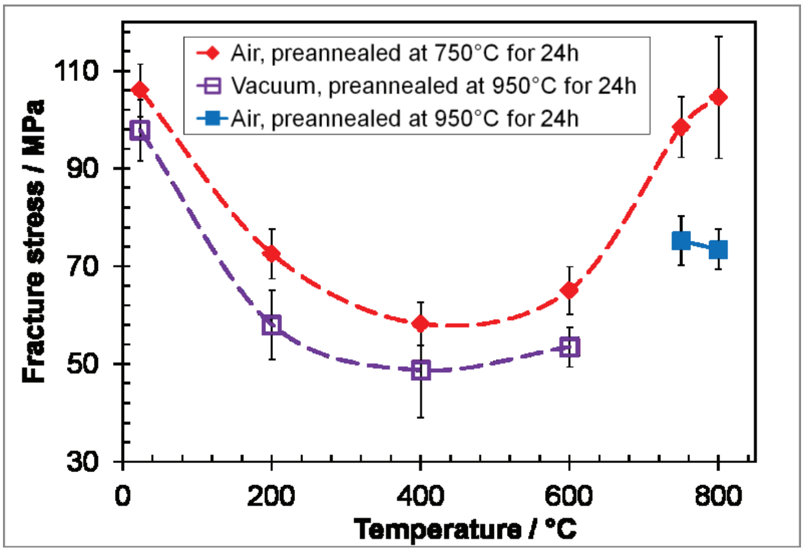

Figure 82. Temperature dependency of the fracture stress of specimens after different thermal treatments.

It is clearly visible that the room temperature fracture stress for annealed specimens is about 30 MPa lower than for as-received specimens (see Figure 77). However, the currently reported results were obtained for specimens with a width of 10 mm, while the O-rings used for the tests described in section 3.3.2 were 2.5 times shorter (b = 4 mm). The decrease of strength, related to the increase of specimen volume, was calculated using Equation 20 to ~ 10 %) Therefore, the additional (~ 10 %) decrease might be related to annealing effects.

Furthermore, the material pre-annealed under vacuum showed lower fracture stresses than that annealed in air. This difference might be caused by different oxygen stoichiometries after annealing under different conditions, which may results in increase of lattice constant and the weakening of inter-atomic bondings. Moreover, the minimum of the fracture stress of pre-annealed samples was observed at 400 °C, whereas tests performed on as-received specimens showed a minimum at 200 °C. This could be a result of stoichiometry changes obtained due to annealing. The slightly increased average value of fracture stress for annealed material in comparison to the as-received one (Figure 77, Figure 82), obtained at 200 °C is within the limits of uncertainty.

The increase of fracture stress at T > 600 °C is surprising. According to Equation 4, the cohesive stress decreases when Young's modulus and / or the interatomic distance increases. Figure 80 indicates a rather constant Young's modulus at temperatures between 600°C and 800°C. At the same time, the interatomic distance increases due to chemical expansion, which should result in decreasing strength. However, the experiments clearly confirm that the strength is increased.

Additional bending tests were performed in air at 750 °C and 800 °C. Before these tests, the specimens were pre-annealed at 950°C for 24 h and directly cooled down to the test temperature in order to avoid hexagonal phase formation. The O-ring tests were performed one hour after reaching the test temperature, which was sufficient to reach thermal equilibrium across the specimens. The results obtained after that test procedure at 800 °C were identical to the results obtained under vacuum at a similar temperatures, which suggests that the fracture stress at temperatures higher than 750 °C was also influenced by the formation of hexagonal phase and not only by the lattice expansion associated with oxygen release. Results of these investigations indicate that at elevated temperatures, fracture stress of BSCF in air, contrary to vacuum, is higher due to strengthening by hexagonal phase presence. However, such influence was not visible below 600 °C.

3.5. Creep tests

3.5.1. Influence of chemical expansion on creep

Before discussing the creep properties of the BSCF, the potential effect of chemical expansion should be addressed. Figure 83 illustrates the time-dependent changes of the dimensions of the BSCF tubular specimens at elevated temperatures. The setup of the experiment was identical that used for compressive creep tests (Figure 31).

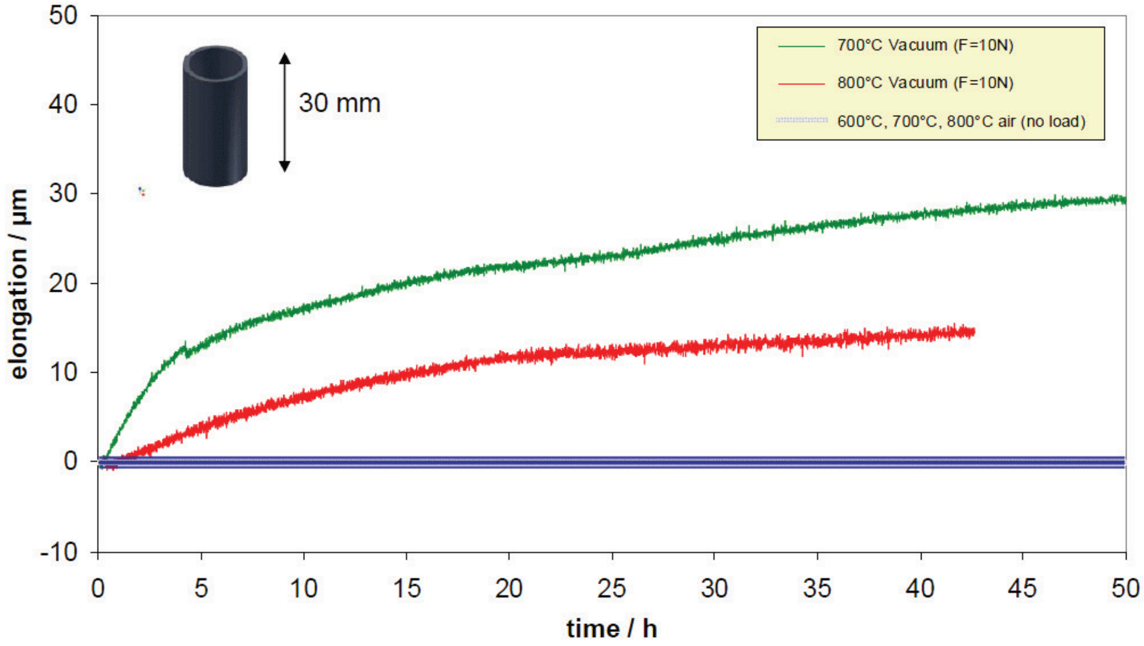

Figure 83.Dimensional changes of the BSCF during dwell at elevated temperatures.

Specimens were heated up to test temperature and the dwell time was ~ 40 h. Subsequently, the specimen elongation induced by chemical expansion was measured. Note that in the vacuum tests (10^{-5} mbar), the specimens were loaded with a rather low load of 10 N, which does not lead to significant creep effects, but assured good contact between specimen and pushing rods. In air no chemical expansion could be observed, hence a standard pre-load of 2 N was used.

Results presented in Figure 83 reveal that in the case of air, no measureable chemical expansion during the dwell time was observed. This means that the entire excess oxygen was continuously released during heating. Oxygen equilibrium is reached very fast due to the high amount of oxygen in the surrounding atmosphere and after heating no further changes in dimensions were noticed. However, in case of vacuum, a continuous change of the specimen dimensions was present even after 40 h at constant temperature (Figure 83). At 700 °C, oxygen release is strong in the initial 10 h. After this period, lower and rather stable changes in dimension can be observed. At 800 °C a steady state is obtained after around 15 h. This demonstrates the very slow and continuous process of oxygen release from the lattice under vacuum.

Furthermore, it is very interesting how the dimensions of the BSCF specimens change during heating. Figure 84 illustrates the influence of the temperature on displacement of a 30 mm tube during temperature increase, both in air and under vacuum. The testing setup is similar as in the case of experiments described above. The heating rate was 1 K/min and a static load of 1400 N, resulting in a stress of 30 MPa was applied. Figure 84 shows the derivatives of strain versus temperature. The change in slope at higher temperatures can be related to creep effects. Therefore, it can be stated that creep of BSCF starts at around 500 °C in air. However under vacuum, this limit is reached already at around 450 °C. This observation agrees very well with TGA measurements (Figure 16) presented by Faraji et al. [16], where identical behavior of mass changes in a similar temperature regime, related to oxygen release was reported. This strongly suggests that vacancies, introduced in the material after oxygen release accelerate creep due to a larger amount of diffusion paths available for cations. In the case of vacuum, the effect of inelastic deformation is stronger than in air (Figure 84) due to higher amount of vacancies created by oxygen release (expected from results presented in Figure 18), which is reflected in the creep behavior, as described in section 3.5.2.

Obviously, chemical expansion will not strongly affect the results of creep measurements in air. However, the chemical expansion might influence the results of creep tests carried out in vacuum. Hence, pre-annealing at 850 °C for 24 h was performed before each test. This seems to be a good compromise since the largest dimension changes occur within first 20-25 h (Figure 83) and the remaining chemical expansion is negligible compared to the creep deformation.

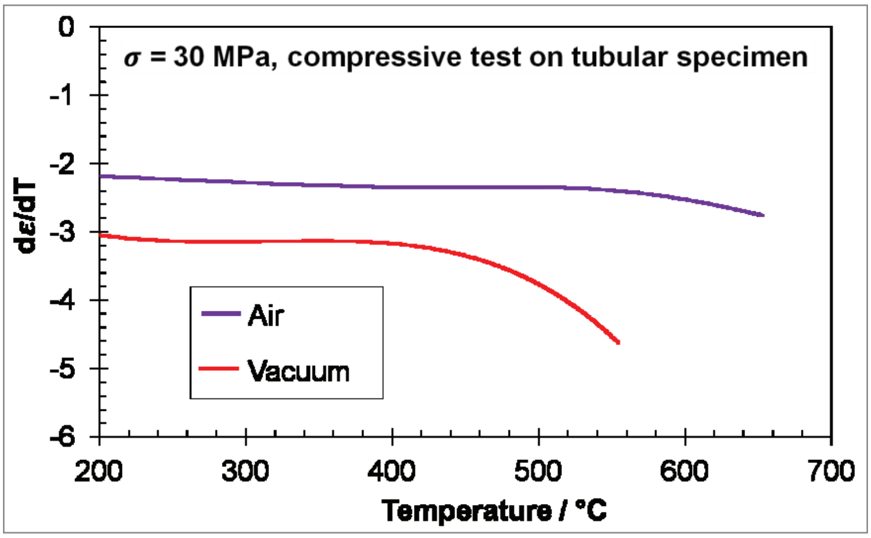

Figure 84. Deformation of the BSCF during heating under constant load.

3.5.2. **Creep characterization**

The steady state creep equation (Equation 7) [100] was used to describe the creep behavior of the BSCF, in particular the dependence on grain size, oxygen partial pressure, stress and temperature. The individual parameters used in Equation 7 were determined in the following way:

The inverse grain size exponent was determined by fitting Equation 7 to an ln($d\varepsilon/dt$) – ln($1/d$) representation (Figure 85) such that the slope of the linear fit represents the value of p. The data necessary to describe grain size influence were taken from the results of creep tests performed in air at a stress of 30 MPa on specimens with standard (29 µm) and increased (88, 140 µm) grain size for temperatures ≥ 850 °C.

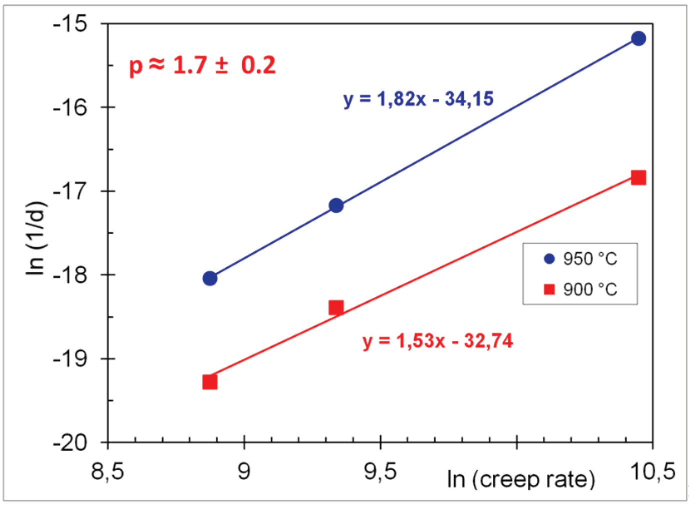

Figure 85. Identification of grain size exponent in Equation 7.

The oxygen partial pressure dependence described by the exponent m as well as the stress exponent n were determined using a similar approach, in particular plotting the experimental data in representations ln($d\varepsilon/dt$) vs. ln(pO_2) and ln($d\varepsilon/dt$) vs. lnσ, respectively (Figure 86, Figure 87) and subsequent linear fitting.

A significant spread of temperature on stress exponent n is seen in Figure 87. However, for reasons of practical applicability, one single value of this parameter should be used in the creep equation (Equation 7). Hence, an average value of n = 1.7 was used for further calculations.

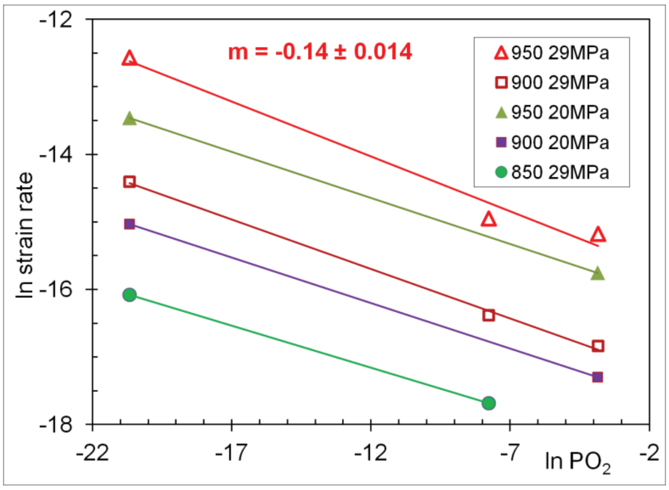

Figure 86. Identification of oxygen partial pressure exponent.

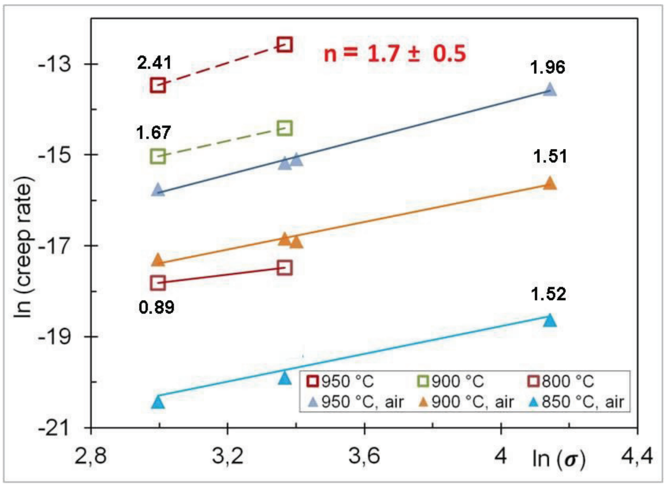

Figure 87. Identification of stress exponent for air and vacuum.

The last major parameter to be determined in (Equation 7) is the activation energy E_a indicating the influence of temperature on creep rate. To identify E_a the creep results were plotted in the representation ln ($d\varepsilon/dt$) vs. $1000/T$ and fitted linearly (Figure 88).

The activation energy is then calculated by multiplication of the slope from linear regression with the universal gas constant R.

In Figure 89, creep rates vs. temperature are plotted for specimens with different grain sizes.

The data points are directly obtained from experiments according to the procedure described in chapter 2.6.1 while the lines represent the results calculated (Equation 7) using the parameters determined according to the procedure described above.

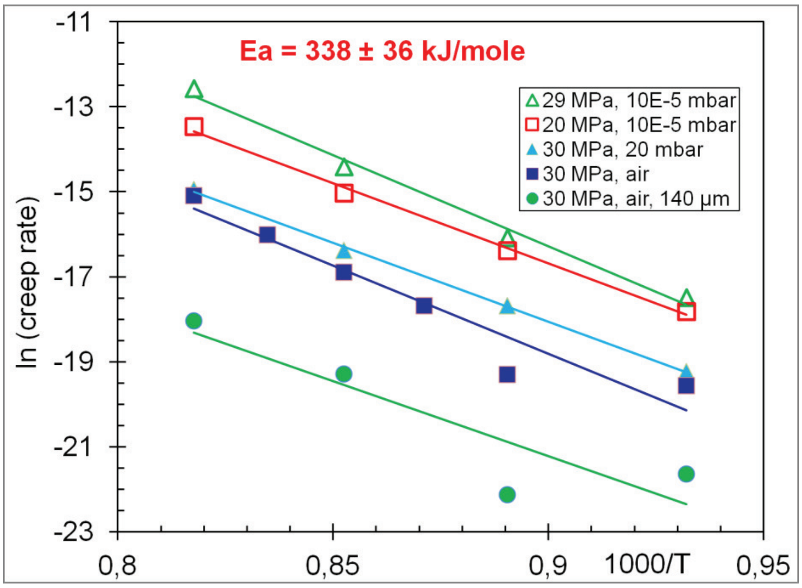

Figure 88. Identification of activation energy for creep.

The fitted lines are in good agreement with the experimental results. As expected, creep rates decrease when the grain size is increased. In order to reduce the creep rate, the grain size should be as large as possible. Note that results for grain sizes of 29, 88, 140 µm were obtained from IKTS tubular specimens, whereas results for grain size of 4.6 µm were acquired using cylinders supplied by VITO, Belgium.

Experimental data of the creep rate versus temperature for various applied stresses are presented in Figure 90.

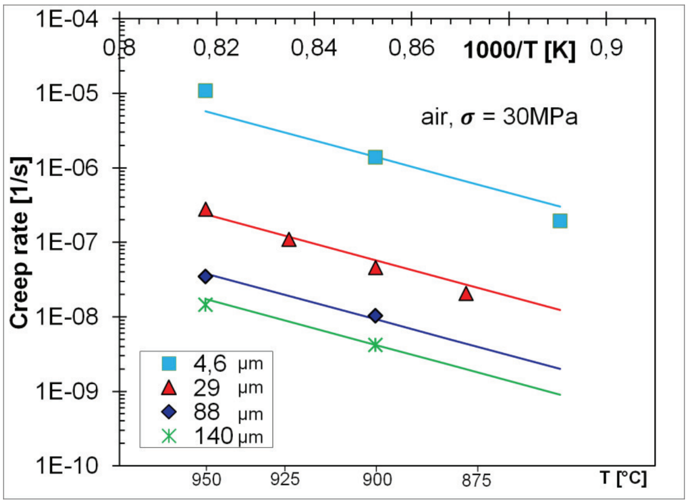

Figure 89. Temperature dependency of creep rate, obtained under a constant stress of 30 MPa for specimens with different grain size.

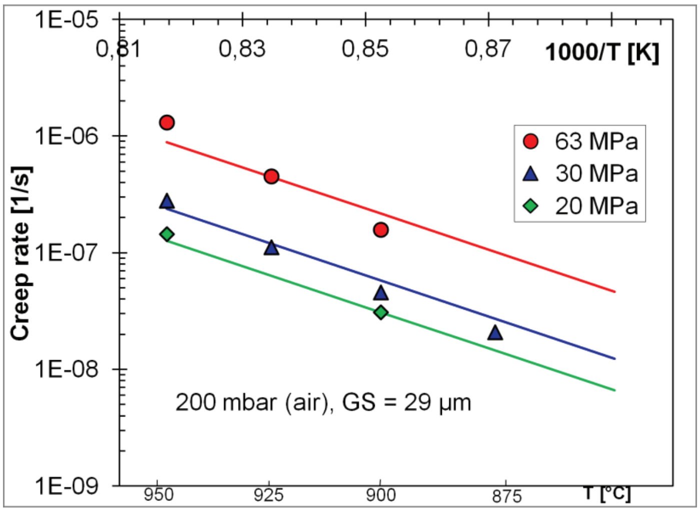

Figure 90. Temperature dependence of the creep rate obtained for specimens with grain size of 29 µm for different stresses in the range of 20 to 63 MPa.

Experiments were performed in air using three different compressive stresses (20, 30 and 63 MPa). The calculated lines from Equation 7 are in very good agreement with the experimental results, if an average stress exponent *n* of 1.7 is used. However, the slope of experimental data for a stress of 63 MPa is steeper than the calculated one. This difference is a result of using an average activation energy for the calculations, which was necessary in order to describe the overall complex behavior by Equation 7 using only one set of parameters.

Furthermore, it is necessary to take into consideration that the membranes will operate under different environments (for example feed side under air and sweep side under vacuum). Hence, the influence of oxygen partial pressure on the creep behavior has to be known for design and operation of reliable components. To obtain this information, an additional set of experiments with reduced oxygen partial pressure was performed. Results are shown in Figure 91 and in Table 11.

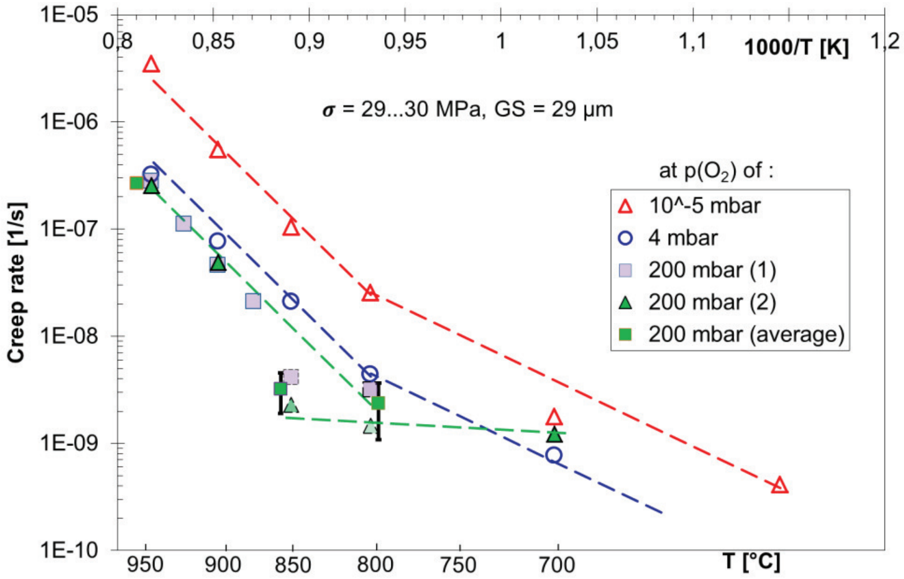

Figure 91. Temperature dependency of creep rate for one particular constant stress and grain size. The oxygen partial pressure was varied.

At first glance, a smooth transition in the slope of the Arrhenius plot for tests performed at oxygen partial pressures of 4 mbar and 10^{-5} mbar is visible at 800 °C, which corresponds to a change of activation energy from 164 ± 16 to 338 ± 36 kJ/mol. However, in the case of air, the strong increase in creep rate can be seen at a slightly higher temperature of around 850 °C. This temperature shift is most likely a result of hexagonal phase presence in microstructure (see section 3.2.1) and will be discussed later in the current chapter.

Table 11. Creep rates (s^{-1}) obtained during the current study.

Stress [MPa]	pO_2	Grain size [μm]	heating	creep rates [s^{-1}] obtained at the temperature of:				
	[mbar]		cooling	750 °C	800 °C	850 °C	900 °C	950 °C
20	200	29	heating	-	$1.50\cdot10^{-9}$	$1.34\cdot10^{-9}$	$3.08\cdot10^{-8}$	$1.44\cdot10^{-7}$
29	200	29	heating	-	$1.46\cdot10^{-9}$	$2.29\cdot10^{-9}$	$4.88\cdot10^{-8}$	$2.57\cdot10^{-7}$
20	10^{-5}	29	heating	-	$1.83\cdot10^{-8}$	$7.67\cdot10^{-8}$	$2.97\cdot10^{-7}$	$1.42\cdot10^{-6}$
29	10^{-5}	29	heating	-	$2.55\cdot10^{-8}$	$1.04\cdot10^{-7}$	$5.53\cdot10^{-7}$	$3.48\cdot10^{-6}$
63	200	29	heating	$4.14\cdot10^{-9}$	-	$9.14\cdot10^{-9}$	-	$9.91\cdot10^{-7}$
63	200	29	cooling	$1.81\cdot10^{-9}$	$5.22\cdot10^{-9}$	$4.60\cdot10^{-8}$	-	$9.91\cdot10^{-7}$
30	200	140	heating	-	$4.02\cdot10^{-10}$	$2.47\cdot10^{-10}$	$4.23\cdot10^{-9}$	$1.46\cdot10^{-8}$
3	200	88	heating	-	$1.44\cdot10^{-9}$	$1.17\cdot10^{-9}$	$1.03\cdot10^{-8}$	$3.50\cdot10^{-8}$
30	4	29	heating	-	-	$2.09\cdot10^{-8}$	$7.66\cdot10^{-8}$	$3.21\cdot10^{-7}$

Below 850 °C, the creep rate is rather independent of the temperature, and the corresponding activation energy is only ~ 60 kJ/mol for air. Above 850 °C, a strong increase of the creep rate with decreasing $1/T$ is visible. The corresponding activation energy takes a value of ~ 340 kJ/mol, which is similar to that obtained in vacuum for the same temperature range. Note that the uncertainty of the measured creep rates in the low temperature range (below 850 °C) is significant. Despite that, average value of creep rate obtained for 800 °C in air is lying on the line calculated using Equation 7. Uncertainty above 850 °C is rather small (results of two experiments for air at 950 °C fit very well each other)). Note that Secondary Ion Mass Spectrometry (SIMS) investigation on the diffusion of Mn and La cations in the BSCF 5528 performed in laboratory air, reported in the MEM-BRAIN project by Schröder [138], reveal that in a temperature range from 850 to 1010 °C, both, bulk diffusion and grain boundary diffusion are present. In their experiments a LSCF layer was deposited onto the BSCF and inter-diffused. Bulk and GB diffusivities differed by about 3-4 orders of magnitude (e.g. at 850 °C, $D(B)_{Mn} = 4\cdot10^{-15}$ whereas $D(GB)_{Mn} = 2\cdot10^{-12}$ cm^2s^{-1}). Activation energies for bulk diffusion of Mn and La cations were measured to 1eV (~ 100 kJ/mol), which is significantly lower than the activation energy for high temperature creep obtained in the present work.

Special consideration was also given to the creep test performed at 850 °C in air (Figure 91), where hexagonal phase should be present (see section 3.2.1). Obviously the creep rate of $9\cdot10^{-8}$ s^{-1} measured under these conditions is significantly lower than the value predicted by the creep equation with the average fitting parameters at T = 850°C. Additional information to explain this anomaly in creep behavior was obtained on the basis of a creep test performed in air under a stress of 63 MPa. The testing procedure for this experiment was modified by additional measurements of the creep rate during the cooling sequence. The temperature – load sequence of this modified creep test is illustrated in Figure 33. This test sequence revealed a difference in the creep behavior of BSCF measured during the heating and cooling sequence, respectively.

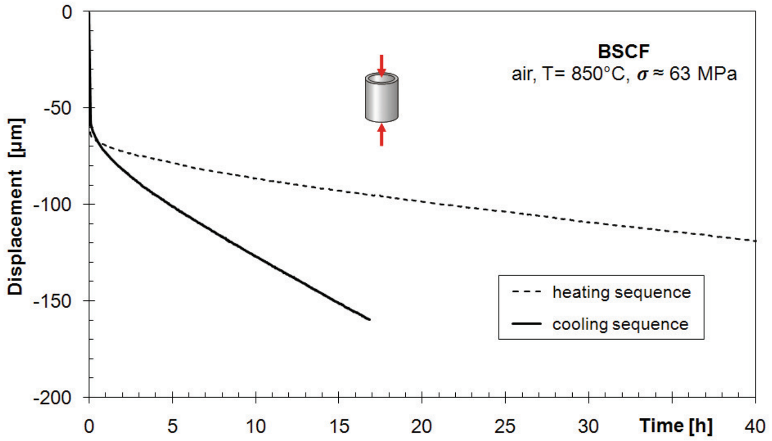

Figure 92. Time - displacement curves obtained during the tests at 850 °C during a heating and cooling sequence. The deformation obtained during cooling is much larger.

This is illustrated exemplarily in Figure 92 showing the displacement - time curves obtained at 850 °C, both during the heating and the cooling sequence.

In the cooling sequence much higher creep rates are observed than in the heating sequence. A creep strain of 0.2 % was obtained after 50 h at 850°C during heating, whereas a similar strain was obtained after only 10 h at the same temperature during the cooling sequence, i.e. the creep rate is 5 times higher. Of course, this significant difference needs to be taken into consideration in design and operation.

The slopes of the curves in Figure 93 give comprehensive information on the measured creep rates. The creep rate hysteresis effect becomes clearly visible in $(d\varepsilon/dt)$ vs $(1/T)$ plot (Figure 93).

In the heating sequence two regimes can be distinguished. First, for the temperature range between 750 and 850 °C an activation energy of ~ 80 kJ/mol was determined. This is about 30 % higher than the value obtained for the creep tests under 30 MPa. A possible reason of such behavior is explained later in the current section. A second regime starts when the temperature exceeds 850 °C with a stronger temperature dependence of the creep rate. This region corresponds to an activation energy of ~ 580 kJ/mol. Such high E_a is caused by hexagonal phase presence because at around 850 °C, values of creep in air are lower than extrapolated from the measurements at higher temperature, causing much steeper slope. Contrary to the heating sequence, only one regime with an activation energy of 345 kJ/mol could be observed for the cooling sequence. The largest difference in the creep rates measured in air for cooling and heating sequences occurs at 850 °C, which appears to be a key temperature for the understanding the creep properties of BSCF under this condition.

The anomaly in the creep behavior illustrated in Figure 91 (850 °C, $9 \cdot 10^{-8}$ s^{-1} for air), as well as the hysteresis effect shown in Figure 93 can be explained as follows. In Figure 53 different BSCF microstructures are presented. Lower creep rates than calculated at 850 °C in the heating sequence are caused by the presence of the hexagonal phase (Figure 53a). This phase is created very fast at 750 °C. In fact, this is the temperature where the first creep measurement was performed in the heating sequence. When heating up to 850 °C the hexagonal phase cannot be dissolved anymore due to sluggish transformation kinetics proven by the annealing experiment (Figure 53a). Note that under equilibrium conditions, the hexagonal phase would not exist at this temperature (Figure 51c). Along with the further heating and subsequent testing at 900 °C and 950 °C the hexagonal phase dissolves first partially (at 900 °C) and then completely (950 °C), the creep rates determined during the cooling sequence, do not overlap with the respective values obtained in the heating sequence due to differences in the amount of the hexagonal phase (Figure 53b). During the tests performed at 850 °C in the cooling sequence, the material is in a state close to its single-cubic-phase equilibrium condition.

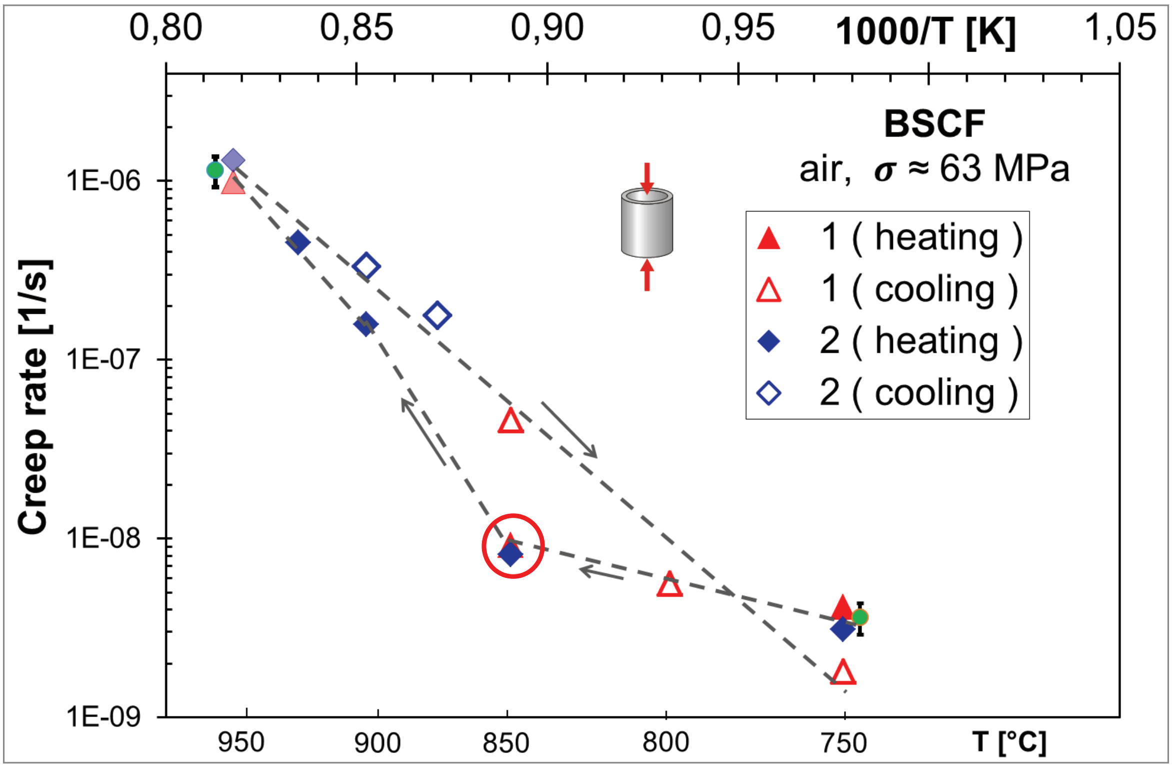

Figure 93. Creep results for test according to the temperature history shown in Figure 33.

The absence of the hexagonal phase in the tested material restores the creep rate to its expected value. It might be concluded that the presence of hexagonal phase in the temperature range from 850 to 880 °C in air can hinder creep by blocking of the grain boundary diffusion paths.

This explanation is illustrated in Figure 94, where every stage of creep test, leading to the hysteresis effect is described.

Recently, Yi et al. [99] reported creep experiments at BSCF cylinders in the temperature range from 805 to 935 °C with creep stresses from 5 to 20 MPa. Various specimens with average grain sizes from 2.5 to 17.4 μm were investigated. Due to the significant difference in the grain size between the latter material and the one investigated in present study, the results can be compared only indirectly. Hence, the creep rates determined for specimens with the grain size equal to 29 μm were recalculated with the aid of the steady state creep equation (Equation 7) into the creep rates which would be obtained for the material with d = 6.9 μm (one of the values used in [99]). Results of these calculations (solid lines), as well as creep rates published in [99] (solid points), are presented in Figure 95.

The recalculated values agree within the experimental uncertainty well with the values reported by Yi et al. [99]. Especially, a significant change in the creep rate at around 880 °C was also noticed by these authors. This phenomenon was assumed to be related with cubic phase instability [99].

However, one difference in the experimental approach between the current studies and these of Yi et al. [99] should be noticed when comparing the respective results. In case of the current work, measurements were performed under constant load and the temperature was varied. In case of Yi et al. experiments, the creep tests were performed at constant temperature and the creep stress was varied.

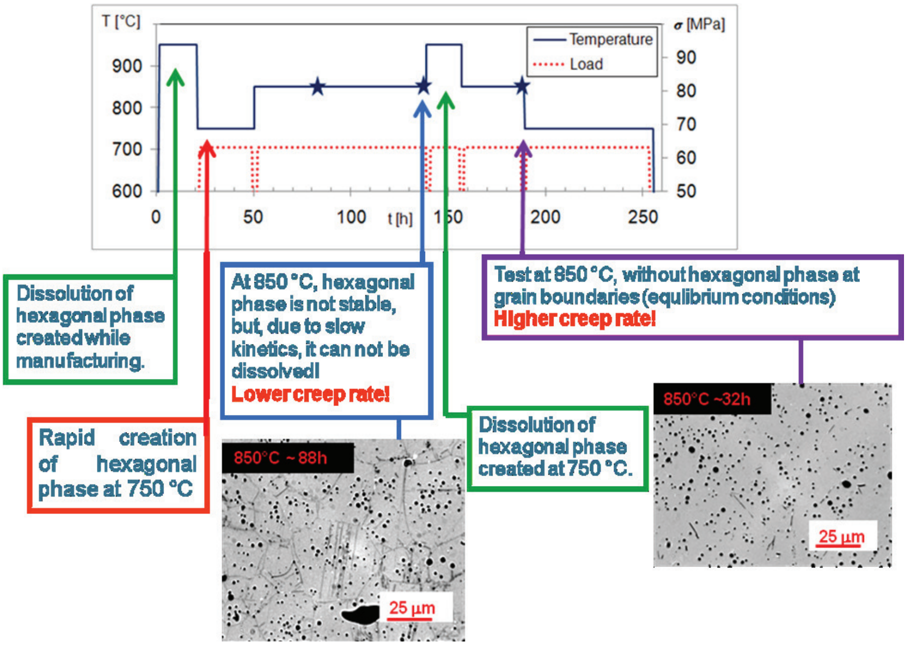

Figure 94. Explanation of hysteresis in creep behavior.

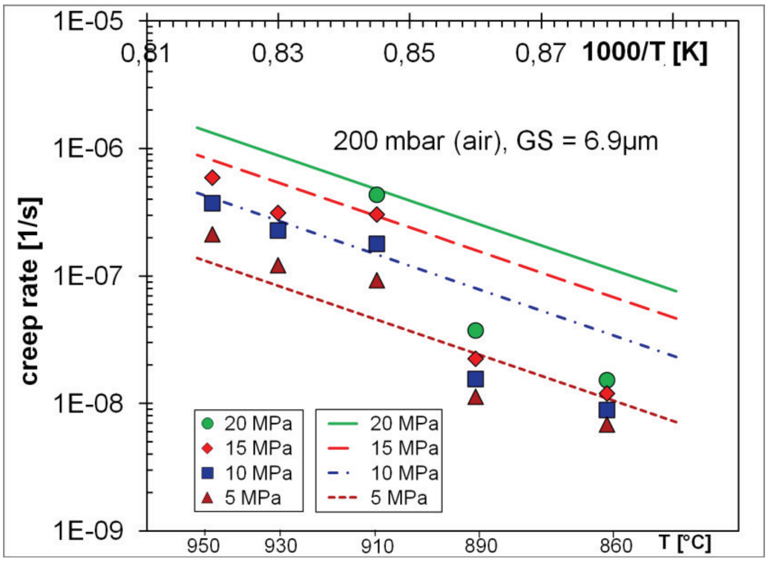

Figure 95. Comparison of creep rates for BSCF specimens with a grain size of 6.9 µm, obtained by Yi et al. [99] (data points) with the creep rates of BSCF obtained in the current work (lines), re-calculated to a grain size of 6.9 µm using Equation 7.

Due to complicated phase transition kinetics, as described in paragraph 3.2.1 and supported by results presented by Niedrig et al. [55], it can be concluded that the difference between the creep behavior in Yi et al. and the current experiments originates from the different thermal history of the investigated samples (initial state as well different experimental approach of the performed creep tests [139]).

In order to verify this hypothesis, additional tests on cylindrical BSCF specimens, supplied by authors of [99] were conducted. Tests were performed in heating sequence under following temperatures: 750, 800, 850, 875, 900, 925, 950 °C. Pre-annealing at 850 °C for 3 h was also applied. Creep stresses of 20 and 100 MPa were used. The results are presented in Figure 96. Blue dots are results from literature [99] at 20 MPa, whereas the red triangles were obtained in the present work under similar load. Basically, the results are compatible, however different transition temperatures were observed (850 °C in the current work and 880 - 890 °C by Yi et al. [99] ($1000/T = 0.85$ on Figure 96)) which was caused by different test approach (and slow dissolution of hexagonal phase during the tests below 880 °C). Nevertheless, the tests reported in Ref. [99] were also performed far from cubic equilibrium conditions.

The lack of compliance between data calculated from Equation 7 and data points reported in Ref. [99] below 910°C (see Figure 95) can be associated with a simple reason. The lines in Figure 95 are calculated for the case where no hexagonal phase is present in microstructure. This is the case under low oxygen partial pressure conditions (20, 10^{-5} mbar) or in air but only when tests are conducted during cooling sequence. During the heating sequence described here, and also during the procedure used in [99] this calculations are invalid due to the two phase microstructure of the BSCF. Open rectangular data points in Figure 96 represent results from a test performed at constant temperature (900 °C) with increasing load (similar to the procedure used in Ref. [99]). As it is well visible, creep data obtained for 10 and 20 MPa are close to the results obtained in the present work at 900 °C and constant load during heating sequence (triangles in Figure 96). Hence, it is very difficult to decide which approach (presented here or in Ref. [99]) is more accurate.

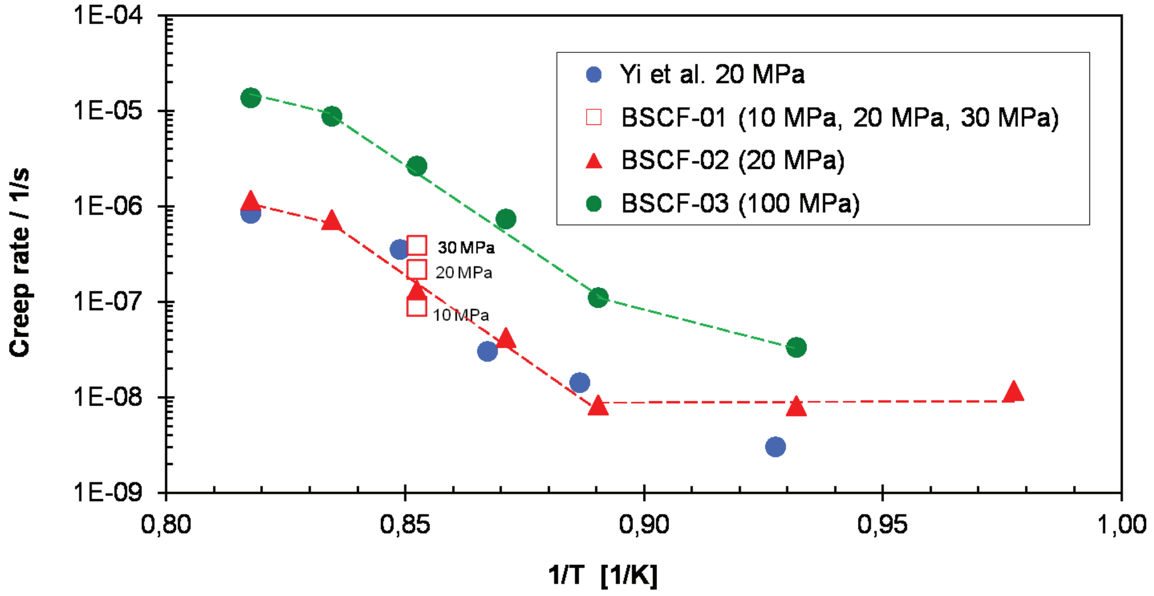

Figure 96. Comparison of creep tests performed in house on specimens supplied by the authors of [99].

As already stated above (Figure 91), the hexagonal phase presence at 850 °C in air caused lower creep rates than predicted by Equation 7. A similar effect can be observed in Figure 95. However, the different test procedure in [99] resulted in an experimental artifact due to sluggish kinetics of hexagonal phase dissolution and led to a shift of the transition to a higher temperature. If before tests at 860 and 890 °C specimens would be annealed for a time long enough to dissolve the hexagonal phase the creep rate should be higher than that obtained without annealing (with two phase structure). Dissolution of the hexagonal phase is very slow in the temperature range 850 – 880 °C. A heating sequence between 825 °C and 890 °C with smaller temperature intervals could confirm this artifact. Additionally, results of tests performed during cooling at 20 MPa (Figure 96) should then follow the green line in Figure 95.

Note that in Figure 96, slight differences in the low temperature regime (on the right hand side of 1000/*T* of 0.9) are well visible. In case of experiments performed in the present work, the creep rate in this region takes almost constant values (region of high uncertainty – see Figure 91). However in the data presented by Yi et al. [99], when a stress of 100 MPa is applied, the result at 800 °C (1000/T of 0.93) is lower than it might be expected according to the results obtained in the present work at 20 MPa. This might suggest that the deformation at such low stresses at temperatures below 800 °C is too low (0.33 μm/h at 800 °C) to obtain reliable results (precision of the displacement sensor is 1 μm) and the measured creep rates could be affected by drift of the creep test equipment and in addition by hexagonal phase presence. When the stress is increased to 60 or 100 MPa, creep rates can be determined correctly due to the larger deformation. This is the most reasonable explanation, why in air in the low temperature regime, the activation energy increases from 60 to 80 kJ/mol when the load is increased from 30 MPa (Figure 91) to 63 MPa (Figure 93). An additional reason can be seen in the different thermal history as well as in uncertainties of the test that might be related to specimen imperfections (roughness, shape).

The stress exponent (n), determined in air by the procedure described at the beginning of the current chapter, is changing insignificantly with temperature (see Figure 87). This suggests that the creep mechanism is independent of temperature, similar like in case of LSCF reported by Huang et al. [104], where a theory of new vacancies creation at high temperatures (causing increase of activation energy when the low temperature regime is exceeded) is proposed. It seems that this theory might also explain the creep behavior of BSCF in air. However, this theory is not applicable for creep of BSCF in vacuum, due to continuous change of stress exponent. In this case, n varies from 0.8 to 2.4 when temperature is increased from 850 to 950 °C (see Figure 87), reflecting continuous changes in creep mechanism. This indicates that even dislocation creep ($n \sim 3$) cannot be excluded at 950 °C. The value of $n = 0.8$ obtained for the range below 850 °C indicates a purely diffusion related process.

Results obtained by Schröder [138] in air, confirms the coexistence of grain boundary and bulk diffusion in this temperature range. Note that the grain boundary diffusion coefficient of Mn in the BSCF was 3-4 times larger than the bulk diffusion coefficient

[138]. Similar results might be expected for all cation diffusion processes in BSCF based compounds.

The coexistence of creep mechanisms other than diffusion is indicated by *n* values significantly higher than 1. In case of negligible diffusion, grains should not grow and maintain their aspect ratio during creep. Some indications of grain boundary widening were found (Figure 60a, Figure 61). However, this finding does not give sufficient evidence for the presence of GBS mechanism during creep of the BSCF in the investigated temperature and load regime. According to the grain size exponent of p = 1.7 obtained for temperatures above 850 °C, the process should rather be governed by bulk diffusion. However, Schröder [138] verified that lattice and grain boundary diffusion coexist even at 1010 °C. Hence, the value of p = 2.45 reported by Yi et al. [99] seems to correspond better to the expectation for this mechanism. The activation energy indicates cations as diffusing species (since the activation energy for oxygen ion diffusion is lower than 60 kJ/mol [34].

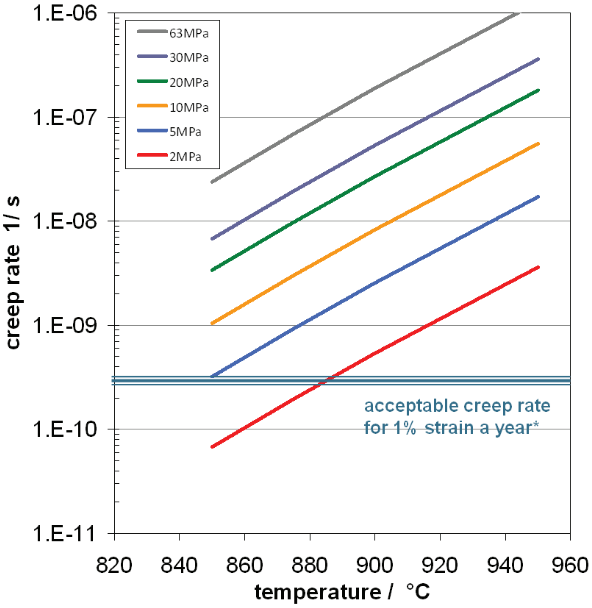

Figure 97. Results of calculations using Equation 7, illustrating under which applied stresses the tolerable creep strain of 1 % per year [98] is exceeded.

According to [98], a creep strain of 1% per year is tolerable for membrane application. On the basis of the creep test data, the stress per year can be calculated (using Equation 7) yielding the data presented in Figure 97. A stress of 2 MPa applied for one year at 880 °C for material with a grain size of 29 µm will result in 1 % of strain. At 850 °C a stress of 5 MPa could be tolerated for the same strain limit, whereas stress of 10 MPa is acceptable only up to 820 °C.

Note that for BSCF with a grain size ~ 7 µm, tested under compressive stress of 5 MPa, a creep rate of ~ $6.9 \cdot 10^{-9}$ 1/s at 860 °C was reported [99]. This would lead to a creep strain of ~ 20 % after one year of operation, which is of course not acceptable for application and underlines the necessity to find a reasonable compromise between sufficient permeation and acceptable creep deformation by further material development and optimization of operation parameters. This issue can be illustrated on the example of operating conditions given in Ref. [25] where an increased air pressure of 17 bar acts on the outer wall of the tube and atmospheric conditions are maintained at the inner side of the tube (feed to sweep side pressure ratio of 17). In this case, according to [140]:

$$\sigma_j = \frac{s \cdot g}{k}$$

Equation 21.

where: σ_j - stress, s – difference between inner and outer pressure, g – radius of tube, k – wall thickness,

The compressive stress generated in the tube walls will reach a value of ~ 6 MPa. If a period of one year is considered, such stress will generate a strain below 1 % in case of the BSCF with a grain size of ~ 26 µm, whereas for the BSCF material investigated in Ref. [99] (d ~ 7 µm), a strain of >7 % will occur, which excludes fine grained BSCF from application in such conditions. This shows the importance of creep investigations for material optimization and process design. Note that temperature along the tube should be constant. Any temperature gradients along the tube will lead to non uniform deformation possibly decrease the time to failure.

In Figure 98 a comparison of creep properties of the BSCF 5582 and the BCFZ 1442 is shown. The well visible kink for the BSCF at 850 °C (1000/*T* ~ 0.89) is absent in case of the BCFZ 1442. Hence, the behavior in air is similar to that observed in vacuum. This may suggest that contrary to the BSCF, the cubic structure of the BCFZ is stable under all applied test conditions (no hexagonal phase formation), which may result in no hysteresis in creep during cooling.

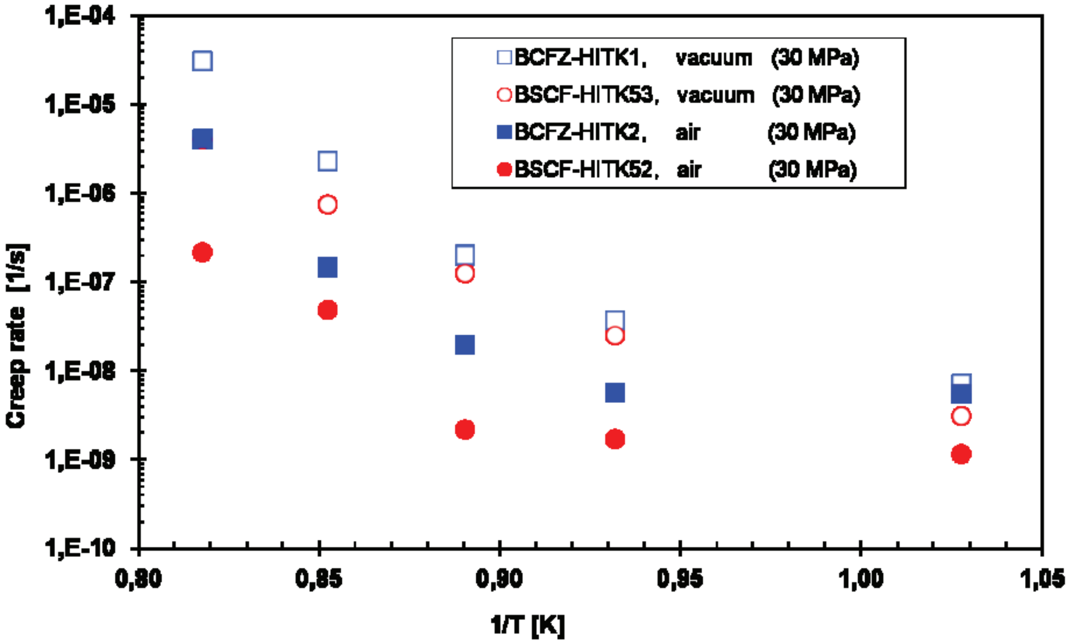

Figure 98. Creep rate comparison for the BSCF 5582 and the BCFZ 1442.

3.6. Post operation analysis of damaged tube

In the demonstration unit shown in section 2.7 [116] mechanical failure of tubes after operation occurred several times. Figure 99 shows a damaged tube after operation during a leakage test performed by R. Kriegel and I. Voigt (IKTS Hermsdorf) [116].This raised questions on the mechanical properties and microstructure (which reflects the local temperature) of the tubes after operation. Therefore, in addition to a mechanical characterization the temperature profile along the length of the tube operated in demonstration unit was determined on the basis of the microstructural investigations conducted after complementary annealing performed in the temperature range from 750 – 950°C (see section 3.2.1).

Figure 99. BSCF membrane tube fractured after operation during leakage test [courtesy of Voigt and Kriegel, IKTS].

Microstructural investigations followed the micro-mechanical tests using indentation and the macro-mechanical bending tests carried out in O-ring geometry. Young's modulus and fracture stress of particular tube segments were determined. In order to conduct the tests, O-ring specimens of 10 mm width were machined from the tubes using a diamond saw. Figure 100 shows one of the investigated demonstrator tubes after the sectioning process.

Figure 100. One of tube after operation sectioned in 10 mm width O-rings.

3.6.1. **Mechanical properties of selected tube segments at RT (depth sensitive indentation)**

Fracture stresses and Young's moduli determined in O-ring geometry showed a large scatter that was probably related to specimen preparation effects, i.e. embedding and cutting, but also to local thickness variations that have not been observed for the material reported in the previous sections. For this reason, the results did not permit any interpretation with respect to the mechanical behavior or possible changes due to the operation. Hence, in order to get insight to the influence of the operation on the mechanical properties of the BSCF tubes tested in demonstrator unit, depth-sensitive indentation measurements were performed. The tube wall cross section was divided into 10 sub-layers (Figure 73a), similarly as in case of the as received specimens (see section 3.3.1). A set of indentation measurements was performed on the sub-layers 1 to 5 (close to inner tube surface, i.e. sweep side) and 6 to 10 (close to outer tube surface, i.e. feed side). The approach allowed to assess possible dependencies of Young's modulus and micro-hardness on the relative position across the tube wall thickness.

Results of the Young's modulus measurements performed with a load of 1 N for a tube section exposed to a temperature close to 750 °C are shown in Figure 101. Young's modulus decreased significantly with increasing distance of the measurement position from the inner wall. It seems that the hexagonal phase presence had no influence on those changes since a similar behavior was found also close to the cold end of the tube, where no hexagonal phase was present (curve "0" in Figure 101). Higher Young's moduli might be expected at the outer surface due to lower porosity (see Figure 39). However, this was not the case, since the specimens in as-received state had uniform values of E_{IT} and H_{IT} (Figure 73b). It therefore might be suggested that the E_{IT} gradients could be caused by chemical stresses generated by differences in oxygen stoichiometry across the wall thickness. However an E_{IT} gradient was also visible at the cold end which should be representative for demonstrator tubes the in as-received state where no chemical strain was present. Note that the tubes investigated in the as-received condition are not exactly the same as operated in the demonstrator (their diameters differs – $Ø_O$ =15 mm and $Ø_O$ = 10 mm in case of tubes in the as-received state for the experiments in the present work and in the demonstrator, respectively).

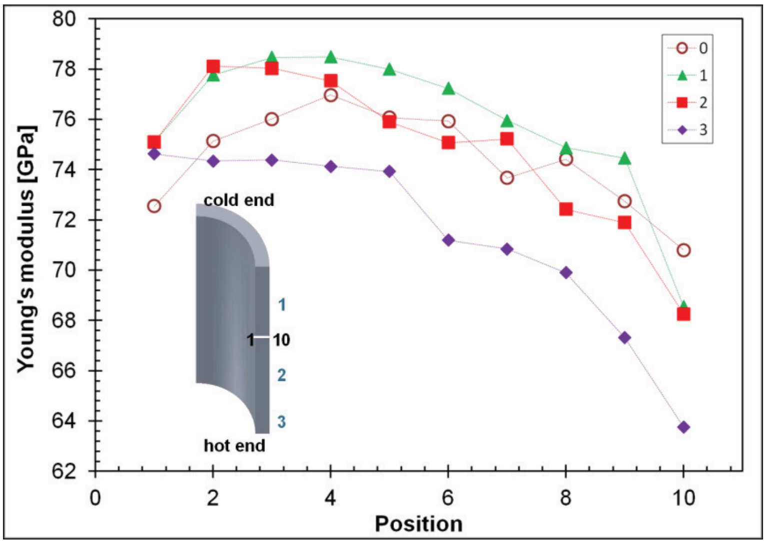

Figure 101. Young's modulus across the tube after operation.

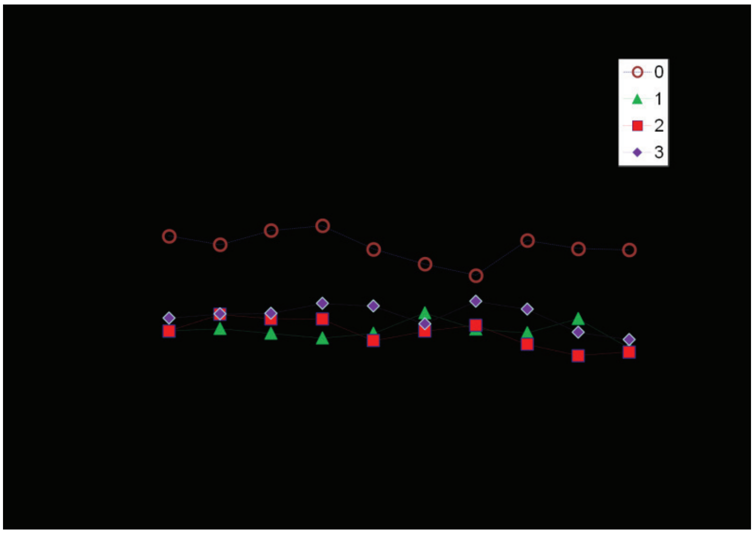

Figure 102. Microhardness profile for a part of tube after operation, exposed to a temperature around 750 °C (1, 2, 3) and for cold end (0).

However, although the manufacturing process should be similar in both cases, the materials appear to be different. For curve 3 (Figure 101), corresponding to the position exposed to 800 °C, the average value of Young's modulus was 72 ± 4 GPa, which is about 16% higher than the value obtained for as-received specimens given above (Figure 73b).

Micro-hardness results are presented in Figure 102. Small fluctuations of hardness are visible, but they were within the limits of standard deviation and therefore hardness appears to be rather independent from the cross-sectional position. Micro-hardness data agree with those obtained for specimens in as-received state (Figure 73b).

Table 12 shows the fracture toughness calculated from Equation 17 for sub-layers No 1, 2 and 9, 10.

Table 12. Fracture toughness at particular positions of a tube after operation, exposed to a temperature around 750 °C.

position	K [MPa·m$^{0.5}$]
1	0.75 ± 0.043
2	0.79 ± 0.049
9	0.82 ± 0.046
10	0.76 ± 0.036

The fracture toughness agrees within its standard deviation with the values measured for as - received specimens (see chapter 3.3.1).

3.6.2. **Temperature profile along the tube**

After macro-mechanical tests, broken parts of selected sections were embedded in epoxy resin and subjected to microstructural investigations. LM investigation revealed differences in the hexagonal phase distribution along the tube length. These microstructural gradients were caused by the inhomogeneous temperature distribution inside the furnace (along the tube length) and oxygen partial pressure gradients (across the wall thickness). Microstructures of particular tube segments were compared with microstructural results of complementarily heat treated specimens (annealing for 336 h at temperature range from 750 to 950 °C) described in chapter 3.2.1.

In Figure 103, a tube after operation with six sections marked by red frames, in which significant changes related to the hexagonal phase might be expected, is presented.

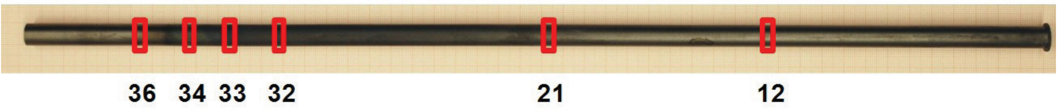

Figure 103. Tube after operation with indication of 6 segments for subsequent microstructural characterization.

In Figure 104, the microstructures of the prepared segments' cross-sections are visible. Label "inside" indicates images taken close to inner surface of the tube (vacuum side), whereas "outside" indicates areas close to the outer surface of the tube (air side).

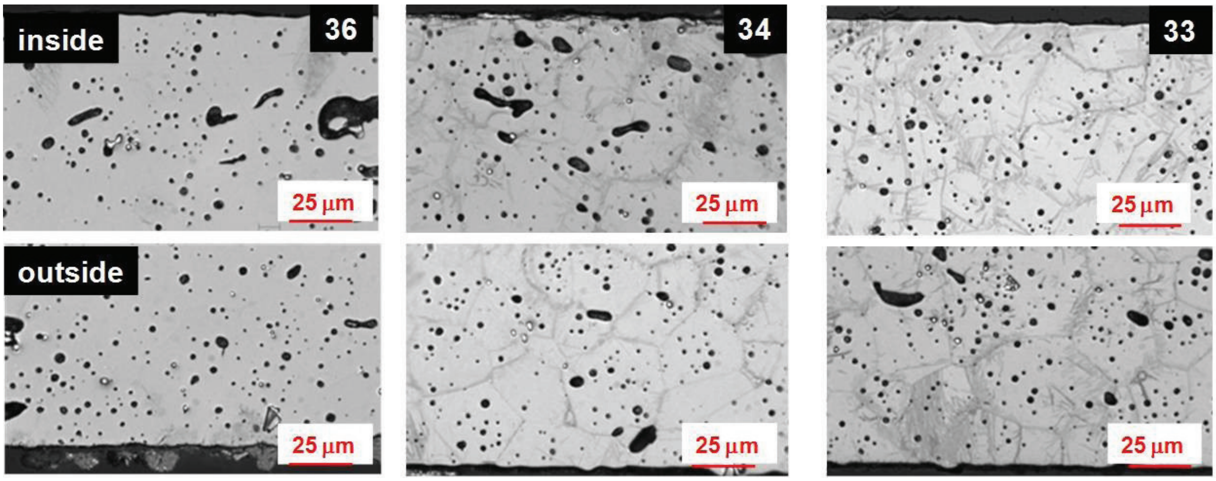

Figure 104. Microstructural images of segments marked as "36", "34", "33", showing similar microstructures to reference specimens in Figure 51.

From the comparison with the reference microstructure (Figure 51) of annealed material it can be concluded that section 36 which was close to cold end, was operated at a temperature below 700 °C (no hexagonal phase in the microstructure). However, in the segment placed 2 cm further on the right hand side (34), a limited amount of hexagonal phase was found at the grain boundaries. Hence, it is concluded that this material segment was exposed to a temperature around 720 °C. Observation of segment 33 revealed much higher quantity of hexagonal phase localized at the grain boundaries and also inside the grains. The latter agrees very well to the microstructure of specimen annealed at 750 °C for 336 h (Figure 51a).

During further microstructural investigations (Figure 105) performed on section 32, significantly less hexagonal phase (in comparison to section 33) was found. The amount of hexagonal phase and its occurrence at the grain boundaries allowed to relate the microstructure to a service temperature of 800 °C. Microstructures found for sections 21 and 12 agreed with microstructure of the material annealed at the 850 °C and higher.

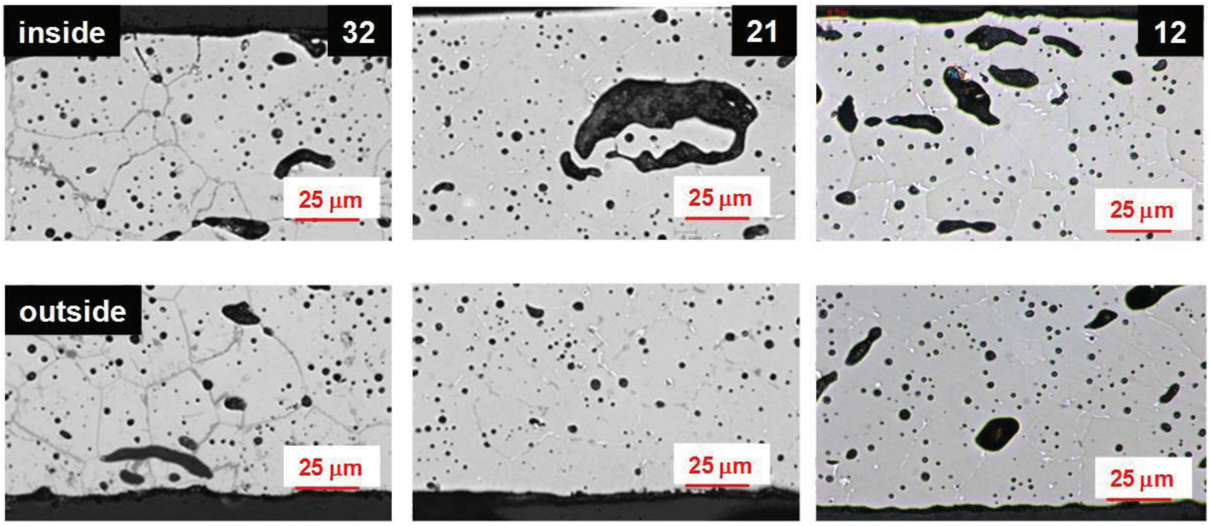

Figure 105. Microstructural images of segments marked as "32", "21", "12", showing similar microstructures to reference specimens in Figure 51.

Note that hexagonal phase is present also at the vacuum (20 mbar) side, which strongly suggests that the mechanical properties and in particular that creep rate of the vacuum side will be similar to this obtained in air. Also higher fracture stress should be expected during presence of hexagonal phase. The stoichiometry at the vacuum side cannot be deduced from the absolute pressure during operation, rather it appears to be a result of the oxygen transport through the membrane.

Based on the investigation described above, an axial temperature profile along the tube was reconstructed (Figure 106).

This temperature profile was compared with temperature profile obtained in-situ during demonstrator operation. Excellent agreement was found.

As mentioned earlier, the relative position of the tube in the demonstration unit was unknown. The insert in the left upper corner of the diagram in Figure 106, presents a schematic drawing of the tubes' distribution in the demonstrator furnace. The plot (red lines and squares) gives the temperature profile for tube no 12 (placed at the right side of demonstrator). Hence, the point from microstructural investigations corresponding to temperature 850 °C fits very well to the measured profile for tube 12. The in-situ measured profile ends, however, at the point corresponding to 800 °C. In order to compare the data, a 2nd order polynomial fitting of the data was performed and in-situ data were extrapolated down to lower temperatures (blue dashed line).

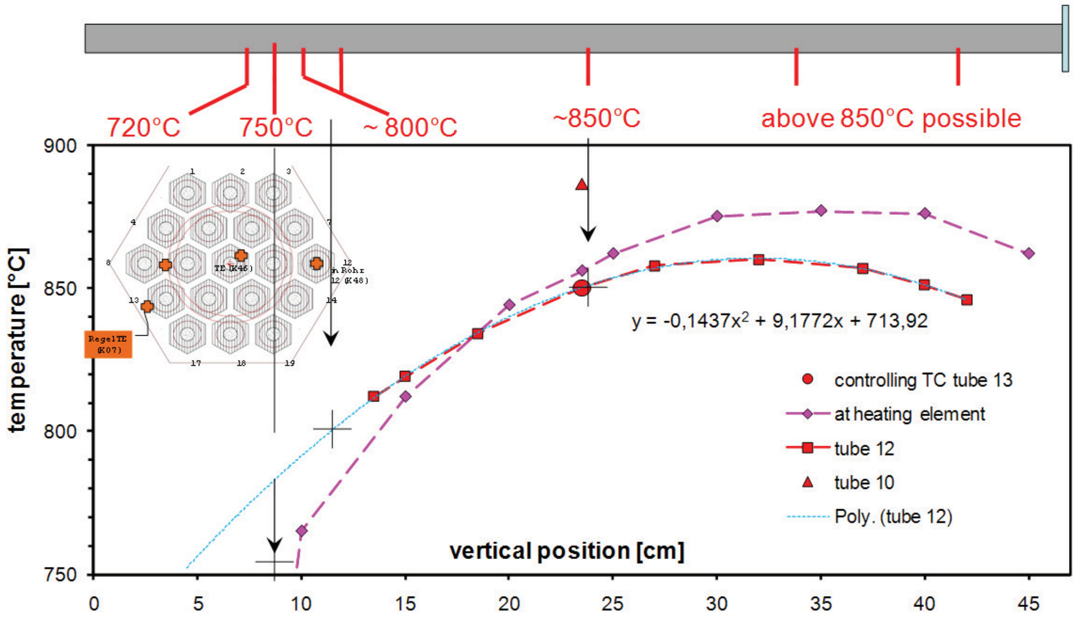

Figure 106. Temperature profile comparison: Temperature profile in tube obtained from microstructural observation (upper part), comparison with temperature profile measured in-situ by thermocouples (diagram - red squares represent temperature measured in the tube, black crosses indicate temperatures estimated from microstructural investigation).

The segment estimated from microstructure to represent a position with a temperature of about 800 °C also fitted well to the profile measured at tube 12. The third point, corresponding to a temperature of 750 °C did not fit well to the extrapolation calculated for the same tube, which predicts this temperature to occur a few more centimeters towards the cold end. The corresponding part of tube was, however, mounted in the cooled metal holder, which might have further reduced the temperature near the very end of the tube.

The temperature measured in-situ at the middle of tube No 10 yields a value of 890 °C, while in the middle of tube 12 the temperature is 850 °C. This indicates that for tube No. 10, all positions where hexagonal phase might be observed will be shifted to the cold end (left) side. Hence, it is also possible to identify the localization of a particular tube in the demonstrator unit by analyzing its microstructure.

Note that the temperature along the tube should be as uniform as possible to optimize permeation. According to the temperature profiles shown in Figure 106 the part of the tube which is exposed to a temperature of more than 850 °C will have a significantly higher local creep rate than the part exposed to a lower temperatures. It can therefore be suggested that the tube diameter will change in a non-uniform way along the axis. This might eventually lead to buckling and enhanced damage of the tube. Hence, the non-uniform temperature profile should be avoided.

Note that during microstructural investigations of tube segments small cracks extending from the ends of long pores were observed (Figure 107).

An effect of preparation can be ruled out since such cracks have not been observed in microstructural observations of non-operated material. In fact, even in the fracture surface of one of the tubes that failed during operation a long crack propagating from the end of a long pore was found (Figure 108).

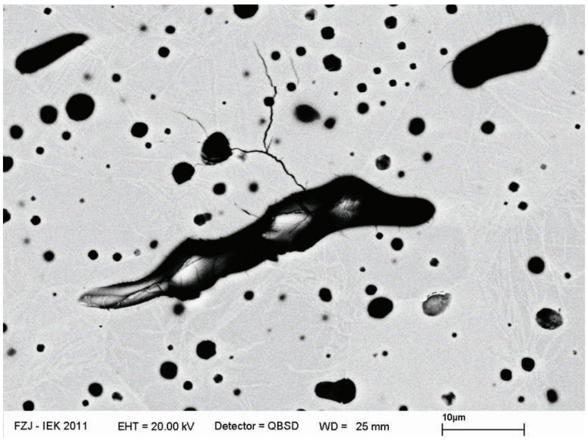

Figure 107. Cracks originating from long pores.

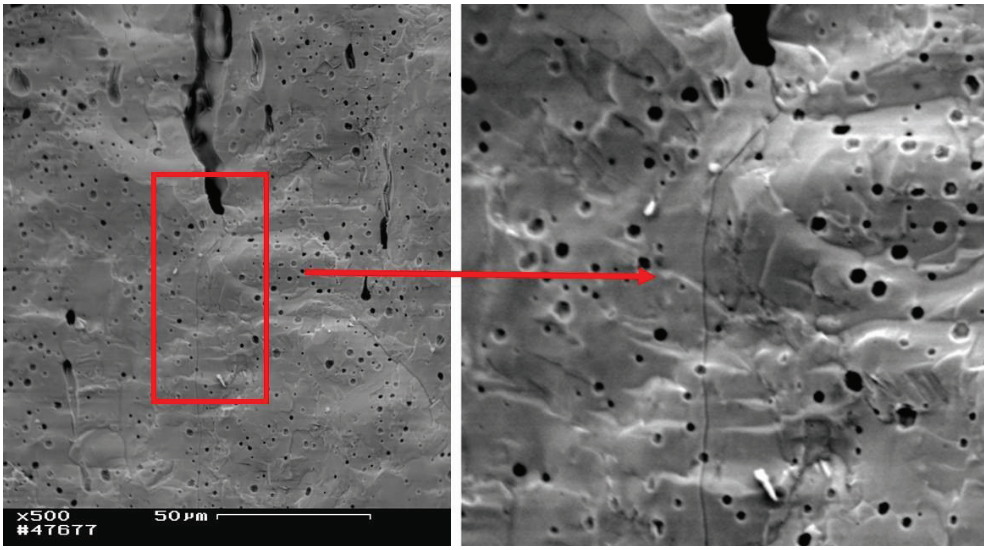

Figure 108. A crack extending from a long pore in the fracture surface of a tube after operation in demonstration unit [image due to courtesy of GFE/RWTH Aachen].

4. Conclusions

The observed hexagonal phase formation, which was fastest at 750 °C (Figure 51a), suggests a pronounced microstructural instability of the BSCF in air (pO_2 = 200 mbar) at operation relevant temperatures (~ 700 < T < ~ 850 °C), (see Figure 51). This temperature range should be avoided since it has been verified that the hexagonal polymorph leads to a very low oxygen permeability [34].

In fact, in addition to some finely dispersed Co_3O_4, also a small amount of hexagonal phase was observed along grain boundaries already in the as-received material, which is formed during the slow (2 K/min) cooling after sintering. During cooling (as well as heating) with such a low rate as 2 K/min, the material remains in the temperature window where hexagonal phase can be formed for almost 75 min. Hence, in order to avoid hexagonal phase presence during membrane operation, the material should be heated to ~ 950 °C during the start-up sequence and dwelled for around 24 h, to dissolve the remnant hexagonal phase. Obviously the subsequent operation temperature should not be lower than 850 °C.

The experimental results suggest that the existence of hexagonal phase is limited to an oxygen partial pressure above 4 mbar, since under higher vacuum conditions (pO_2~10^{-5} mbar) only the formation of CoO (formed by reduction of Co_3O_4) was observed. In addition to microstructural investigation of annealed specimens, the BSCF tubes after operation at 850 °C in the IKTS demonstrator unit were investigated. During operation an oxygen partial pressure of 20 mbar was maintained inside the demonstrator tubes. Hence a gradient in the quantity of hexagonal phase across the wall thickness might be expected since annealing under an oxygen pressure of 4 mbar did not result in the formation of this second phase. However, the hexagonal phase was observed in the entire cross-section of the tube, which might be a result of oxygen transport. Probably for the same reason CoO particles were not found.

The mechanical tests revealed a Young’s modulus for the BSCF of ~ 63 GPa at RT. The value decreased to ~ 45 GPa when heated to 200 °C. Then the modulus recovered partially when the temperature is raised to 350 °C and remained on this level up to 800 °C. It might be suggested that the decrease in Young’s modulus at low temperatures around 200 °C reduces the thermally and chemically induced elastic stresses during cooling and stresses could increase again during further cooling to RT due to increase of Young’s modulus. However, the fracture strength has a similar temperature dependence as Young’s modulus. Hence, even though Young’s modulus and residual stress change, a higher failure probability might not be expected. Strength measurements and fractographic investigation suggest that the IKTS material delivered in tubular form is superior to the planar specimens; measured strength and Weibull modulus were almost 50 % higher. A large number of pores was observed that can act as strength limiting flaws in the planar material (chapter 3.1.3). Although the tubular membrane material was rather homogenous, in addition to large agglomerates elongated pores were found (Figure 43). Hence, the overall reduction of the quantity of large pores should be an aim of further materials development.

It seems that a presence of hexagonal phase does not affect the fracture behavior below 600 °C (Figure 82). However, there is a significant effect at around 800 °C. Although all specimens showed transgranular fracture mode material with higher amount of hexagonal phase resulted in around 25 % higher strength values than observed for specimens annealed at 950 °C for 24 h, where no hexagonal phase was present.

Creep tests were mainly performed on material supplied by the IKTS. However, the behavior in air was verified by investigation on material supplied by the VITO and the University of Twente. The creep behavior of the BSCF in air is significantly different from that observed under vacuum (pO_2 of 4; 10^{-5} mbar). Under vacuum, a change of creep mechanism was observed at around 800 °C; reflected by a change of the activation energy. Similarly also two creep regimes were visible in air when tests were carried out in a heating sequence (see section 3.5.2), however with the kink in the strain-rate – temperature plot shifted to 850 °C. Furthermore, the creep rate measured in air was almost independent of the temperature below 850 °C. Above 850 °C, the temperature dependence was similar as observed under vacuum. The difference of the temperature where the mechanism change occurs probably results from the hexagonal phase creation during the experiments at 750 °C in air. During creep tests in a cooling sequence (see section 3.5.2), creep rates did not overlap with values obtained during heating and only one creep deformation regime was present with a uniform activation energy that agreed with the value obtained under vacuum. The associated creep hysteresis in air is caused by the absence of the hexagonal phase during the cooling sequence. With respect to the creep behavior the hexagonal phase appears to be advantageous, since its presence can decrease creep rates by about one order of magnitude.

At an intermediate oxygen partial pressure of 4 mbar creep rates were slightly higher than in air. However, the overall behavior was similar as under higher vacuum. This might suggest that the different sides of membrane will creep with different rates during operation in an air separation unit. However, in real application this will probably not be the case, since the microstructural investigations on tubes after demonstrator operation suggest that the oxygen concentration profile across the wall thickness is equilibrated by permeation. Creep deformation is aided by cation diffusion and hence, due to charge balance also by the number of available oxygen vacancies. Therefore, it might be suggested that in order to decrease the creep rates the material should be modified in order to decrease the amount of vacancies, which however is not an option since it will also lead to a decrease of permeation.

The creep mechanisms proposed by Huang et al. [104] for the LSCF (coexistence of dislocation creep and lattice diffusion connected with creation of new vacancies at higher temperatures) seem also to be applicable for the creep behavior of the BSCF in air. However under vacuum, due to the continuous change of stress exponent with temperature (see Figure 87), a continuous change of creep mechanisms from pure diffusional (below 850 °C) to coexistence of diffusional and dislocation creep might be suggested. Above 850 °C, a coexistence of lattice and grain boundary diffusion in the BSCF was reported [138]. Some indications of GBS were also noticed in the current work (section 3.2.4).

Since a creep deformation of 1% per year which appears to be acceptable for application [98] it can be suggested that stresses of 2 MPa and 5 MPa are tolerable for operation temperatures of 880 °C and 850 °C, respectively in case of a grain size of 29 µm, section 3.5.2. A further decrease of the operation temperature to 820 °C would allow to increase the applied stress to 10 MPa. For a material with a grain size of 7 µm [99] a strain of 20 % would be reached in one year at 860 °C for a stress of 5 MPa, which is not acceptable. Consequently, during design of membrane modules the grain size is a design parameter that has to be taken into consideration. Furthermore, due to potentially high creep deformation, tubular membranes should not be exposed to high pressure gradients although they lead to high driving forces for permeation. A pressure differences of 17 bar from feed to sweep side yielded in simulations a compressive stress of 6 MPa in a tube with 2 mm wall thickness for a temperature of 800 °C [25]. The creep rate of the BSCF with a grain size of 7 µm under such conditions is more than $2 \cdot 10^{-9}$ s^{-1} [99], leading to strain of ~ 7 % per year. Hence these operating conditions would be unacceptable for fine grained BSCF.

Note that permanent deformation and local creep damage of tubes loaded in tension was observed already when a critical strain of 0.2 % was exceeded. In compression, creep rupture at grain boundaries parallel to the loading direction occurs when ~ 4 % of strain is reached (section 3.2.4).

Overall a steady state creep equation allowed a mathematical description of the data and hence predicting the creep behavior under different conditions. The BSCF is, due to its good oxygen permeation, a promising material for application as oxygen separation membrane. However, further development of the material is necessary in order to improve the stability of the cubic structure, which could allow a decrease of the operation temperature below 850 °C, resulting in an increased component life with respect to creep effects. Additionally, the manufacturing method should be further improved, in order to minimize the content of strength limiting flaws. Moreover, although not an aspect of the current investigation, the stability against CO_2 should be improved, since even minor quantities (20 %) of CO_2 have shown to lead to strong decrease in permeation rates [59].

5. References

[1] J. Conti, P. Holtberg, International Energy Outlook 2011, Independent Statistics & Analysis, U.S. Energy information Administration DOE/EIA-0484 (2011).
[2] U. Nations, Kyoto Protocol to the United Nations Framework Convention on Climate Change (1998).
[3] I.E. Agency, Technology Roadmap. Carbon capture and storage. OECD/IEA (2009).
[4] H. Herzog, J. Meldon, A. Hatton, Advanced Post-Combustion CO2 Capture, MIT (2009).
[5] M. Czyperek, P. Zapp, H.J.M. Bouwmeester, M. Modigell, K.V. Peinemann, I.Voigt, W.A. Meulenberg, L. Singheiser, D. Stöver, Energy Procedia 1 (2009) 303-310.
[6] M. Czyperek, P. Zapp, H.J.M. Bouwmeester, M. Modigell, K. Ebert, I. Voigt, W.A. Meulenberg, L. Singheiser, D. Stöver, Journal of Membrane Science 359 (2010) 149-159.
[7] M. Kanniche, R. Gros-Bonnivard, P. Jaud, J. Valle-Marcos, J. M. Amann, C. Bouallou, Applied Thermal Engineering 30 (2010) 53-62.
[8] M. Modigell, OXYCOAL-AC: Oxyfuel power plant concepts for gas separation with oxygen transport membranes, 9. Jülicher Werkstoffsymposium, 15-16 November (2007).
[9] P. Higginbotham, V. White, K. Fogash, G. Guvelioglu, Energy Procedia 4 (2011) 884-891.
[10] F.K. K.-D. Tigges, C. Bergins, K. Busekrus, J. Niesbach, M. Ehmann,, F.H. C. Kuhr, B. Vollmer, T. Buddenberg, S. Wu, A. Kukoski, Energy Procedia 1 (2009) 549-556.
[11] J. Sunarso, S. Baumann, J.M. Serra, W.A. Meulenberg, S. Liu, Y.S. Lin, J.C.D. da Costa, Journal of Membrane Science 320 (2008) 13-41.
[12] S. Baumann, J.M. Serra, M.P. Lobera, S. Escolástico, F. Schulze-Küppers, W.A. Meulenberg, Journal of Membrane Science 377 (2011) 198-205.
[13] J.F. Vente, S. McIntosh, W.G. Haije, H.J.M. Bouwmeester, Journal of Solid State Electrochemistry 10 (2006) 581-588.
[14] H. Wang, Y. Cong, W. Yang, Catalysis Today 82 (2003) 157-166.
[15] H. Wang, Y. Cong, W. Yang, Journal of Membrane Science 209 (2002) 143-152.
[16] S. Faraji, K. J. Nordheden, S. M. Stagg-Williams, Applied Catalysis B: Environmental 99 (2010) 118-126.
[17] Z. Shao, S. M. Haile, Nature 431 (2004) 170-173.
[18] J. Peña-Martínez, D. Marrero-López, J.C. Ruiz-Morales, B.E. Buergler, P. Núñez, L.J. Gauckler, Solid State Ionics 177 (2006) 2143-2147.
[19] S. Lee, Y. Lim, E.A. Lee, H.J. Hwang, J.W. Moon, Journal of Power Sources 157 (2006) 848-854.
[20] A.Y. Yan, M. Yang, Z.F. Hou, Y.L. Dong, M.J. Cheng, Journal of Power Sources 185 (2008) 76-84.
[21] Q.L. Liu, K.A. Khor, S.H. Chan, Journal of Power Sources 161 (2006) 123-128.
[22] Y. Zhang, J. Liua, X. Huang, Z. Lu, W. Sub, Solid State Ionics 179 (2008) 250-255.
[23] C. Buysse, A. Kovalevsky, F. Snijkers, A. Buekenhoudt, S. Mullens, J. Luyten, J. Kretzschmar, S. Lenaerts, Journal of Membrane Science 372 (2011) 239-248.
[24] H.H. Wang, R. Wang, D.T. Liang, W.S. Yang, Journal of Membrane Science 243 (2004) 405-415.
[25] S. Engels, F. Beggel, M. Modigell, H. Stadler, Journal of Membrane Science 359 (2010) 93-101.
[26] B.X. Huang, Thermo-Mechanical Properties of Mixed Ion-Electron Conducting Membrane Materials, PhD thesis, Aachen (2010).
[27] R. Kriegel, R. Kircheisen, J. Töpfer, Solid State Ionics 181 (2010) 64-70.
[28] P. Higginbotham, V. White, K. Fogash, G. Guvelioglu, International Journal of Greenhouse Gas Control 5S (2011) S194-S203.
[29] Vattenfall, http://www.zeroco2.no/introduction/what-is-ccs/vattenfalloxyfuel.jpg.

[30] Z.P. Shao, G.X. Xiong, J.H. Tong, H. Dong, W.S. Yang, Separation and Purification Technology 25 (2001) 419-429.
[31] H. Kruidhof, H.J.M. Bouwmeester, R.H.E. Vondoorn, A.J. Burggraaf, Solid State Ionics 63-5 (1993) 816-822.
[32] H.H. Wang, S. Tablet, W.S. Yang, R. Caro, Materials Letters 59 (2005) 3750-3755.
[33] J. Ovenstone, J.I. Jung, J.S. White, D.D. Edwards, S.T. Misture, Journal of Solid State Chemistry 181 (2008) 576-586.
[34] Z.P. Shao, W.S. Yang, Y. Cong, H. Dong, J.H. Tong, G.X. Xiong, Journal of Membrane Science 172 (2000) 177-188.
[35] A. Yan, B. Liu, Y. Dong, Z. Tian, D. Wang, M. Cheng, Applied Catalysis B: Environmental 80 (2008) 24-31.
[36] B.X. Huang, J. Malzbender, R.W. Steinbrech, E. Wessel, H.J. Penkalla, L. Singheiser, Journal of Membrane Science 349 (2010) 183-188.
[37] Q. Zhu, T. Jin, Y. Wang, Solid State Ionics 177 (2006) 1199-1204.
[38] Z. Shao, G. Xiong, Y. Cong, W. Yang, J. Membr. Sci 164 (2000).
[39] X. Zhu, H. Wang, W. Yang, Chem. Commun. (2004).
[40] J. Tong, W. Yang, B. Zhu, R. Cai, J. Membr. Sci. 203 (2002).
[41] H. Wang, C. Tablet, A. Feldhoff, J. Caro, Adv. Mater 17 (2005).
[42] J. Tong, W. Yang, R. Cai, B. Zhu, G. Xiong, L. Lin, Sep. Purif. Technol 32 (2003).
[43] S. Xie, W. Liu, K. Wu, P.H. Yang, G.Y. Meng, C.S. Chen, Solid State Ionics 118 (1999).
[44] C.Y. Tsai, A.G. Dixon, Y.H. Ma, W.R. Moser, M.R. Pascucci, J. Am. Ceram. Soc. 81 (1998).
[45] Y. Teraoka, T. Nobunaga, N. Yamazoe, Chem. Lett. (1988).
[46] Y. Teraoka, H.M. Zhang, S. Furukawa, N. Yamazoe, Chem. Lett. (1985).
[47] J.E. ten Elshof, H.J.M. Bouwmeester, H. Verweij, Solid State Ionics 81 (1995).
[48] V.V. Kharton, A.A. Yaremchenko, A.V. Kovalevsky, A.P. Viskup, E.N. Naumovich, P.F. Kerko, J. Membr. Sci 163 (1999) 307-317.
[49] H.W. Brinkman, H. Kruidhof, A.J. Burggraaf, Solid State Ionics 68 (1994).
[50] Y.H. Lim, J. Lee, J.S. Yoon, C.E. Kim, H.J. Hwang, Journal of Power Sources 171 (2007) 79-85.
[51] Z.H. Chen, R. Ran, W. Zhou, Z.P. Shao, S.M. Liu, Electrochimica Acta 52 (2007) 7343-7351.
[52] A.C.v. Veen, M. Rebeilleau, D. Farrusseng, C. Mirodatos, The Royal Society of Chemistry (2003) 32-33.
[53] S. McIntosh, J.F. Vente, W.G. Haije, D.H.A. Blank, H.J.M. Bouwmeester, Chemistry of Materials 18 (2006) 2187-2193.
[54] S. McIntosh, J.F. Vente, W.G. Haije, D.H.A. Blank, H.J.M. Bouwmeester, Solid State Ionics 177 (2006) 1737-1742.
[55] C. Niedrig, S.Taufall, M. Burriel, W. Menesklou, S. F. Wagner, S. Baumann, E. Ivers-Tiffée, Solid State Ionics 197 (2011) 25-31.
[56] S. Svarcova, K. Wiik, J. Tolchard, H.J.M. Bouwmeester, T. Grande, Solid State Ionics 178 (2008) 1787-1791.
[57] J-I. Jung, D.D. Edwards, Journal of Materials Science 46 (2011) 7415-7422.
[58] Z. Yang, J. Martynczuk, K. Efimov, A. S. Harvey, A. Infortuna, P. Kocher, L.J. Gauckler, Chemistry of Materials 23 (2011) 3169–3175.
[59] M. Schulz, R. Kriegel, A. Kämpfer, Journal of Membrane Science 378 (2011) 10– 17.
[60] M. Arnold, H.H. Wang, A. Feldhoff, Journal of Membrane Science 293 (2007) 44-52.
[61] S. Engels, T. Markus, M. Modigell, L. Singheiser, Journal of Membrane Science 370 (2011) 58-69.
[62] J. Yi, M. Schroeder, Journal of Membrane Science 378 (2011) 163-170.

[63] Q. Zeng, Y. Zuo, C. Fan, C. Chen, Journal of Membrane Science (2009) 140-144.
[64] N. Orlovskaya, M. Lugovy, S. Pathak, D. Steinmetz, J. Lloyd, L. Fegely, M. Radovic, E.A. Payzant, E. Lara-Curzio, L.F. Allard, J. Kuebler, Journal of Power Sources 182 (2008) 230-239.
[65] J. Mastin, M.A. Einarsrud, T. Grande, Chem. Mater 18 (2006) 1680-1687.
[66] S. Miyoshi, J.O. Hong, K. Yashiro, A. Kaimai, Y. Nigara, K. Kawamura, T. Kawada, J. Mizusaki, Solid State Ionics 161 (2003) 209-217.
[67] E. Bucher, A. Egger, P. Ried, W. Sitte, P. Holtappels, Solid State Ionics 179 (2008) 1032-1035.
[68] P.V. Hendriksen, P.H. Larsen, M. Mogensen, F.W. Poulsen, K. Wiik, Catal. Today 56 (2000) 283 - 295.
[69] A. Atkinson, T.M.G.M. Ramos, Solid State Ionics 129 (2000) 259 - 269.
[70] M. Lipinska-Chwalek, J. Malzbender, A. Chanda, S. Baumann, R.W. Steinbrech, Journal of the European Ceramic Society 31 (2011) 2997-3002.
[71] H. L. Lein, Ø. S. Andersen, P. E. Vullum, E. Lara-Curzio, R. Holmestad, M.A. Einarsrud, T. Grande, Journal of Solid State Electrochemistry 10 (2006) 635-642.
[72] B.X. Huang, J. Malzbender, R.W. Steinbrech, L. Singheiser, Journal of Membrane Science 359 (2010) 80-85.
[73] Y.S. Chou, J.W. Stevenson, T.R. Armstrong, L.R. Pederson, Journal of the American Ceramic Society 83 (2000) 1457–1464.
[74] N. Orlovskaya, K. Kleveland, T. Grande, M.A. Einarsrud, Journal of the European Ceramic Society 20 (2000) 51-56.
[75] A. Fossdal, M. -A. Einarsrud, T. Grande, Journal of the European Ceramic Society 25 (2005) 927-933.
[76] K. C. Goretta, E. T. Park, R. E. Koritala, M. M. Cuber, E. A. Pascual, N. Chen, A. R. de Arellano-López, J. L. Routbort, Physica C: Superconductivity 309 (1998) 245-250.
[77] A. Julian, E. Juste, P.M. Geffroy, N. Tessier-Doyen, P. Del Gallo, N. Richet, T. Chartiera, Journal of the European Ceramic Society 29 (2009) 2603-2610.
[78] T.L. Anderson, Fracture Mechanics. Fundamentals and Applications. Second edition, CRC Press, Inc. (1995).
[79] G.D. Quinn, Fractography of Ceramics and Glasses, NIST (2007).
[80] A. Atkinson, A. Selçuk, Solid State Ionics 134 (2000) 59-66.
[81] N. M. Sammes, R. Ratnaraj, M. G. Fee, Journal of Materials Science 29 (1994) 4319-4324.
[82] S.W. Paulik, S. Baskaran, T.R. Armstrong, Journal of Materials Science 33 (1998) 2397-2404.
[83] N. Nagendra, S. Bandopadhyay, Scripta Materialia 48 (2003) 37-42.
[84] Y.S. Chou, K. Kerstetter, L.R. Pederson, R.E. Williford, Journal of Materials Research 16 (2001) 3545-3553.
[85] D.L. Meixner, R.A. Cutler, Solid State Ionics 146 (2002) 273-284.
[86] C.M. D'Souza, N.M. Sammes, Journal of the American Ceramic Society 83 (2000) 47-52.
[87] C.S. Montross, H. Yokokawa, M. Dokiya, L. Bekessy, Journal of the American Ceramic Society 78 (1995) 1869-1872.
[88] N.M. Sammes, R. Ratnaraj, Journal of Materials Science 32 (1997) 687-692.
[89] DIN, Deutsches Institut für Normung (2007).
[90] K. Kleveland, N. Orlovskaya, T. Grande, A.M.M. Moe, M.A. Einarsrud, K. Breder, G. Gogotsi, Journal of the American Ceramic Society 84 (2001) 2029-2033.
[91] S. Baskaran, C.A. Lewinsohn, Y.S. Chou, M. Qian, J.W. Stevenson, T.R. Armstrong, Journal of Materials Science 34 (1999) 3913-3922.
[92] N. Orlovskaya, M. Lugovy, S. Pathak, D. Steinmetz, J. Lloyd, L. Fegely, M. Radovic, E. Andrew Payzant, E. Lara-Curzio, L. F. Allard, J. Kuebler, Journal of Power Sources 182 (2008) 230-239.

[93] D. Dierickx, I. Houben, J. Lapin, F. Delannay, O. VanDerBiest, Journal of Materials Science Letters 15 (1996) 1573-1576.
[94] H.L. Lein, O.S. Andersen, P.E. Vullum, E. Lara-Curzio, R. Holmestad, M.A. Einarsrud, T. Grande, Journal of Solid State Electrochemistry 10 (2006) 635-642.
[95] A. Chanda, B.X. Huang, J. Malzbender, R.W. Steinbrech, Journal of the European Ceramic Society 31 (2011) 401-408.
[96] M. Radovic, M.W. Barsoum, T. El-Raghy, S. Wiederhorn, Acta Materialia 49 (2001) 4103-4112
[97] F. Lofaj, S. M. Wiederhorn, G. G. Long, B. J. Hockey, P. R. Jemian, L. Browder, J. Andreason, U. Täffner, Journal of the European Ceramic Society 22 (2002) 2479-2487
[98] D.R. Thompson, L.E. Bool, J.C. Chen, Oxygen enchanced combustion for NOx control - Final Report, in: Praxair, Inc., 2004.
[99] J.X. Yi, H.L. Lein, T. Grande, S. Yakovlev, H.J.M. Bouwmeester, Solid State Ionics 180 (2009) 1564–1568.
[100] G. Majkic, L.T. Wheeler, K. Salama, Solid State Ionics 164 (2003) 137-148.
[101] G. Majkic, L. Wheeler, K. Salama, Acta Materialia 48 (2000) 1907-1917.
[102] P. E. EVANS, Journal of the American Ceramic Society 53 (1970) 365–369.
[103] H.L. Lein, K. Wiik, M.A. Einarsrud, T. Grande, Journal of the American Ceramic Society 89 (2006) 2895-2898.
[104] B.X. Huang, J. Malzbender, S. Baumann, R.W. Steinbrech, Acta Materialia In press (2011).
[105] J. Wolfenstine, P. Huang, A. Petric, Journal of the Electrochemical Society 147 (2000) 1668-1670.
[106] Standard, ASTM C1499-05.
[107] S. R. Choi, J. A Salem, F. A Holland, NASA Technical Memorandum 107369 (1997).
[108] K. Bongartz, E. Gyarmati, H. Schuster, K. Tauber, Journal of Nuclear Materials 62 (1976) 123-137

[109] Standard, ISO 20501, Fine ceramics (advanced ceramics, adwanced technical ceramics) - Weibull statistics for Strength data (2003).
[110] Standard, DIN EN 1288-1.
[111] www.gordonengland.co.uk, http://www.gordonengland.co.uk/hardness/microhardness.htm.
[112] A. R. Franco Jr., G. PintaúdeII, A. SinatoraI, C. E. PinedoIII, A. P. TschiptschinI, Materials Research 7 (2004).
[113] J. Gubicza, A. Juhasz, J. Lendvai, Journal of Materials Research 11 (1996) 2964-2967.
[114] C. B. Ponton, R. D. Rawlings, Materials Science and Technology 5 (1989) 865-872.
[115] I. J. McColm, Ceramic hardness, Plenum Press, New York (1990).
[116] R. Kriegel, Keramische Werkstoffe, 119 Erg.-Lfg., Kapitel 8.10.1.1 (November 2010).
[117] IKTS, http://www.ikts.fraunhofer.de/en/research_fields/Environmental_Engineering_and_Bioenergy/mixedconductorscatalysis/oxygen_separation/index.jsp.
[118] D.N. Mueller, R.A.D. Souza, T.E. Weirich, D. Roehrens, J. Mayer, M. Martin, Physical Chemistry Chemical Physics 12 (2010) 10320–10328.
[119] K. Efimov, Q. Xu, A. Feldhoff, Chemistry of Materials 22 (2010) 5866–5875.
[120] X. Yang, Mechanical Failure of Ceramic Materials in Components of the Energy Industry, Master Thesis, Aachen (2011).
[121] C. Niedrig, S. F. Wagner, E. Ivers-Tiffée, MEM-BRAIN RT 1 Meeting – Berlin, February 23/24, (2011) unpublished.
[122] G.A. El-Shobaky, I.F. Hewaidy, N.M. Ghoneima, Thermochimica Acta 53 (1982) 105 - 114.

[123] G.A. El-Shobaky, A.S. Ahmad, A.N. Al-Noaimi, H.G. El-Shobaky, Journal of Thermal Analysis 46 (1996) 1801 - 1808.
[124] C. Buysse, A. Kovalevsky, F. Snijkers, A. Buekenhoudt, S. Mullens, J. Luyten, J. Kretzschmar, S. Lenaerts, Journal of Membrane Science 359 (2010) 86-92.
[125] A. Kovalevsky, C. Buysse, F. Snijkers, A. Buekenhoudt, J. Luyten, J. Kretzschmar, S. Lenaerts, Journal of Membrane Science 368 (2011) 223-232.
[126] O. M. Jadaan, D. L. Shelleman, J. J.C. Conway, J. J.J. Mecholsky, R. E. Tressler, Journal of Testing and Evaluation 19 (1991) 181-191.
[127] J. Gong, J. Wu, Z. Guan, Journal of the European Ceramic Society 19 (1999) 2625-2631.
[128] I. Manika, J. Maniks, Acta Materialia 54 (2006) 2049-2056.
[129] K.K. Tho, S. Swaddiwudhipong, J. Hua, Z.S. Liu, Materials Science and Engineering A 421 (2006) 268-275.
[130] B. W. Mott, Micro-Indentation Hardness Testing, Butterworths Scientific, London (1956).
[131] M. L. Tarkanian, J. P. Neumann, L.Raymond, ed. J. H. Westbrook and H. Conrad. American Society for Metals, Metal Park, OH, (1973) 187–198.
[132] W.D. Nix, H. Gao, Journal of the Mechanics and Physics of Solids 46 (1998) 411-425.
[133] W. Mason, P. F. Johnson, J. R. Varner, J. Mater. Sci 26 (1991) 6576–6580.
[134] H. Li, A. Ghosh, Y. H. Han, R. C. Bradt, Journal of Materials Research 8 (1993) 1028-1032.
[135] M. F. Ashby, D. R. H. Jones, Engineering Materials 2 - An Introduction to their Properties and Applications, Pergamon Press (1980).
[136] S.I. S. Murata, M. Suzuki, Y. Kobayashi, K. Asai, K. Kohn, Physica B 263-264 (1999) 647-649.
[137] B. Huang, J. Malzbender, R.W. Steinbrech, Journal of Materials Research 26 (2011) 1388-1391.
[138] M. Schröder, Project MEM-BRAIN Status Report Valencia, 2011 (2011).
[139] B. Rutkowski, J. Malzbender, R.W. Steinbrech, T. Beck, H.J.M. Bouwmeester, Journal of Membrane Science 381 (2011) 221-225.
[140] M. Ashby, H. Shercliff, D. Cebon, Materials: engineering, science, processing and design, Elsevier Ltd., 2007.

6. **List of figures**

7. List of tables

8. **Nomenclature**

Acronyms

AR	aspect ratio
ASU	air separation unit
BCF	$BaCo_{0.8}Fe_{0.2}O_{3-\delta}$
BCFZ 1442	$BaCo_{0.4}Fe_{0.4}Zr_{0.2}O_{3-\delta}$
BSC	$Ba_{0.5}Sr_{0.5}CoO_{3-\delta}$
BSCF 5582	$Ba_{0.5}Sr_{0.5}Co_{0.8}Fe_{0.2}O_{3-\delta}$
BSF	$Ba_{0.5}Sr_{0.5}FeO_{3-\delta}$

CASINO	„Monte Carlo simulation of electron trajectory in solids”
CGO	$Ce_{0.2}Gd_{0.8}O_2$
FIB	focused ion beam
GBS	grain boundary sliding
GFE	Gemeinschaftslabor für Elektronenmikroskopie
HITK	Hermsdorfer Institut für Technische Keramik e.V.
IKTS	Fraunhofer-Institut für Keramische Technologien und Systeme, Institutsteil Hermsdorf
ISE	indentation size effect
LM	light microscopy
LSC	$La_{0.5}Sr_{0.5}CoO_{3-\delta}$
LSCF	$La_{0.6}Sr_{0.4}Co_{0.8}Fe_{0.2}O_{3-\delta}$
LSCF 5555	$La_{0.5}Sr_{0.5}Fe_{0.5}Co_{0.5}O_{3-\delta}$
LSGM-2015	$La_{0.8}Sr_{0.2}Ga_{0.85}Mg_{0.15}O_{2.825}$
LT-SOFC	low temperature solid oxide fuel cell
LVDT	linear variable differential transformer
MIEC	mixed ionic-electronic conductor
O_2-TDP	temperature programmed desorption of oxygen
RT	room temperature

RWTH	Rheinisch-Westfaelische Technische Hochschule, Aachen (Germany)
SCF	$SrCo_{0.8}Fe_{0.2}O_{3-\delta}$
SEM	scanning electron microscopy
SIMS	secondary ion mass spectrometry
TDP	temperature programmed desorption
TEC	thermal expansion coefficient
TEM	transmission electron microscopy
TGA-DTA	differential thermal analysis
XRD	X-ray diffraction
VITO	Flemish Institute for Technological Research NV (Belgium)

Latin symbols

a	half of imprint’s diagonal length [m]
Ac	projected contact area
b	width [m]
d	grain size [µm]
d_B	specimen’s deflection [m]
d_e	central deflection of specimen [m]
E	Young’s modulus [GPa]

E_a	activation energy [kJ·mol^{-1}]
E_i	Young's modulus of indenter [GPa]
E_{IT}	indentation Young's modulus [GPa]
F_B	maximal applied force [N]
g	radius of tube [m]
h	indentation depth
h_c	contact depth
H_{IT}	indentation hardness [N/mm^2]
k	specimen thickness [m]
K_{ind}	indentation toughness [MPa·√m]
l	length [m]
m	oxygen partial pressure exponent
n	stress exponent
p	grain size exponent
P	applied force [N]
P_B	fracture load [N]
P_{max}	peak load in indentation [N]
pO_2	oxygen partial pressure [mbar]

P_S	survival probability
r_o	outer radius [m]
r_i	inner radius [m]
R	gas constant
R_1	radius of loading ring [m]
R_2	radius of supporting ring [m]
R_3	specimen radius [m]
s	pressure difference between inner and outer side of tube
t	time
T	temperature [°C or K]
u	Weibull modulus
V_0	characteristic volume of tested specimen
x_0	equilibrium separation of atoms

Greek symbols

α	thermal expansion coefficient [K^{-1}]
β	correction factor for Vickers indenter (1.0124)
γ_S	surface energy
ε	strain

ε_c	elastic strain
v	Poisson’s ratio
v_i	Poisson’s ratio of indenter tip
v_s	Poisson’s ratio of specimen
σ	stress [MPa]
σ_e	elastic stress [MPa]
Ø	diameter [m]

9. **Acknowledgments**

First of all, I would like to express my sincere appreciation to my supervisors, Professor A. Czyrska-Filemonowicz and Professor T. Beck for their guidance, great commitment in supervising my work and for their valuable support and substantive discussions.

I would also like to thank Dr. R. Steinbrech and Dr. J. Malzbender who always were ready to share tangible experimental advices and substantial discussions, as well as Dr. M. Lipińska-Chwałek and Mr. G. Pećanac for great substantive support.

I would like to express my gratitude to Ms. T. Osipova, Ms. M. Braun, Mr. J. Mönch and Mr. R. Küppers for excellent technical support, Dr. R. Kriegel (IKTS), Dr. S. Baumann (IEK-1) for providing the BSCF specimens, Dr. B.X. Huang for valuable discussions.

This work was supported by the Initiative and Networking Fund of the Helmholtz Association, contract HA-104 (“MEM-BRAIN”).